UNIVERSITY OF READING

Department of Meteorology

Novel Applications of Polarimetric Radar in Mixed-Phase Clouds and Rainfall

William Keat

A thesis submitted for the degree of Doctor of Philosophy

June, 2016

Declaration

I confirm that this is my own work and the use of all material from other sources has been properly and fully acknowledged.

William Keat

Abstract

This thesis presents novel uses of routinely measured dual polarisation radar variables to improve our understanding of the microphysics of mixed-phase clouds and rainfall. Fundamentally, a new variable $L = -\log_{10}(1 - \rho_{hv})$ is defined, which has preferable statistical properties to the co-polar correlation coefficient (ρ_{hv}) and allows rigorous confidence intervals on ρ_{hv} to be derived. The use of this variable also removes biases introduced by averaging many ρ_{hv} samples and allows, for the first time, ρ_{hv} to be used quantitatively.

An emphasis is placed on how these variables can be used to retrieve microphysical information in embedded mixed-phase regions, which are particularly poorly understood at present. Using a combination of differential reflectivity (Z_{DR}) and differential Doppler velocity (DDV), new statistics of the frequency of occurrence of mixed-phase clouds are presented. During a 3 month observational campaign, it is estimated that embedded mixed-phase clouds occur 26% of the time.

A technique to remove the ambiguity of interpreting Z_{DR} measurements when pristine oriented crystals are present amongst larger aggregate crystals is also presented. By combining L and Z_{DR}, the contribution to the radar signal from pristine oriented crystals (C) and their "intrinsic" Z_{DR} (Z^P_{DRI}) that would otherwise be hidden is retrieved. The results show that elevated Z_{DR} above the melting layer was typically the result of pristine oriented crystals with Z^P_{DRI} between 3 and 7 dB, with varying contributions to the radar reflectivity. The retrieval provides an insight into the microphysics of embedded mixed-phase clouds using dual polarisation radar not before possible.

Finally, the possibility of using L to measure the shape parameter (μ) in the gamma drop size distribution to improve rain rate retrievals is also investigated. It is shown that including drop oscillations is essential for this application. In a convective rain case study, μ appears to be substantially larger than 0 (an exponential DSD), and would result in an overestimated rain rate by up to 50% compared to if a simple exponential DSD is assumed. The potential to retrieve μ with operational radars is also discussed.

Acknowledgements

Firstly, I would like to express my gratitude to my two supervisors **Chris Westbrook** and **Anthony Illingworth**. Thanks for your enthusiasm, ideas and guidance throughout this journey, without which this thesis would not exist.

I would like to thank the staff at STFC for both the maintenance and operation of radars that made this work possible, in particular, **Chris Walden** and **John Bradford**. Thanks to **Stuart Fox** from the Met Office for the processing of aircraft data used in this thesis. Thank you also to the members of my monitoring committee: **Robin Hogan**, **Christine Chiu** and **Nicolas Bellouin** for your guidance and critique.

I owe a great deal to the friends I have made in the department in the past few years, especially those on Lyle 5, who have helped make my experience an enjoyable one. Special mentions go to **Mark Fielding**, **Matt Young**, **Julian Mann**, **Jake Gristey**, **Rob Thompson** and **Andy Barrett**. Thank you Mark in particular for our numerous radar chats, and our many refreshing (and sometimes day-ending) lunchtime runs!

Finally, I am extremely grateful to my family and Becca. Thank you all for your support throughout the PhD.

Contents

Chapter 1

Introduction

Mixed-phase clouds play an important role in the Earth's radiation budget (Comstock *et al.*, 2007; Solomon *et al.*, 2007). Yet, of all cloud types, they are one of the most poorly understood, and are one of the greatest sources of uncertainty in future climate projections (Sun and Shine, 1994; Gregory and Morris, 1996; Mitchell *et al.*, 1989; Senior and Mitchell, 1993). Complex interactions and feedbacks between incoming and outgoing radiation, cloud dynamics and the microphysical processes make them particularly challenging to understand, but fundamentally there is a lack of good observational datasets of mixed-phase clouds. Characteristics such as the frequency of occurrence and microphysical properties of mixed-phase regions embedded within deeper ice cloud, which are thought to be fundamental to precipitation development (Mülmenstädt *et al.*, 2015), are not well known. Observational techniques to measure this type of mixed-phase cloud are lacking.

Another problem which is long-standing in the field of radar meteorology is the accurate retrieval of rain rates from weather radars, which is important for many industries (e.g. agriculture), and for public flood warnings. Traditional radars estimate rain rate using radar reflectivity from a single polarisation, using empirically derived reflectivity-rain rate ($Z-R$) relationships. Rain rates estimated in this way are sensitive to variations in the drop size distribution (DSD), and so an accurate understanding of rain DSDs is needed. In particular, the shape of the DSD can have a large impact on rain rate estimates. Typically, ground based disdrometer instruments have been used to estimate DSD shape, and statistically relate it to other parameters of the distribution. Radar parameters can then be related to rain rate statistically. However disdrometers suffer from small sampling volumes and underestimation of small and large drops which can lead to biases in these estimates. Direct radar estimates of the DSD are preferable, due to the much larger number of drops being sampled. Typically, dual polarisation radar provides two observed parameters, however there are three unknown parameters in the gamma DSD.

This thesis aims to use novel polarimetric radar measurements and techniques, in particular using the co-polar correlation coefficient and Differential Doppler Velocity parameters which both measure the variety of shapes being sampled by the radar, to improve our understanding of embedded mixed-phase cloud characteristics and microphysical properties. A new technique to estimate the shape parameter in the gamma DSD is also presented.

1.1 Mixed-phase clouds

Mixed-phased clouds contain both supercooled liquid water (SLW) droplets and ice crystals in the same volume. Pure liquid water droplets can exist in a supercooled state down to temperatures as low as -40°C (Yau and Rogers, 1996), before homogeneous nucleation (freezing without an ice nucleus) occurs. Between -40 and 0°C, the presence of some insoluble aerosols can initiate glaciation through heterogeneous nucleation (freezing with the aid of an ice nucleus). However, ice nuclei are relatively rare: the number monotonically increases with decreasing temperature, from about 0.1 L^{-1} at -10°C to more than 100 L^{-1} at temperatures colder than -25°C (Meyers *et al.*, 1992). Therefore, mixed-phase clouds tend to contain numerous supercooled liquid water drops with relatively few ice crystals forming within them. Due to differences in the degree of supersaturation over ice and water, these ice crystals grow rapidly at the expense of the SLW droplets via the Wegener-Bergeron-Findeisen process (Pruppacher and Klett, 1997). Ice crystal growth within mixed-phase regions is fundamental to the production of precipitation; it is estimated that most of the precipitation observed at mid-latitudes is formed in this way (Mülmenstädt *et al.*, 2015). The depletion of liquid water in the cloud can have important radiative effects, which can, in turn effect the characteristics of mixed-phase clouds and their ability to sustain further crystal growth. Despite the importance of the microphysical processes that dictate the coverage, lifetime and evolution of mixed-phase clouds, our understanding of them is poor. Consequently, so too is their representation in numerical weather and climate models (Gregory and Morris, 1996). Furthermore, mixed-phase clouds can also pose a threat to aviation in the form of aircraft icing (e.g. Politovich 1989).

1.1.1 Characteristics of mixed-phase clouds

Field *et al.* (2004) suggest that mixed-phase clouds can be classified as one of two types: those containing a thin SLW layer at cloud top (which hereafter will be referred to as Type I), and those that contain SLW embedded within a deeper ice cloud containing irregular ice particles (hereafter referred to as Type II). The schematic in figure 1.1

illustrates the difference between Type I and Type II mixed-phase cloud types. In these regions, ice crystals grow rapidly by vapour deposition, and fall out beneath (Rauber and Tokay, 1991; Hobbs and Rangno, 1998). Typically these layers are 100—200 m deep (Hogan *et al.*, 2002; Field *et al.*, 2004), but have been observed to be as deep as 700 m (Korolev *et al.*, 2007).

These mixed-phase clouds are very important for Earth's radiation balance (Hogan *et al.*, 2003a; Comstock *et al.*, 2007; Solomon *et al.*, 2007). This is because they typically consist of a high concentration of small drops, with typical effective radii of 2 to 50 μm (Crosier *et al.*, 2011), which are very reflective to incoming shortwave solar radiation (Hogan *et al.*, 2003a); the same amount of liquid water distributed amongst SLW drops is more reflective than distributed amongst fewer but larger ice crystals. The radiative importance of these liquid layers is reduced if thick ice clouds is present above them, however Hogan *et al.* (2003) estimate that in the majority of cases SLW will dominate the radiative properties of the clouds. Although outgoing longwave radiation is also reduced, the shortwave reflection by the SLW is larger. It is therefore estimated that they have a net cooling effect on Earth's climate (Hogan *et al.*, 2003).

1.1.2 Formation and maintenance

Mixed-phase clouds are formed by the cooling of an air mass to condensation below 0°C by either diabatic or adiabatic processes. This is common in convective updrafts or large scale ascent, such as that associated with mid-latitude frontal systems. Due to the Wegener-Bergeron-Findeisen process, one would expect mixed-phase regions to be inherently unstable and tend to glaciate fairly quickly. Indeed, from in-situ aircraft measurements, Korolev *et al.* (2003) showed that the ratio of ice water content to total condensed water content was typically either greater than 0.9 or smaller than 0.1 over scales of approximately 100 m. However, this is in stark contrast to recent observations of SLW layers generating ice crystals for hours (Westbrook and Illingworth, 2011a) to even days (Marsham *et al.*, 2006; Shupe, 2011; Morrison *et al.*, 2012). Mixed-phase clouds are maintained by a delicate balance between radiation, cloud dynamics, and cloud microphysical processes (Morrison *et al.*, 2012). Essentially, the cloud can

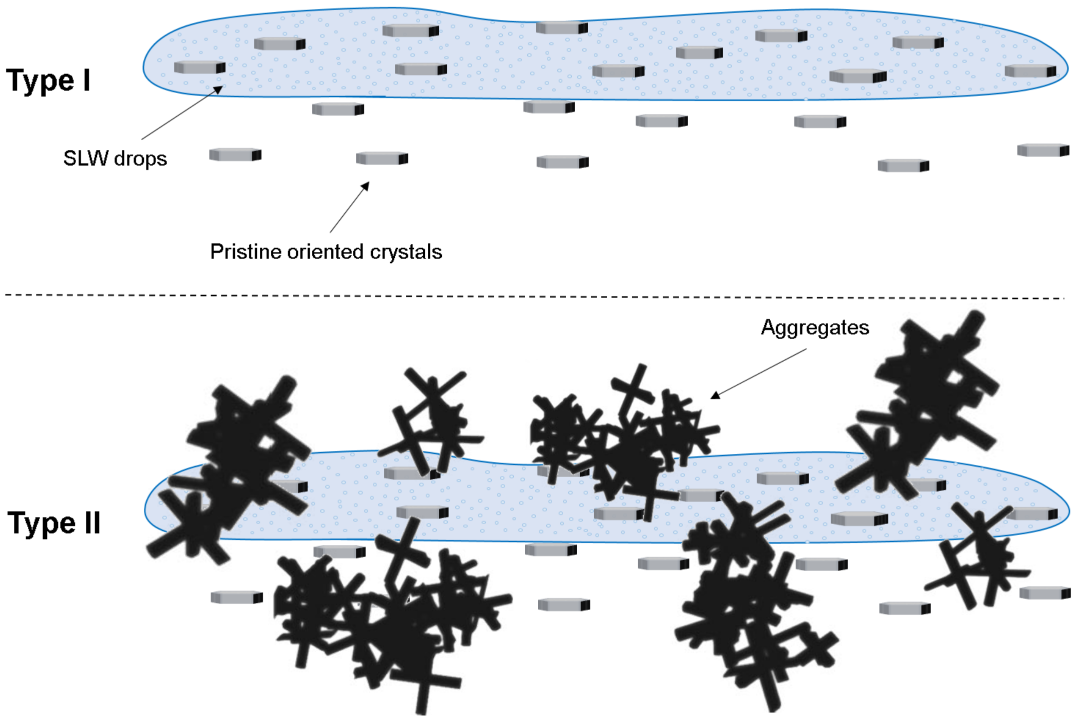

Figure 1.1 Schematic of Type I and Type II mixed-phase regions. The presence of aggregate crystals in Type II regions acts to mask the radar signal from the pristine oriented crystals.

persist as long as the rate of supply of liquid water exceeds the rate of depletion by ice formation and deposition from the cloud. It was postulated by Rauber and Tokay (1991) that mixed-phase regions could be maintained by updrafts that were sufficiently strong to bring air to saturation. The updraft speed required was larger at colder temperatures and for larger ice nuclei concentrations. However, it is known that large updrafts are typically not associated with mixed-phase clouds; typically mean velocities are close to zero (Shupe *et al.*, 2008a). More recently, Korolev and Field (2008) have suggested that liquid water can form and persist if the vertical velocity of an ice cloud parcel exceeds a certain threshold, and occurs above some threshold altitude to bring the vapour pressure of the parcel to water saturation. Longwave emission and the associated turbulence could also produce the necessary conditions to bring air to saturation in these regions. Deviations from the mean velocity can be as large as $\pm$ 2 ms^{-1}, with condensation occurring in the upward part of the turbulent eddy (Shupe *et al.*, 2008a). The formation and maintenance of Type II mixed-phase clouds is potentially complicated by other microphysical processes (such as riming, see section 1.1.5.2) that occur in deeper ice cloud.

1.1.3 Observed frequency

For the same reason that SLW layers are reflective to solar radiation, they are also very reflective at lidar wavelengths. This means that Type I clouds can be easily detected using a lidar instrument; this technique has formed the basis of estimating the observed frequency of occurrence of these clouds types. Several studies have shown mid-level mixed-phase clouds containing a SLW at cloud top (Type I mixed-phase clouds) are a relatively frequent occurrence (Hogan *et al.*, 2002, 2003a; Field *et al.*, 2004; Marsham *et al.*, 2006; Shupe *et al.*, 2008b; de Boer *et al.*, 2009; Morrison *et al.*, 2011; Westbrook and Illingworth, 2011b). Hogan *et al.* (2004) present measurements from a lidar on board a space shuttle from the Lidar In-space Technology Experiment between the latitudes of ±60°. They estimate that around 20% of clouds between -10 and -15°C contain liquid water, falling to essentially none below -35°C. Using a spaceborne lidar, Zhang *et al.* (2010) estimate that 34% of mid-level stratiform clouds contained a liquid layer at cloud top and that at any one time, these clouds covered 7.8% of the Earth's surface. They find that the fraction of mid-level clouds that are liquid topped increased as cloud top temperature decreased, and markedly so between -15 and -10°C. Both of these spaceborne lidar studies are in agreement with 18 months of near-continuous ground based lidar measurements of Hogan *et al.* (2003). They show 27% of clouds between -5 and -10°C contain significant liquid water, falling to only 6% of clouds observed between -25 and -30°C. Hogan *et al.* (2003) also estimate that the horizontal extent of the layers is typically between 20 and 70 km. More recently, from four years of continuous lidar data Westbrook and Illingworth (2011b) estimates that at -27°C, half of all ice clouds are liquid water topped, increasing to 95% for temperatures warmer than -20°C.

Multi-layered and embedded mixed-phase clouds within deep ice cloud (Type II mixed-phase clouds) have also been observed (Hogan *et al.*, 2002, 2003a; Field *et al.*, 2004; Shupe *et al.*, 2006; Morrison *et al.*, 2009; Rambukkange *et al.*, 2011). Unlike Type

I clouds, however, it is generally not possible to use spaceborne or ground-based lidar to identify this type of mixed-phase cloud as lidar wavelengths are strongly attenuated by ice or liquid clouds above or below these regions. Consequently, there are limited measurements of Type II mixed-phase clouds and statistics of their occurrence. Lidar on board an aircraft (e.g. Hogan *et al.* 2003a) or in-situ probes can be used to identify such conditions, however it is not possible to obtain longer term statistics via these methods. From approximately 1200 km of in-situ aircraft measurements and using particle sphericity as an indicator of phase, Field *et al.* (2004) estimate that liquid water is present 40% of the time in Type II clouds between -5 and -10°C, decreasing to 20% in clouds between -10 and -15°C. They also suggest high variability of mixed-phase cloud properties on the scales of 100 s of metres for Type II mixed-phase clouds.

1.1.4 Numerical modelling of mixed-phase clouds

Despite their importance and sensitivity to their specification (Mitchell *et al.*, 1989; Senior and Mitchell, 1993), mixed-phase clouds remain poorly represented in numerical weather and climate models. Part of the problem is that mixed-phase layers may be very thin; sometimes smaller than the model grid spacing (Hogan *et al.*, 2003a) and are not resolved. Current weather and climate models must rely on microphysical parameterisations of mixed-phase clouds. Their effective modelling depends on accurate representations of the ice crystal scattering properties, fall speeds and primary and secondary ice nucleation mechanisms which are uncertain (Harrington *et al.*, 1999; Jiang *et al.*, 2000; Morrison *et al.*, 2003). Good observational data on which to base these parameterisations is needed.

Recent satellite (Zhang *et al.*, 2010) and ground-based remote sensing studies (Illingworth *et al.*, 2007) have shown that numerical models typically underestimate the frequency of mid-level mixed-phase clouds. A comprehensive intercomparison between single-column and cloud-resolving model simulations has shown that although models simulate the ice water path of Type I mixed-phase clouds well, they typically underestimate their liquid water path (Klein *et al.*, 2009). They conclude that this discrepancy is the result of poor model representation of the interaction of ice microphysics with liquid microphysics. A complimentary study by Morrison *et al.* (2009) used operational and climate models to simulate deep multi-layered mixed-phase clouds (Type II clouds). They find that models tend to produce too much cloud, over-predict liquid water path, but under-predict ice water path. Furthermore, not enough liquid water is converted to ice in Type II regions, in contrast to Type I regions where this conversion was too rapid (Klein *et al.*, 2009). This disagreement suggests that the microphysics of Type I and Type II mixed-phase clouds may be quite different, and implies a lack of understanding of the microphysical processes occurring within mixed-phase clouds. Current observations are inadequate to correct evident errors in representation of mixed-phase clouds (Fridlind *et al.*, 2007). One of the primary aims of this thesis is to present new observations of Type II mixed-phase clouds which could help improve our understanding of the microphysics in these regions and address these model shortcomings.

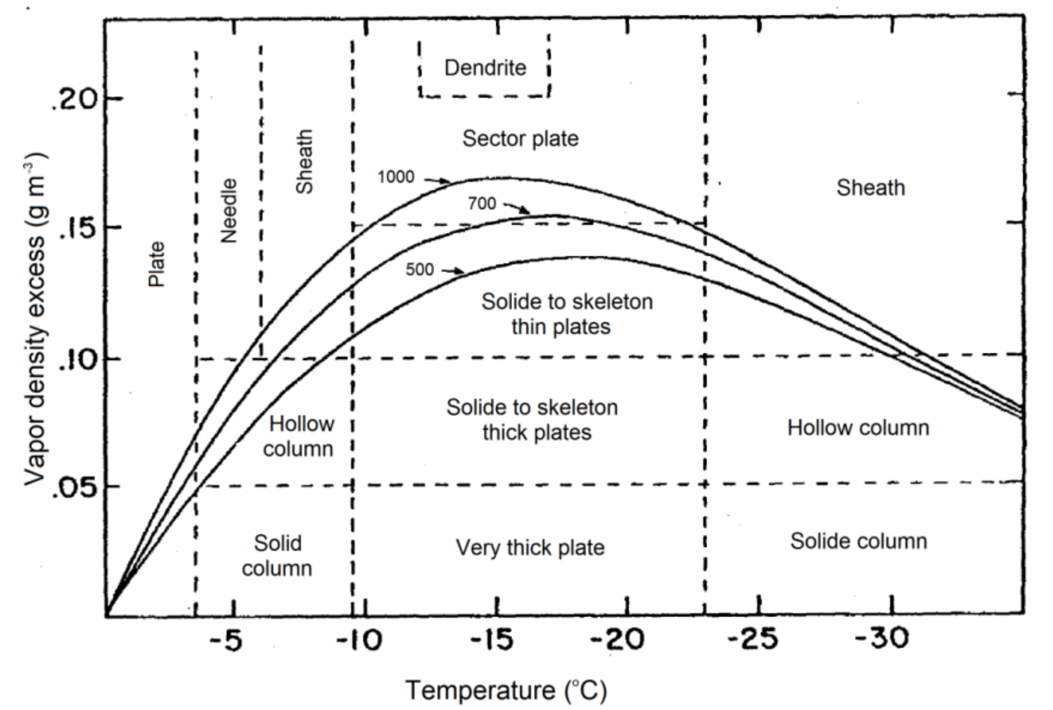

Figure 1.2 The effect of environmental temperature and supersaturation on ice crystal habit. Image from Young (1993).

1.1.5 Ice microphysics

The heterogeneous nucleation of pristine oriented crystals (that is, nucleation due to the presence of ice nuclei) is fundamental to the microphysical evolution of the cloud (Westbrook and Illingworth, 2011b; De Boer *et al.*, 2011). Ice crystals take the form of a vast range of shapes and sizes in the atmosphere. The precise temperature, pressure and humidity at which they are nucleated determines their shape and density (Fukuta and Takahashi, 1999; Bailey and Hallett, 2009). However, they all have a common basic shape of a hexagonal prism. The preferential axis of growth is a function of the temperature and supersaturation of the environment in which the crystal forms. The habit is determined by the slowest growing ice crystal faces. Figure 1.2 from Young (1993) shows how supersaturation and temperature effects the ice crystal habit. In general, crystals growing between approximately -22 and -9°C tend to be plate-like, between -9 and -4°C columnar, and plate-like again warmer than -4°C. In regions of high supersaturation where there are very large vapour density gradients, columns can become needles or sheaths (hollow columns) and plates can grow extensions and branches (Magono *et al.*, 1966). Figure 1.3 shows a schematic of a plate (left) and a column (right) crystal. Both are depicted with their major axis aligned horizontally as they would be in the atmosphere (see section 1.1.5.4).

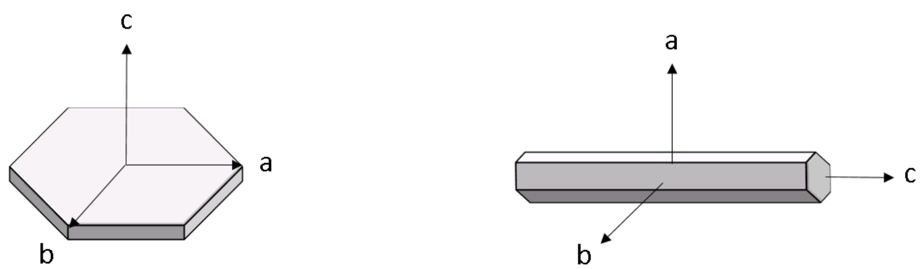

Figure 1.3 Schematic of a plate crystal (left) and column crystal (right). Due to aerodynamics these crystals fall with their major axis horizontally. For plates, this axis is either a or b, for columns it is c.

Until recently, it was thought that the dominant crystal habit below -22°C was columnar. However, more recent laboratory and aircraft cloud imaging probe data reveals that below -22°C there are two distinct habit regimes: plate-like crystals between -40 and -20°C, and columnar types between -70 and -40°C. Figure 1.4 shows the comprehensive ice crystal habit diagram; most crystals below -22°C are in fact polycrystals with complex, irregular shapes. Unlike in a laboratory, ice crystals in the real atmosphere can fall through many different temperature and saturation environments throughout their lifetime, causing more complicated shapes. It was shown by Korolev *et al.* (2000) that in thick stratiform ice cloud, 84% of ice particles larger than 125 μm are irregularly shaped polycrystals or aggregates (Stoelinga *et al.*, 2007) and that pristine crystals occurred relatively infrequently, and typically embedded within larger zones of these irregularly shaped crystals on scales of approximately 100 m.

1.1.5.1 Growth by vapour deposition

The saturation vapour pressure for ice is smaller than that for water. Therefore, in mixed-phase conditions (in the absence of any source of supersaturation) the air is super-saturated with respect to ice, but sub-saturated with respect to liquid water. This causes the ice crystals to grow rapidly by vapour deposition at the expense of SLW drops via the Wegener-Bergeron-Findeisen mechanism (Pruppacher and Klett, 1997). The growth rate for any given crystal (assuming steady state conditions) is given analytically by Yau and Rogers (1996):

$$\frac{dM}{dt} = \frac{4\pi C(S_i - 1)}{\frac{L_s^2}{KR_vT^2} + \frac{R_vT}{e_i(T)D}} \tag{1.1}$$

where M is crystal mass (kg), C is the capacitance of the ice crystal, (S_i-1) is the degree of supersaturation of the air with respect to ice, L_s is the latent heat of sublimation, K is the thermal conductivity of the air, R_v is the gas constant for water vapour, e_i is the vapour pressure over ice, D is the diffusion coefficient for water vapour in air and T is the temperature. The capacitance of any given crystal is a function of its shape and size; crystals with large aspect ratios have the largest capacitance for a given mass, and so grow very rapidly (Westbrook, 2008).

Figure 1.5 shows predicted ice crystal growth rate by vapour deposition as a function of temperature normalised by C. The maximum difference between the saturation vapour pressures over ice and water occurs at -12°C. However, the maximum growth rate occurs a few degrees colder at approximately -15°C over a wide range of pressures. This is because local heating from latent heat release reduces the vapour pressure difference (Pruppacher and Klett, 1997). Typical lengths of columnar crystals and diameters of plate-like crystals growing by vapour deposition are 20—2000 μm. Columns widths are typically 10—200 μm, and the thickness of hexagonal plates and dendrite crystals is typically 10—60 μm (Pruppacher and Klett, 1997). Under vapour depositional growth, the diameter and thickness of plate-like crystals and length and width of columnar crystals are related.

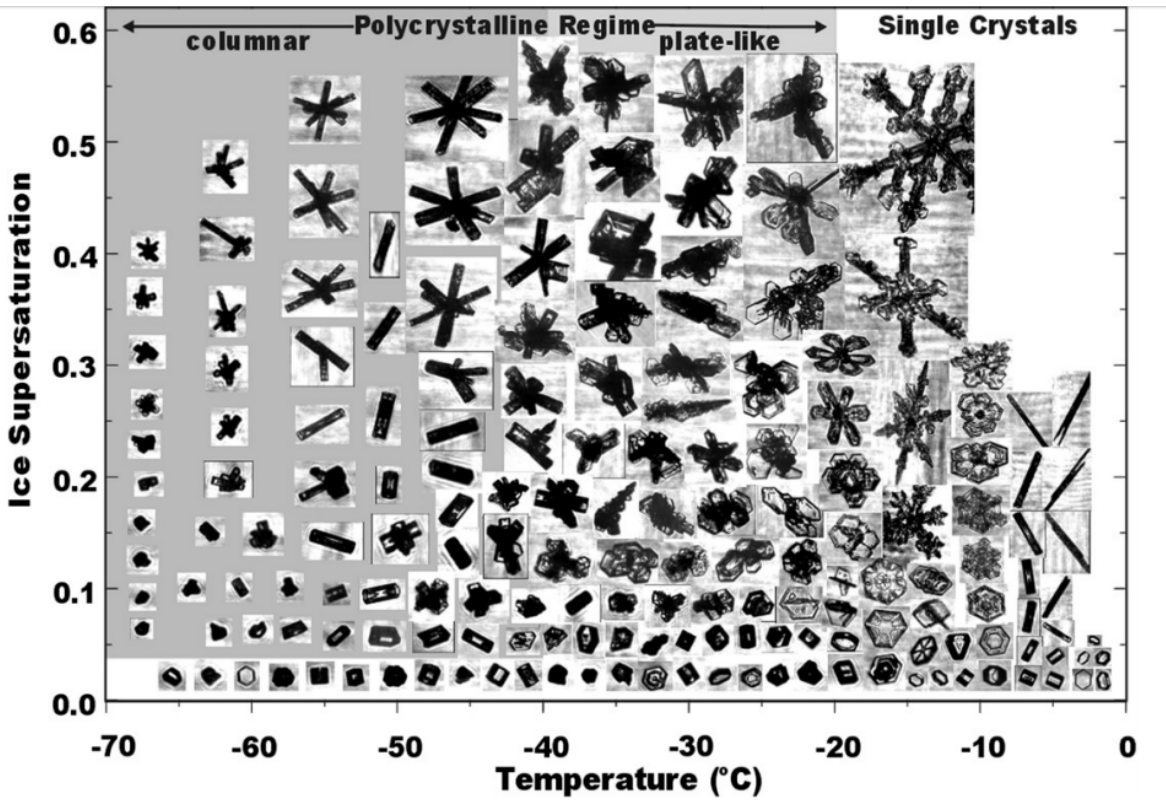

Figure 1.4 Crystal habit diagram from Bailey and Hallett (2009).

1.1.5.2 Riming

Once crystal have grown to a sufficient size by vapour deposition, further growth of ice crystals can occur by the collection of SLW drops as the ice crystal falls through the

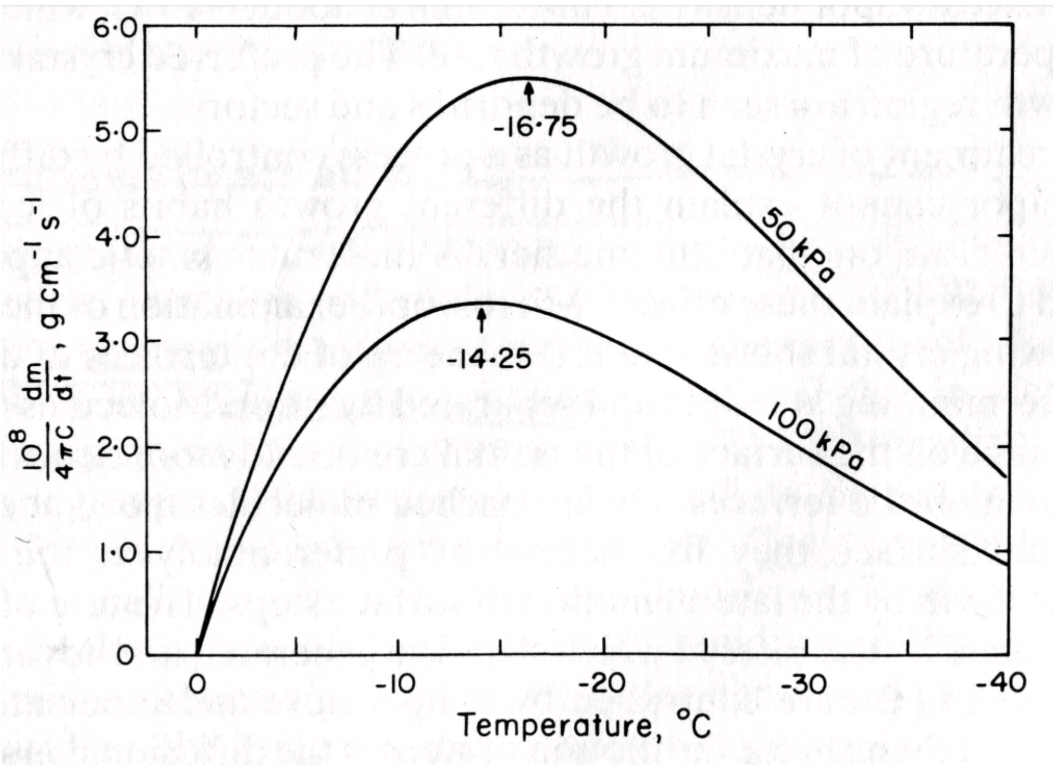

Figure 1.5 Ice crystal growth rate by vapour deposition as a function of temperature and pressure. Image from Yau and Rogers (1996).

atmosphere, known as accretion, or riming. Laboratory studies estimate that columnar crystals must have a minor axis of 50—90 μm before the onset of riming, and plate crystals must grow to between 300—400 μm in diameter (Ono, 1969). The riming droplets also need to be larger than approximately 10 μm (Harimaya, 1975). More recently, a modelling study has estimated that the onset of riming occurs for columns once their minor axis is greater than 70 μm, and for hexagonal plates and broad-branched crystals when their major axes are 220 μm and 400 μm respectively (Wang and Ji, 2000). The growth rate by this mechanism depends on the cross sectional area of the crystals, and the collision efficiency with SLW droplets. The resulting increase in mass of rimed crystals causes them to have higher terminal velocities than unrimed particles of the same size (Locatelli and Hobbs, 1974). Riming is also thought to be important for ice multiplication processes at warmer temperatures, though splintering of ice crystals on impact with SLW drops (Hallett and Mossop, 1974).

1.1.5.3 Aggregation

Aggregation is a key process governing precipitation growth in ice clouds. Differential sedimentation rates of ice crystals (due to differences in sizes and shapes) lead to the chance of collision and sticking of ice crystals. The overall aggregation rate is a function of the collision rate, and the "sticking efficiency" of the crystals which depends on the ice crystal shape and the environmental temperature (Pruppacher and Klett, 1997). There are two mechanisms by which aggregation can occur given a collision between particles: bonding across the surface of contact or the inter-locking together of different crystals. The first process typically occurs at temperatures warm enough for the crystals to become water-coated. Evidence suggests that the locking together of ice crystals is most efficient for crystals with dendritic structures; these two aggregation modes are found in aircraft observations of Hobbs *et al.* (1974), where two peaks in maximum aggregate sizes are observed between -5 and 0°C as the crystals become water coated, and between -15 and -10°C, the temperature range where dendritic crystals are known to occur.

Aggregates crystals are typically 1—5 mm in size, but can reach 15 mm (e.g. Hobbs *et al.*, 1974). The effective density of aggregates is typically much less than for pure ice as their volume largely consists of air. Their density decreases inversely to the maximum dimension (Brown and Francis, 1995), and is typically very low, most frequently between 0.01 and 0.2 gcm^{-3} (Pruppacher and Klett, 1997), compared to the density of pure ice, which is 0.917 gcm^{-3}. This has important implications for radar observations of ice clouds, which is discussed in section 1.3.2.

1.1.5.4 Crystal fall speeds and orientation

The terminal fall speeds of ice particles are a function of their size, mass and shape. There are many documented fall speed-dimension power-laws that relate crystal properties such as surface area or mass to their fall speed (e.g Hobbs *et al.* 1974; Mitchell 1996). Figure 1.6 shows terminal fall speeds for various plate-like crystals computed from drag coefficients in then laboratory (from Kajikawa 1972). Higher density crystals with smaller surface areas tend to fall quickly for a given size; dendritic crystals with lower densities (compared to their surface area) fall more slowly for a given size. The terminal fall speeds of columns tends to be larger than plates. The terminal fall speeds of unrimed crystals are typically less than 1 ms^{-1} (Kajikawa, 1972). Conversely, aggregate crystals (which have larger mass) generally have terminal fall speeds larger than 1 ms^{-1} once their diameter is greater than 1 mm (Locatelli and Hobbs, 1974).

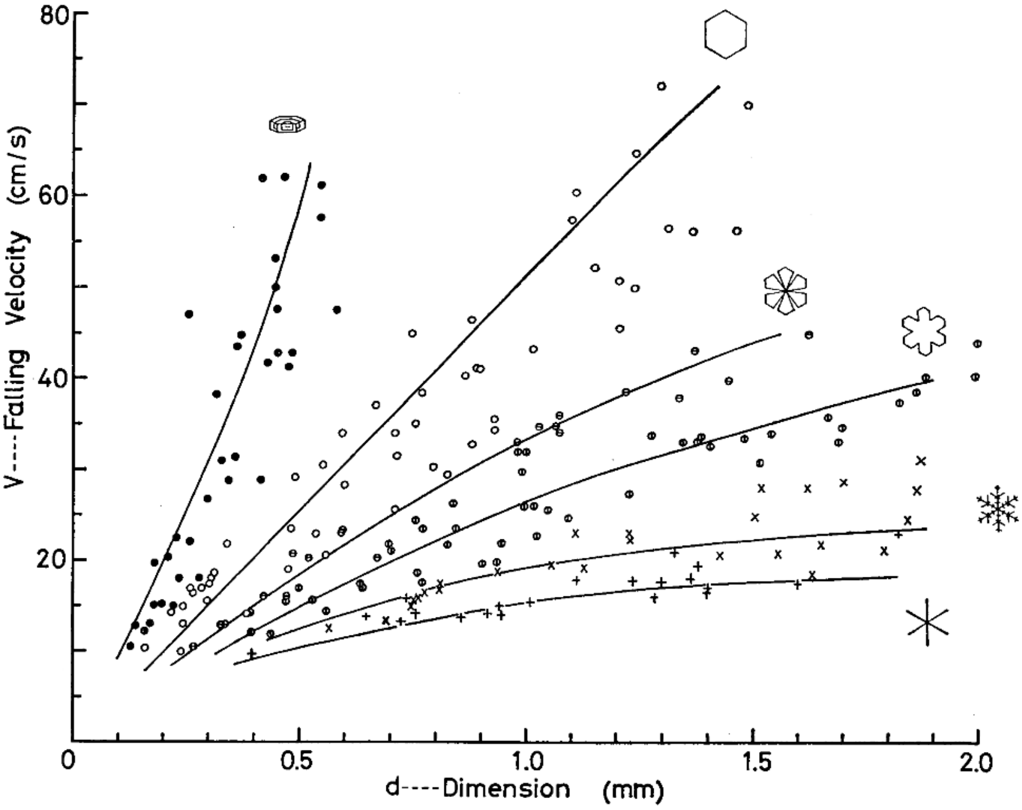

Figure 1.6 Terminal velocities of different planar crystal shapes, computed from drag data at -10°C, 1000 mb. Image from Kajikawa (1972).

Pristine ice crystals falling through the atmosphere with Reynold numbers between 1 and 100 tend to be oriented with their major axis aligned horizontally (Sassen, 1980; Cho *et al.*, 1981; Pruppacher and Klett, 1997). In this regime, symmetrical vortices are formed in the wake of the crystals, such that if the ice crystal inclination angle deviates from the horizontal plane, a re-orienting torque acts to return the crystal to the horizontal plane (Willmarth *et al.*, 1964). This convenient property means that pristine crystals are aligned in such a way that they can be easily detected with polarimetric radar; the exploitation of this property is fundamental to this thesis. For very large crystals (Reynolds number larger than 100), the inertial forces become too strong to be damped, resulting in irregular tumbling motions (Willmarth *et al.*, 1964; Kajikawa, 1992). Fluttering can also be occur for Reynolds numbers as low as 40 if particles have some asymmetry (Kajikawa, 1992). The magnitude of this flutter is thought to vary significantly, estimates of hexagonal plates range from 0.3° (Thomas *et al.*, 1990) to 20° (Melnikov and Straka, 2013). Large aggregate crystals can tumble dramatically (Kajikawa, 1982).

1.2 Rain drop size distributions

Another problem which is long-standing in the field of radar meteorology is the accurate retrieval of rain rates from weather radars. An accurate estimation of rain rate and accumulation is important for many industries (e.g. agriculture), and public flood warnings.

Accurate knowledge of the DSD is important for retrievals of rain rate using weather radars, and for the modelling of a variety of rain formation and growth processes such as accretion and collision-coalescence, and depletion of liquid water through evaporation. Traditionally, a single polarisation radar (see section 1.3) has been used to relate the observed radar reflectivity (Z) to the rain rate (R), via empirical expressions of the form:

$$Z = aR^b \tag{1.2}$$

However, rain rates estimated in this way suffer from errors due to uncertainty in the characteristics of the drop size distribution. Using radar reflectivity from a single polarisation radar, it is not possible to know whether the backscattered power is the result of many small drops, or a few large drops in the radar sampling volume. Natural rain DSDs can be described by a gamma distribution (Ulbrich, 1983):

$$N(D) = N_0 D^{\mu} \exp\left[-\frac{(3.67+\mu)}{D_0} D\right] \tag{1.3}$$

where D is the equivalent spherical drop diameter, N_0 is the intercept parameter, D_0 is the median volume drop diameter and μ is the dispersion parameter (a measure of the drop size spectrum shape). Dual polarisation radar allows the backscatter in the vertical polarisation to also be measured. Differential reflectivity is the ratio of backscattered power in the horizontal polarisation to the vertical polarisation (see section 1.3.2); this is related to the mean drop shape in the radar pulse volume. Figure 1.7 shows how drops become increasingly oblate as they become larger, due to aerodynamic effects (Beard *et al.*, 2010). If μ is known a-priori, by exploiting this relationship,

D_0 can be estimated using Z_{DR} (Seliga and Bringi, 1976), which better constrains the DSD and can help improve rain rate estimates.

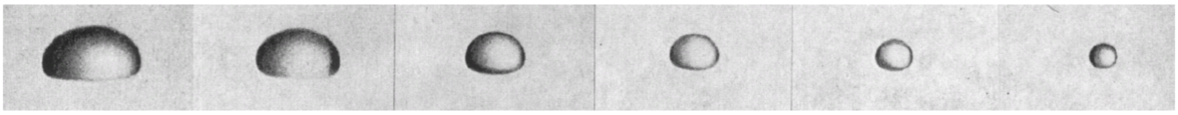

Figure 1.7 Shape of large drops falling at terminal velocity having equivalent spherical diameters of D = 8.00, 7.35, 5.80, 3.45 and 2.00 mm. Image from Beard *et al.* (2010).

However, without knowledge of the shape parameter, μ, it is still not known whether drops in the pulse volume are centered about this median drop size, or whether there is a large spread in drop sizes. Higher μ corresponds to more monodisperse drop size distributions, whereas lower μ corresponds to broader DSDs. Since larger drops have the largest volume, they contribute most to rain rate, and DSDs with lower μ for a given median drop diameter produce higher rain rates. Unfortunately, retrievals of rain rate are sensitive to variability in the shape of the drop size spectrum. Figure 1.8 shows rain rate (R) per unit radar reflectivity (Z) as a function of Z_{DR} for simulated gamma distributions with μ equal to -1, 0, 2, 4, 8, 12 and 16. Uncertainty in μ alone could introduce an error in the retrieved rain rate of up to 2.5 dB (almost a factor of 2) for a given pair of Z and Z_{DR} observations.

Typically, ground based disdrometer instruments have been used to relate D_0 to μ statistically. These instruments fundamentally work by counting the number of drops that fall within certain drop size bins over certain period of time, typically 1 minute. From this, moments of the DSD can be estimated. However, it is difficult to obtain reliable estimates of μ from disdrometers as they suffer from undersampling of large drops; this, for example, makes μ values that are derived from the 3$^{\text{rd}}$, 4$^{\text{th}}$ and 6$^{\text{th}}$ moments of the drop size distribution biased high (Johnson *et al.*, 2014). Furthermore, disdrometers also undercount the number of drops with diameters smaller than 0.5 mm (Tokay *et al.*, 2001), which can also introduce a bias in estimates of μ. Estimating DSD parameters using radar is preferable over disdrometers due to the very large number of drops being sampled. In this thesis, new estimates of μ are made using a new radar variable defined in chapter 3, which has the potential to improve dual polarisation

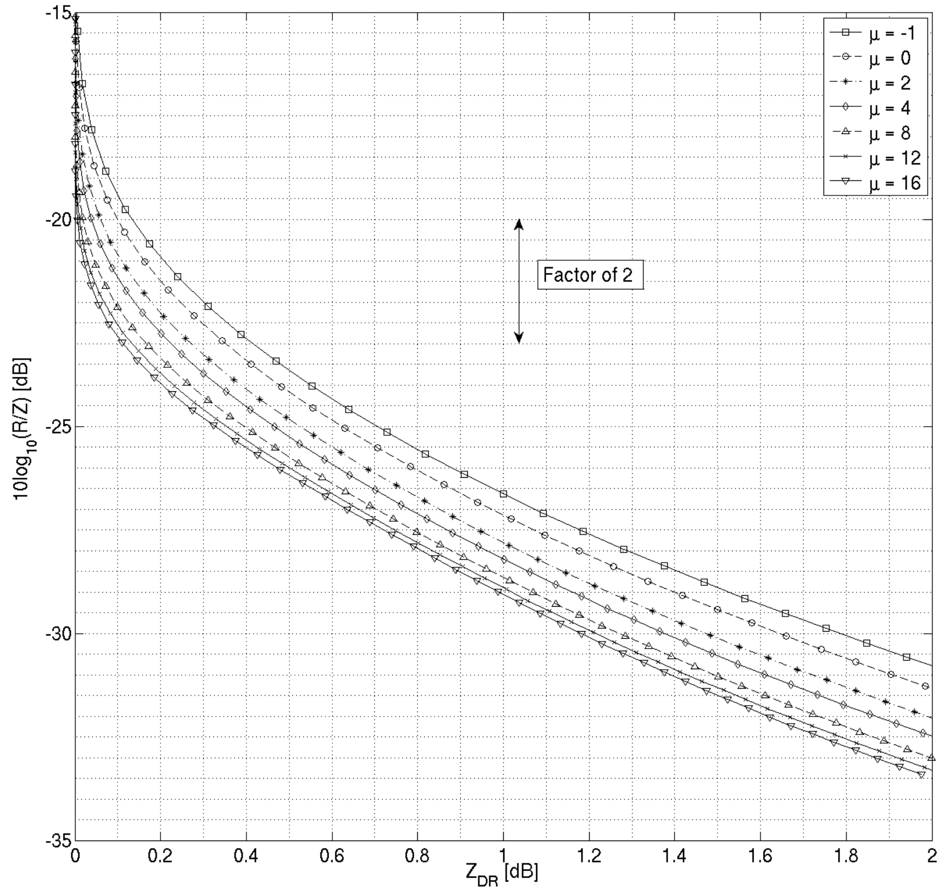

Figure 1.8 Rain rate (in dB referenced to 1 mm hr^{-1}) per unit radar reflectivity as a function of Z_{DR} computed using Gans theory for gamma distributions of μ = -1, 0, 2, 4, 8, 12 and 16. The rain rate can vary by almost a factor of 2 for a given pair of Z and Z_{DR} observations as a result of drop spectrum shape variability.

radar retrievals of rain rate.

1.3 Dual-polarisation radar

Dual polarisation radar is a powerful tool for investigating the microphysics of clouds and precipitation. In this section, principles of dual polarisation radar and the polarimetric variables that are used in this thesis are introduced.

Radar instruments fundamentally work by transmitting an electromagnetic pulse and receiving an echo after some time delay, which allows the distance of the backscattering particles to be identified. Single polarisation radars typically transmit a polarised electromagnetic pulse in the horizontal or vertical polarisation, defined by the plane of the electric field of the wave ($\vec{E}$, which is always perpendicular to direction of propagation). Upon interacting with liquid water, ice, or non-meteorological targets, an amount of this radiation is backscattered to the radar. Weather radars typically use centimetre wavelengths so that the wavelength is much larger than the diameters of the hydrometeors ($\lambda \gg D$) and scattering occurs predominantly in the Rayleigh regime. The radar measures the backscattered electric field, which for a single particle can be related to incident electric field through the backscattering matrix (S) by:

$$\begin{bmatrix} E_h \\ E_v \end{bmatrix}^b = \begin{bmatrix} S_{hh} & S_{hv} \\ S_{vh} & S_{vv} \end{bmatrix} \times \begin{bmatrix} E_h \\ E_v \end{bmatrix}^i \frac{e^{-ik_0 r}}{r} \tag{1.4}$$

where $E^b$and E^i are the backscattered and incident electric fields respectively, k_0 is the wavenumber, r is the range (Doviak and Zrnic, 2006). The elements of S are inherent to the particle causing the backscattering; they contain information regarding the size, shape, orientation and dielectric factor of the hydrometeors. The subscripts correspond to the received and transmitted polarisations respectively. Thus, the measured backscattered electric field can be related to the hydrometeors causing the backscatter.

1.3.1 Radar reflectivity factor (Z)

The radar reflectivity in the horizontal polarisation for a single particle is given by:

$$Z_H = (4\lambda^4/\pi^4|K|^2)|S_{hh}|^2 \tag{1.5}$$

where $|K|^2$ is the dielectric factor of the particle (which is approximately 0.93 for water, and approximately 0.21 for ice, but also depends on wavelength and temperature (Yau and Rogers, 1996)). In the Rayleigh regime, the radar reflectivity for an ensemble of hydrometeors is proportional to the sixth power of the diameter and linearly to their number, defined per unit radar sampling volume as:

$$Z = \int_0^\infty \frac{|K_i^2|}{0.93} N(D) D^6 dD \qquad [\mathrm{mm^6 m^{-3}}] \tag{1.6}$$

where $|K_i|^2$ is the dielectric factor of the ith particle, and D is the equivalent hydrometeor diameter. The higher dielectric factor for water means that rain drops have a higher radar reflectivity than ice particles of the same size. Since Z varies over orders of magnitude, it is more often expressed in logarithmic units as:

$$Z[\mathrm{dBZ}] = 10\log_{10}(\mathrm{Z[mm^6m{-}3]}) \tag{1.7}$$

Thus, due to the very strong dependence of backscatter on particle diameter (D^6), a small number of large particles in the sampling volume can dominate the received radar signal. It is also not possible to tell whether the backscatter is caused by many smaller hydrometeors or fewer larger ones.

1.3.2 Differential reflectivity (Z_{DR})

Dual polarisation radar works in the same way as a single polarisation radar, however also transmits and receives a vertically polarised wave. This can be either through an alternate H and V pulse transmission and reception (which is the case for both the radars used in this thesis), or more commonly simultaneous transmission of both polarisations using a 45° polarisation, and receiving in both the H and V channels simultaneously. This additional measurement provides information about particle shape. Differential reflectivity is defined as the ratio of radar reflectivity factors in the horizontal (H) and vertical (V) polarisations:

$$Z_{DR} = 10\log_{10}\left(\frac{Z_H}{Z_V}\right) \quad [\mathrm{dB}] \tag{1.8}$$

It is therefore a measure of the size, shape, density and alignment of hydrometeors (Seliga and Bringi, 1976). It is independent of the number concentration, but is reflectivity-weighted, therefore dominated by larger particles in the sampling volume. Positive values occur when the backscatter in the H polarisation is larger than in the V polarisation. This is the case for oblate rain drops or ice crystals aligned with their major axis horizontally aligned. In rainfall it can be used to improve rain rate estimates due to the unique relationship between drop size and shape (Seliga and Bringi, 1976).

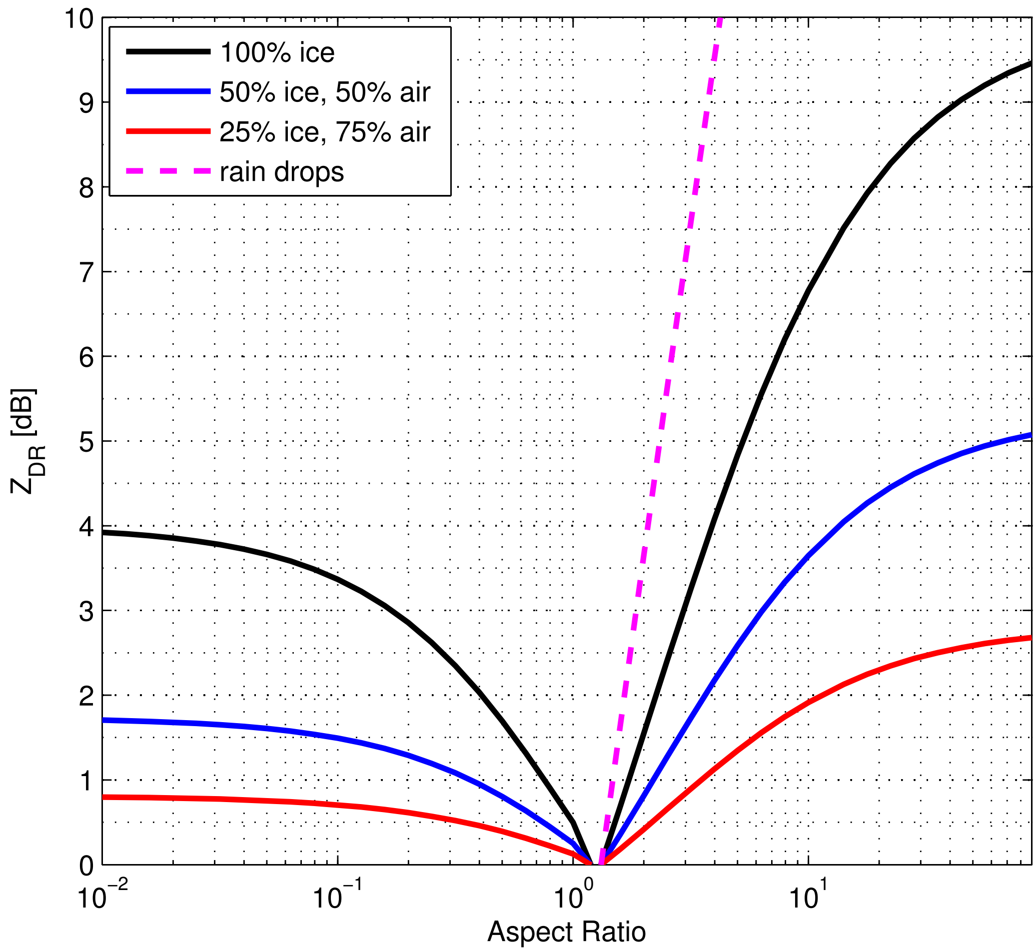

Figure 1.9 Differential reflectivity of ice particles (solid lines) and water drops (dashed) as function of their aspect ratio. Particles are aligned horizontally. Columns are assumed to have a random azimuth orientation.

Its interpretation in ice clouds however, is more ambiguous; the shapes and sizes of ice particles are generally not related. Figure 1.9 shows the differential reflectivity for ice particles of various axial ratios (axes c divided by axis a in figure 1.3) and densities, and rain drops (dashed magenta lines). Due to their high density, "pristine" crystals aligned with their major axes horizontally can produce very large Z_{DR} signatures. This is particularly true of plates, which produce the same backscatter in the H and V polarisations at any azimuthal orientation; the maximum possible Z_{DR} for extremely oblate particles (plates can be considered as such) has been calculated to be 10 dB (e.g. Hogan *et al.*, 2002). Columns, however, fall with random azimuthal orientation. The backscatter in the V polarisation is constant at all azimuths. However, the backscatter in the H polarisation for a distribution of columns is equal to the backscatter integrated over all azimuths. The maximum possible Z_{DR} from these crystals is consequently less, and is approximately 4 dB. The larger the volume fraction of air in these crystals, the lower their density and dielectric constant, hence the lower the Z_{DR} measurement. Aggregate crystals consist largely of air hence have low density. Consequently they typically produce a low Z_{DR} (0 — 0.5 dB). Their large size means that even a low number of these crystals can dominate the Z_{DR} signal from smaller pristine crystals (Bader *et al.*, 1987). A technique is developed in chapter 4 which addresses this problem.

1.3.3 The co-polar correlation coefficient (ρ_{hv})

The co-polar correlation coefficient (ρ_{hv}) is defined as (Bringi and Chandrasekar, 2001):

$$\rho_{hv} = \frac{\sum S_{HH} S_{VV}}{\sqrt{\sum |S_{HH}|^2 + \sum |S_{VV}|^2}}. \tag{1.9}$$

where $\sum S_{HH}$ and $\sum S_{VV}$ are the sums of the co-polar elements of the backscattering matrix from each particle in the radar sample volume. It can be estimated by cross correlating successive power or complex (in-phase, I, and quadrature, Q) measurements. ρ_{hv} is a measure of shape diversity within a sample volume. This property makes it complimentary to hydrometeor shape measurements of Z_{DR}. Typical values in rain are greater than 0.98, 0.9—1 in ice, and larger than 0.9 in the melting layer since it contains a variety of shapes and phases (Caylor and Illingworth, 1989). It is therefore useful for applications such as identifying the melting layer (Caylor and Illingworth, 1989; Brandes and Ikeda, 2004; Tabary *et al.*, 2006; Giangrande *et al.*, 2008), ground clutter (e.g. Tang *et al.* 2014), rain-hail mixtures (Balakrishnan and Zrnic, 1990) and interpreting polarimetric signatures in ice (e.g. Andrić *et al.* 2013), and potentially the retrieval of the drop size distribution (DSD).

This variable is used extensively in this thesis. It is discussed in more detail in chapter 3, along with practical aspects of its measurement.

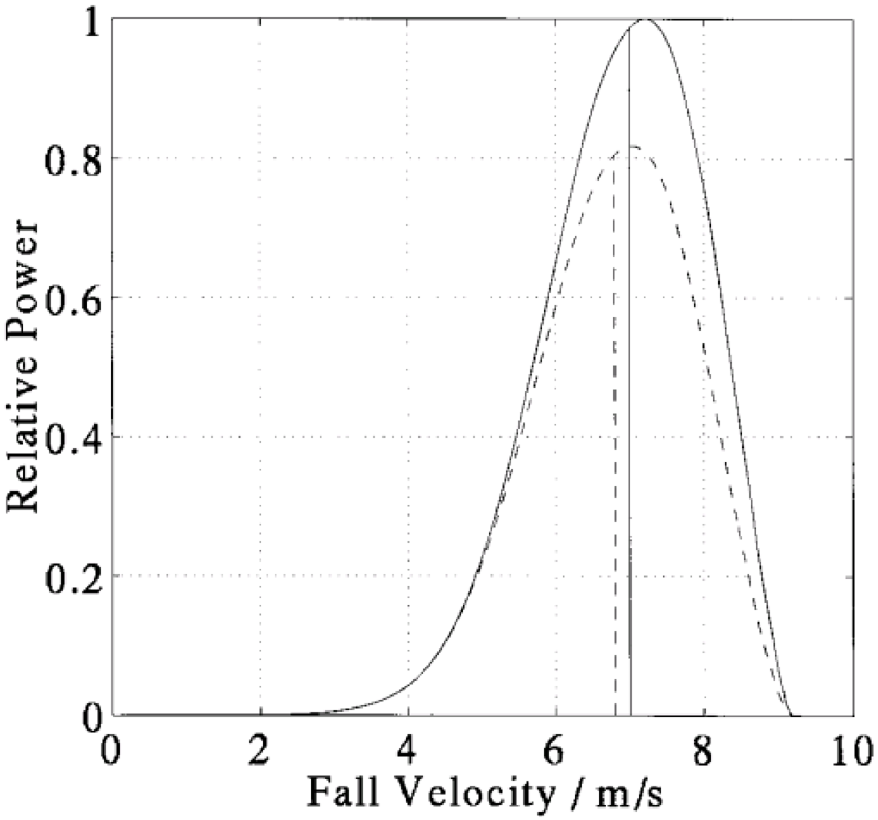

Figure 1.10 A schematic of backscattered power spectra in horizontal (solid) and vertical polarizations (dashed) in rainfall. The vertical lines represent the mean fall velocities. Figure from Wilson *et al.* (1997).

1.3.4 Differential Doppler Velocity (DDV)

Differential Doppler velocity was first introduced by Wilson *et al.* (1997). It is defined as the difference in polarisation estimates of the Doppler velocity:

$$DDV = \frac{U_H - U_V}{\sin\theta} \tag{1.10}$$

where U_H and U_V are the Doppler velocity estimates in the H and V polarisations respectively. It is necessary to divide this difference by sine of the elevation angle θ, to obtain "equivalent" estimates at vertical incidence. The elevation angle must be sufficiently large (above 10°) that there is a component of the fall speeds of particles parallel to the radar beam. Like ρ_{hv}, DDV is sensitive to mixtures of particle shapes within a sampling volume Essentially, it is a measure of whether the more aligned particles in the sample volume are falling faster or slower than the mean. Figure 1.10 shows a schematic of backscattered power spectra for H and V polarisations in rainfall. Larger drops fall more quickly than smaller drops and are also more oblate (Beard *et al.*, 2010) so have larger Z_{DR}. Since estimates of the Doppler velocity are reflectivity-weighted, and the larger drops are falling more quickly, the fall velocity estimate in the H polarisation will be larger than that in the V polarisation, and U_H - U_V will be positive. Note that the convention adopted in this thesis is that Doppler velocity is positive *away* from the radar. Therefore, in rain, this would produce a *negative* DDV estimate. If, on the other hand, the aligned particles are falling more slowly than the mean, estimates of DDV will be *positive*.

1.3.5 Radars used in this thesis

Two radars used extensively in this thesis are the S-band (3 GHz) Chilbolton Advanced Meteorological Radar (CAMRa) and the Ka-band (35 GHz) Copernicus cloud radars. A photograph of these radars is shown in figure 1.11. Both of these radars are dual polarisation and Doppler-capable. CAMRa boasts a very large antenna (25 m), making it the world's largest fully steerable meteorological radar. The resulting narrow one-way half power beamwidth (0.28°) makes it capable of very high resolution measurements. The radar is a coherent-on-receive magnetron system, transmitting and receiving alternate H and V polarised pulses with a pulse repetition frequency (PRF) of 610 Hz. A cubic polynomial interpolation is used to estimate the H power at the V pulse timing and the V power at the H pulse timing. The sensitivity of the radar is -40 dBZ at 1 km. The full capabilities of this radar are discussed in Goddard *et al.* (1994). The Copernicus radar, unlike CAMRa, typically operates continuously pointing at zenith. It has a 2.4 m antenna, which gives it 0.25° one-way half power beamwidth. Its sensitivity is approximately -35 dBZ at 1 km. Copernicus has a much higher pulse repetition frequency than CAMRa, giving it a much shorter maximum unambiguous range. Its shorter wavelength gives it a higher number of independent radar pulses per unit time, but this also means that the beam can be significantly attenuated by heavy rain and melting ice; attenuation is negligible at S-band. The full specifications of these radars

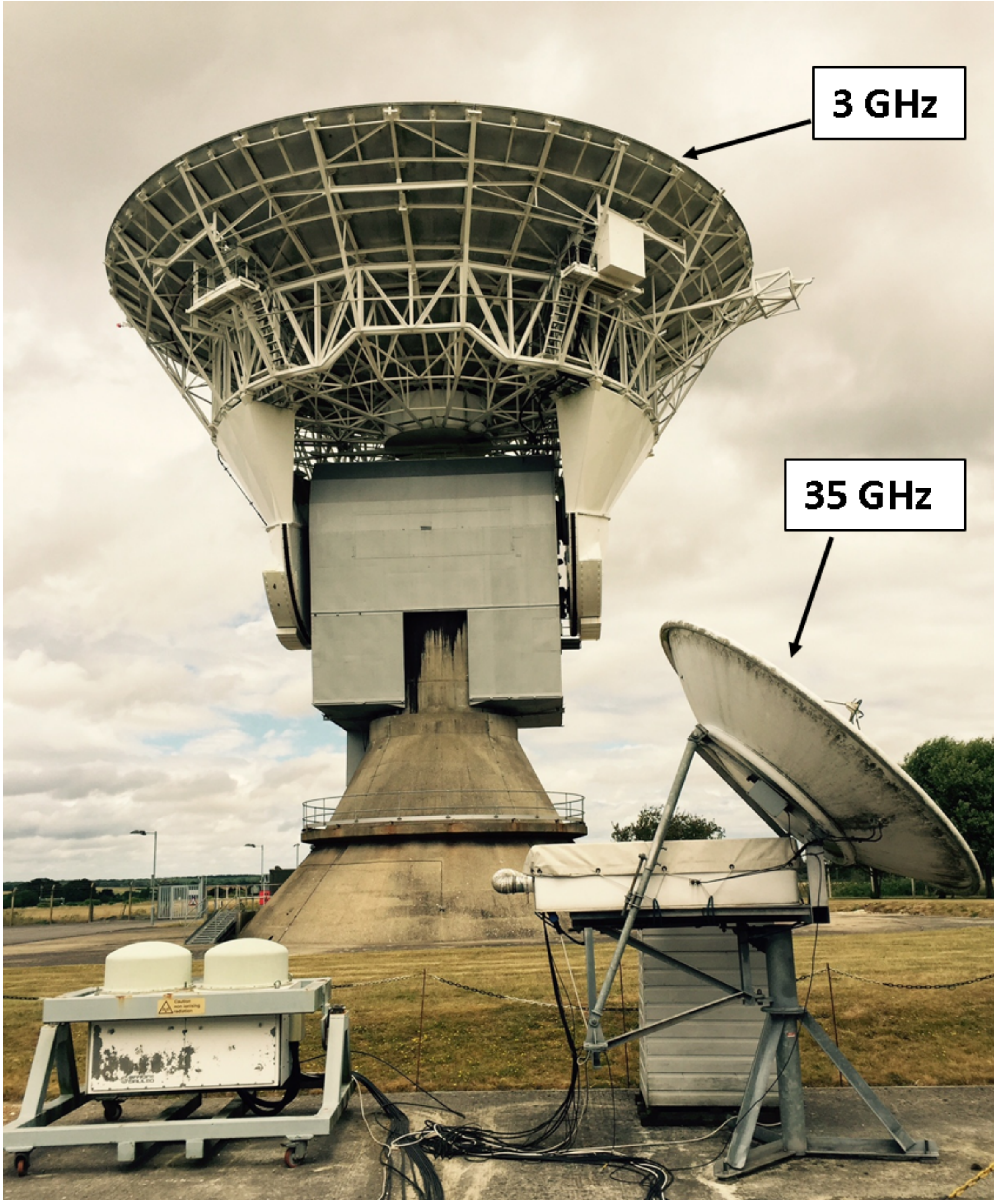

Figure 1.11 A photograph of the 3 GHz Chilbolton Advanced Meteorological Radar (CAMRa) and the 35 GHz (Copernicus) cloud radar installed at the Chilbolton Observatory.

are shown in table 1.1.

	CAMRa	Copernicus
Frequency	3 GHz	35 GHz
Wavelength	9.75 cm	8.6 mm
Antenna diameter	25 m	2.4 m
Half-power beamwidth	0.28°	0.25°
Pulse width	0.5 μs	0.4 μs
Range resolution	75 m	60 m (oversampled to 30 m)
PRF	610 Hz	10 KHz
Peak power	560 kW	1 kW

Table 1.1: Specifications of the radars used extensively in this thesis.

1.4 Thesis Outline

The aim of this thesis is to develop polarimetric radar observational and retrieval techniques to address the problems outlined above. It is organised as follows: In chapter 2, 10 weeks of continuous polarimetric radar observations will be presented, and the the frequency of occurrence of Type II mixed-phase clouds estimated. In chapter 3, a new variable $L = -\log_{10}(1 - \rho_{hv})$ is defined, which has preferable statistical properties to ρ_{hv} and allows it to be used quantitatively. Chapter 4 will then use this new radar variable in a novel retrieval technique that allows the microphysical properties of Type II mixed-phase clouds to be retrieved. Chapter 5 will also use this new variable in a new technique to retrieve μ in the rain drop size distribution. Finally, chapter 6 will summarise these results and propose future work.

Chapter 2

Statistics of Type II mixed-phase clouds

2.1 Motivation

The fundamental properties and the frequency of occurrence of Type II mixed-phase clouds are not well understood. One of the main reasons for this lack of understanding is an absence of good observational datasets. The purpose of this chapter is to present a statistical description of ice and mixed-phase cloud from 10 weeks of continuous radar measurements. Data was collected between the dates of 14 July to 21 September 2015 using the dual-polarised, Doppler capable Copernicus 35 GHz radar installed at Chilbolton. The radar was tilted to 45° elevation, allowing both polarimetric and Doppler information to be collected.

The key polarimetric variables of interest in this chapter are differential reflectivity (Z_{DR}) and Differential Doppler Velocity (DDV) at vertical incidence, defined as the difference in the Doppler velocity estimates in the H and V polarisations respectively divided by the sine of the elevation angle (Wilson *et al.* 1997, see section 1.3.4 for more details). This variable has received very little attention in the literature, although Doppler spectral measurements of Z_{DR} have been used to categorise particle habits in mixed-phase clouds (e.g. Dufournet 2010). In a similar way, DDV has the potential to be useful for investigating mixed-phase clouds due to its sensitivity to hydrometeor fall speeds and shapes. Since Doppler velocity is reflectivity-weighted, estimates are weighted by the larger particles in the sample volume. The relationships between hydrometeor shape, size and their corresponding fall speeds makes DDV complimentary to measurements of Z_{DR}. As discussed in chapter 1, the convention in this thesis is that positive Doppler velocities are away from the radar, therefore faster falling particles produce a more negative Doppler velocity.

2.2 Expectations of DDV and Z_{DR} in ice clouds

In Type I mixed-phase cloud regions, pristine oriented crystals grow at the expense of SLW drops. These SLW drops are very small, and therefore contribute very little to the radar signal. However, the pristine crystals have extreme aspect ratios and fall with their major axis aligned horizontally which produces a high Z_{DR} value. Hogan *et al.* (2003a) showed that elevated Z_{DR} can therefore act as a proxy for the presence of SLW. Since they are the only crystal population in the radar sampling volume, the H and V polarisation estimates of the Doppler velocity will be the same. Type I regions can therefore be identified by relatively high Z_{DR} and low DDV measurements. In Type II regions, these pristine oriented crystals are embedded amongst irregular polycrystals and aggregates (which have a Z_{DR} of approximately 0 dB). The magnitude of DDV depends on the relative contribution of the pristine oriented crystals to radar reflectivity, the shapes of the pristine oriented crystals and the aggregates or polycrystals, and the difference in fall speeds between the two crystal populations. DDV will typically be much higher when a mixture of crystal habits is present, and Z_{DR} will be greater than 0 dB as it contains contributions from highly aligned pristine crystals. In aggregate or polycrystal only regions, Z_{DR} will be small, as the particles are approximately spherical to the radar, and DDV should be low as they are all the same type. Regions consisting of irregular polycrystals and aggregates can therefore be identified by low Z_{DR} and low DDV measurements. A summary of expected DDV and Z_{DR} for each of these situations is given in table 2.1.

As the radar elevation angle increases, the vertically polarised wave becomes increasingly in the plane of the horizontally polarised wave, until at vertical Z_{DR} is always 0 dB as both polarisations are in the same plane. Z_{DR} can be computed using the Rayleigh Gans approximation. Figure 2.1 shows computed Z_{DR} for plates and

Table 2.1: Theoretical observations of DDV and Z_{DR} in polycrystals and aggregates-only regions, and Type I and II mixed-phase clouds.

	Agg/poly only	Type I	Type II
Z_{DR}	low	high	intermediate
DDV	low	low	high

columns similarly to figure 1.9, but at an elevation angle of 45°. Note that the maximum Z_{DR} value possible for plates is only approximately 3.5 dB (compared to 10 dB at 0° elevation), and for columns is approximately 1.8 dB. Full details of this calculation can be found in appendix B.

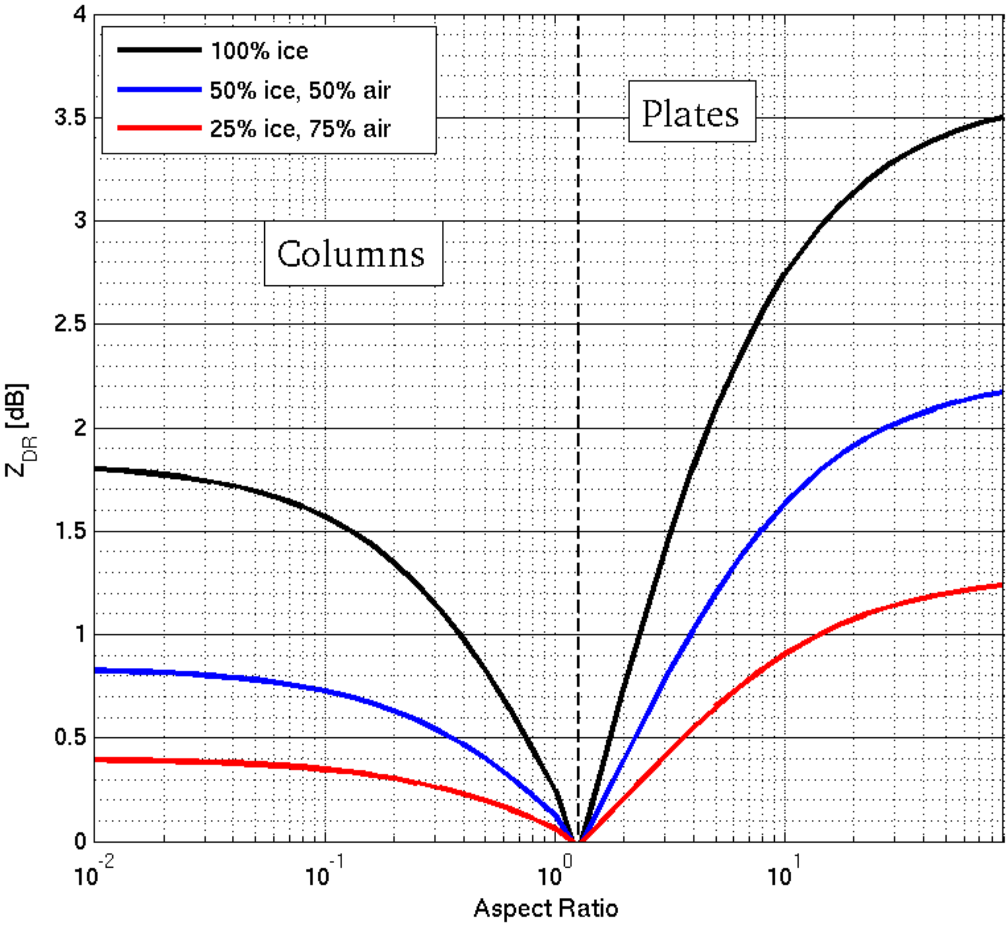

Figure 2.1 Differential reflectivity as a function of aspect ratio and particle density for plates and columns at an elevation angle of 45°. Particles are aligned horizontally. Columns are assumed to have a random azimuthal orientation.

2.3 Example case study: 11 August 2015

On the 11 August 2015, a front passed over the Southern U.K. which was sampled by the Copernicus radar. Z_{DR} and DDV were recorded with a 30 m range resolution, and a 30 second integration time; the specifications of this radar are shown in table

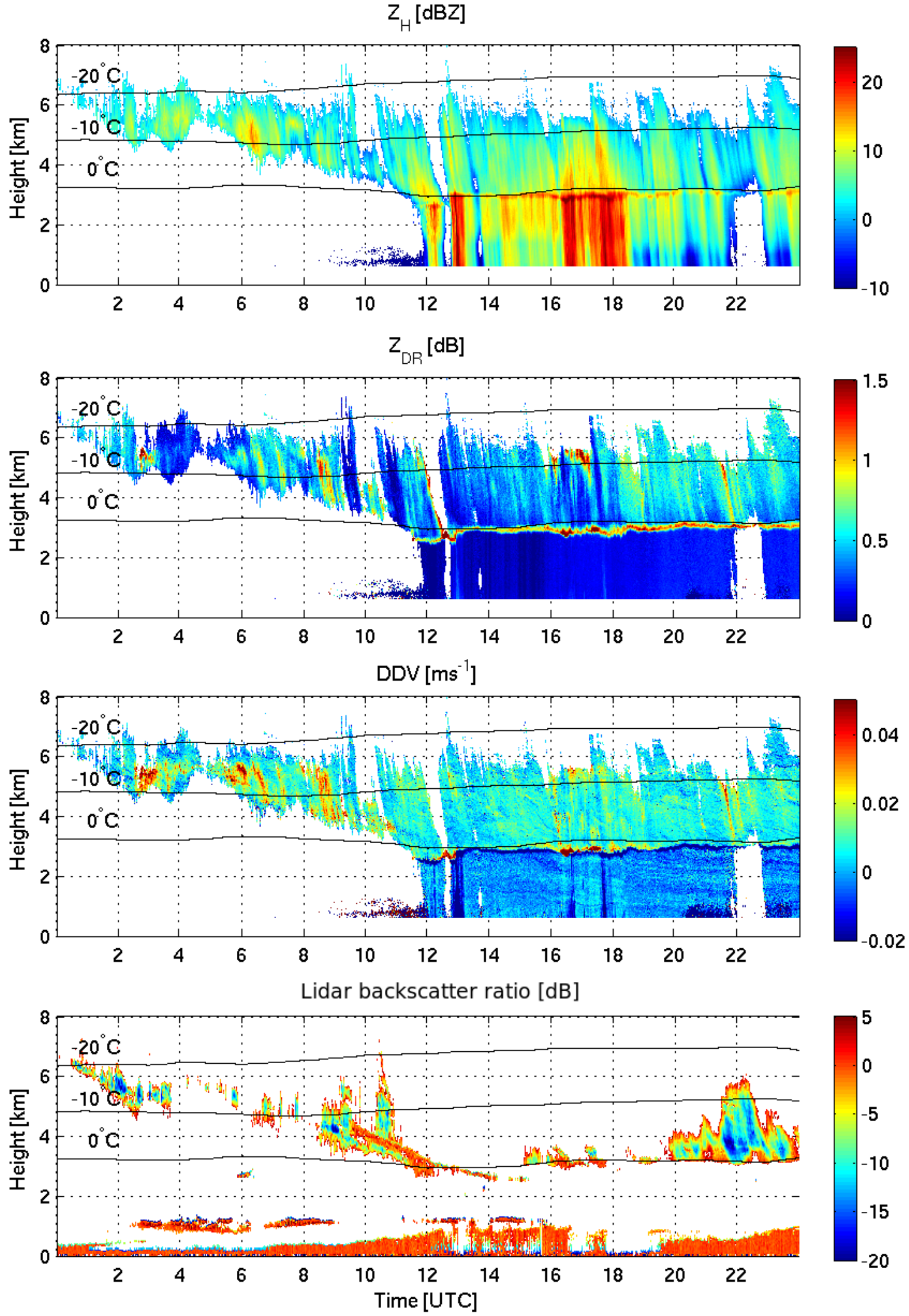

Figure 2.2 Observations of (a) Z, (b) Z_{DR}, (c) DDV and (d) lidar backscatter ratio from 11 August 2015. Only radar data with SNR > 10 dB is shown. Lidar backscatter ratio is shown at all points in which off-zenith backscatter was measured.

1.1. Full details of this instrument can be found in Illingworth *et al.* (2007). Rain rates were always less than 1 mm hr^{-1} for the duration of the front. Figure 2.2 shows measurements of Z_{DR} (a) and DDV (b) from this day. The melting layer can clearly be seen at approximately 2.5 km as region of enhanced Z, Z_{DR} and typically strongly negative DDV, the result of a complicated mixture of shapes, particle phases and fall speeds. In the rain, DDV is slightly negative (see section 1.3.4).

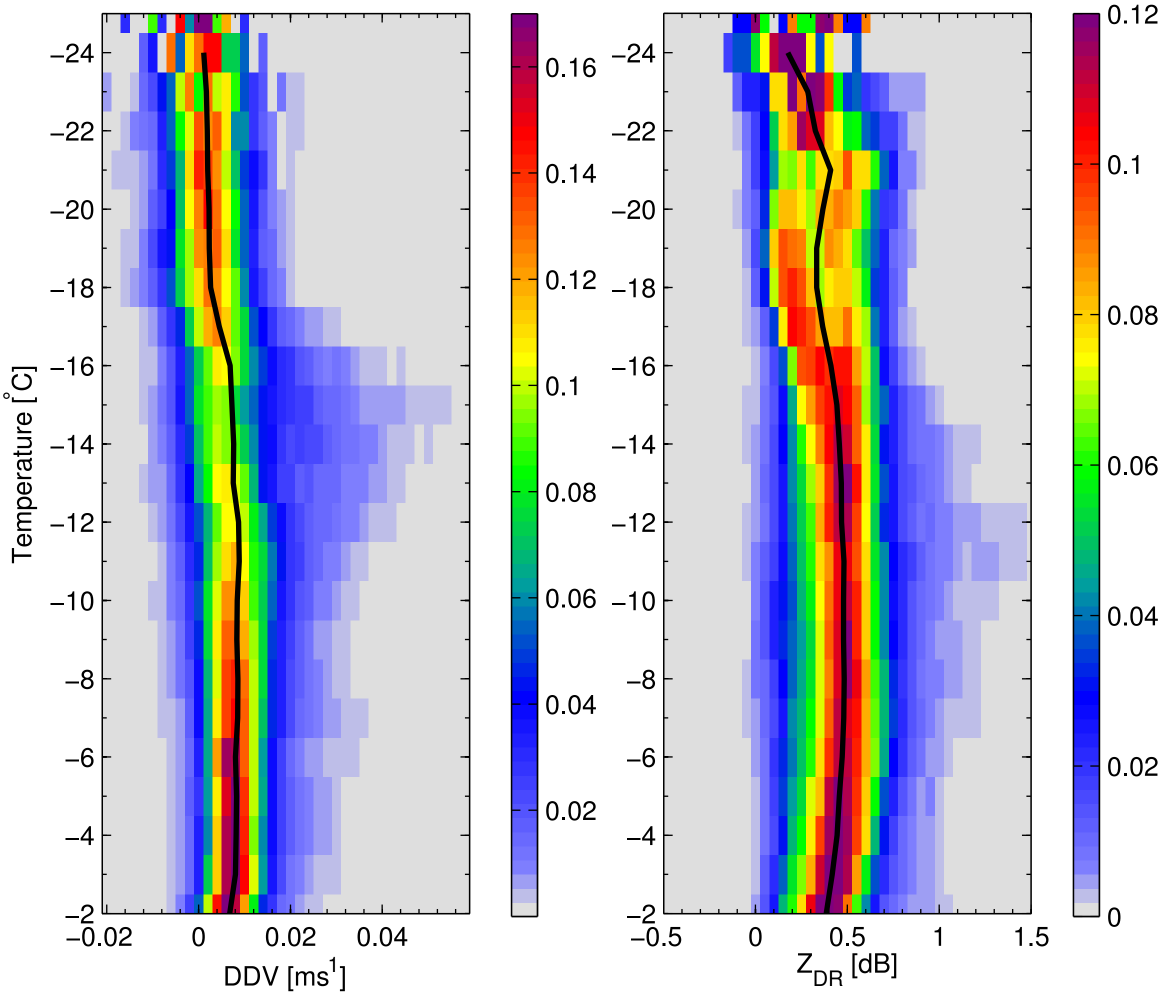

Figure 2.3 Normalised PDFs of Differential Doppler Velocity (left) and Z_{DR} (right), as functions of temperature for 11 August 2015. DDV is binned ever 0.002 ms^{-1}, Z_{DR} every 0.05 dB, and temperature every 2.5°C. Only data with SNR > 10 dB is shown. The probabilities sum to 1 for each temperature bin. Temperature was imported from the operational ECMWF model.

Some very interesting radar signatures can be seen in the ice cloud on this day. In particular, between 00:00 UTC and 10:00 UTC there are strong DDV and Z_{DR}

signatures at approximately 4—6 km in height. The interpretation of these high Z_{DR} as high-density plate-like crystals is supported by observations from a 1.5 μm Doppler lidar also installed at the Chilbolton Observatory. This instrument records profiles of backscatter and Doppler velocity for 36 m range gates and alternates between pointing at zenith and 4° off-zenith every 20 s. Oriented plate crystals can cause specular reflection; "mirror-like" reflections of the lidar beam (Platt, 1978). If plate crystals are present, then the backscatter at zenith will be much higher than that slightly off-zenith (Thomas *et al.*, 1990; Westbrook *et al.*, 2010). A useful parameter to identify specular reflection is the lidar backscatter ratio, defined as:

$$\text{Lidar Backscatter Ratio [dB]} = 10\log_{10}\left(\frac{\beta}{\beta^{z}}\right) \tag{2.1}$$

where β and β^{z} are the off-zenith and zenith pointing backscatters respectively. The presence of plate crystals can therefore be identified by negative backscatter ratios (i.e. $\beta^{z} \gg \beta$). Figure 2.2 (d) shows the lidar backscatter ratio calculated for 11 August 2015. Lidar is typically only able to penetrate the first 1—2 km of an ice cloud, but is strongly attenuated by liquid water. The near zero backscatter ratios between 00:00 and 10:00 UTC in the lowest 1 km in height are likely the result of backscatter from boundary layer aerosols, which are typically quasi-spherical and backscatter equally in both pointing directions. Unfortunately, much of the ice cloud containing interesting DDV and Z_{DR} signatures appears to be obscured by a thin layer of liquid water cloud at approximately 1 km. However, backscatter ratios down to -15 dB are seen between 01:00 and 04:00 UTC, co-located with enhanced Z_{DR}. Even more negative backscatter ratios (as low as -20 dB) are observed between 22:00 — 23:00 UTC, where a gap in the low cloud allowed the lidar to directly sample the ice crystals. This supports the interpretation that elevated Z_{DR} regions are the result of pristine plate-like crystals. Co-located DDV measurements are typically greater than 0.01 ms^{-1}, suggesting that the observed plates are present among other aggregates or polycrystals.

For further insight into the microphysical processes occurring in this frontal system, figure 2.3 shows normalised probability distributions (PDFs) of DDV (left) and Z_{DR} (right) as a function of temperature for this day. These PDFs reveal interesting

DDV and Z_{DR} signatures. Between -24 and -18°C, the median DDV is approximately constant at 0.002 ms^{-1}. The median Z_{DR} value is variable, exhibiting a peak of approximately 0.5 dB at approximately -21°C. There appears to be bi-modal Z_{DR} at these temperatures, which could be the sampling of different pristine oriented crystals with different "intrinsic" Z_{DR}. At temperatures warmer than -16°C, there is increased likelihood of elevated DDV and Z_{DR}. The maximum DDV sampled was over 0.04 ms^{-1} at -15°C, and the maximum Z_{DR} sampled was 1.5 dB at approximately -12°C. Broadly, this suggests the presence of Type II mixed-phase clouds at these temperatures. At temperatures warmer than -12°C, the median DDV remains approximately constant while Z_{DR} decreases slightly, suggesting aggregation is occurring The probability of observing elevated DDV and Z_{DR} signatures (compared to colder than 18°C) remains high, even up to -2°C.

2.4 10 weeks of continuous Z_{DR} and DDV measurements

In this section, a statistical analysis of mixed-phase clouds from 10 weeks of continuous observations is presented. In order to be included in the analysis, the data was subjected to the following criteria: (a) the signal-to-noise ratio must be larger than 10 dB, (b) the temperature of the observation must be colder than -2°C and (c) the surface rain rates (from a rain gauge also located at the Chilbolton Observatory) must be less than 1 mm hr^{-1}. The reason for a rain rate threshold is that differential attenuation was often observed during precipitating frontal systems, caused by oblate drops extinguishing more of the H than the V polarised wave. This was significant due to the radar's 8.6 mm wavelength, resulting in Z_{DR} estimates being biased low. In total, there were approximately 1.4 million data points that met these requirements. Probability distributions of DDV (which is unaffected by the effects of differential attenuation) when the rain rate was greater than 1 mm hr^{-1} show very similar behaviour to when rain rate was less than 1 mm hr^{-1}, suggesting that the remaining data is broadly representative of the microphysics in both cases.

Z_{DR} was calibrated using measurements of drizzle during the campaign; drizzle

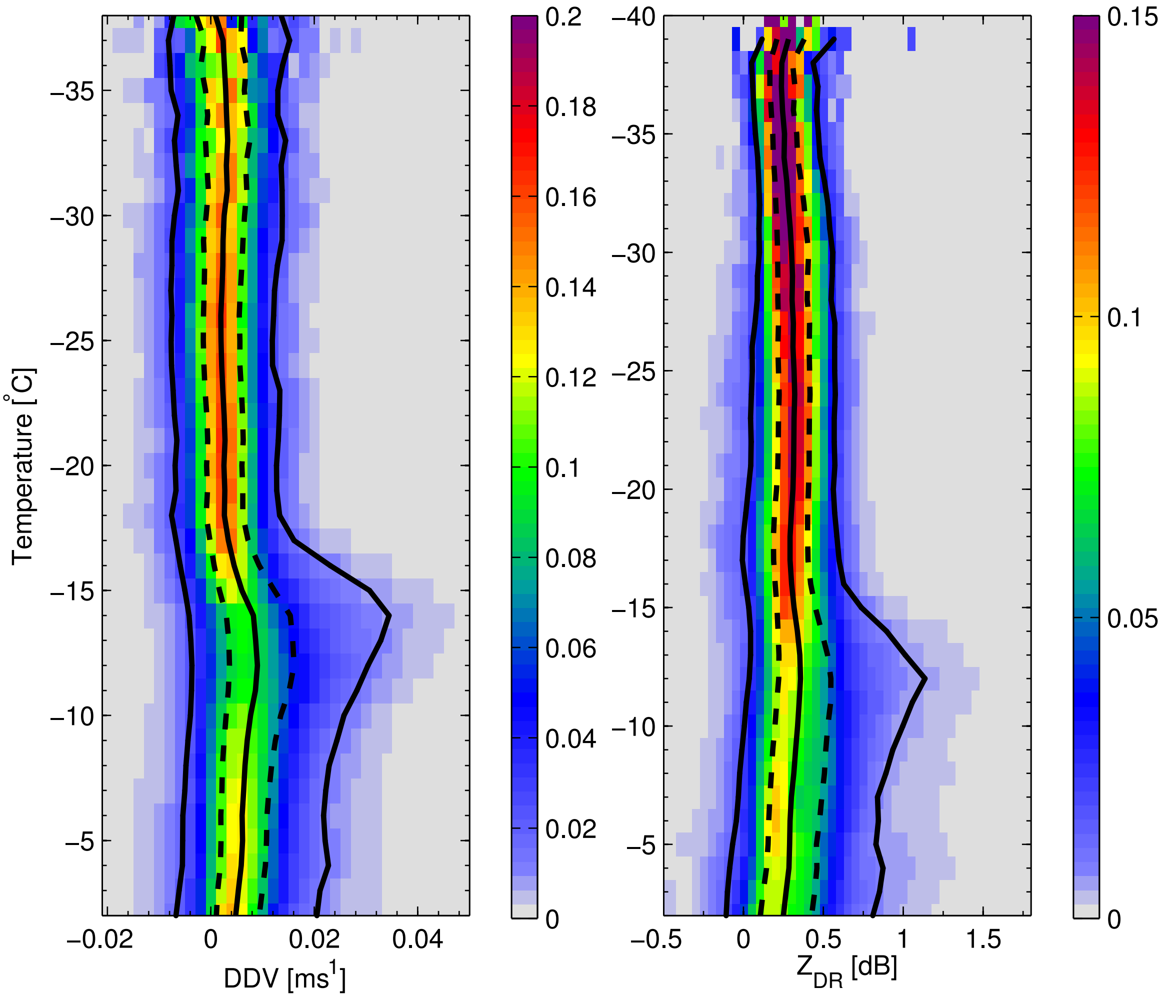

Figure 2.4 Normalised PDFs of Differential Doppler Velocity (left) and Z_{DR} (right), as functions of temperature, for a total of 1.4 million data points. DDV is binned ever 0.002 ms^{-1}, Z_{DR} every 0.05 dB, and temperature every 2.5°C. The sum of the probabilities is one for each temperature bin. Temperatures are imported from the ECMWF operational model. Also shown are the median (solid line), upper and lower quartiles (dashed lines) and 95$^{\text{th}}$ percentiles. Only data with SNR > 10 dB is shown. Note the different temperature scale to figure 2.3.

drops are known to be spherical and hence have a Z_{DR} of 0 dB. It was then checked again once the radar had been returned to point vertically, where Z_{DR} should always be 0 dB. It was found that typically Z_{DR} was -0.7 dB in both of these cases, with a slight temperature dependence. The reason for this temperature dependence is unclear, but it is estimated that the addition of a 0.7 dB offset means that Z_{DR} for the data shown in this chapter is calibrated to within 0.1 dB.

Figure 2.4 shows normalised probability distributions of DDV (left) and Z_{DR} (right) with temperature for all of the data collected during the campaign that passed the aforementioned thresholds. Overplotted are the median, upper and lower quartile ranges, and 95$^{\text{th}}$ percentiles of the data. Below -33°C, the median DDV is very slightly positive (0.0025 ms^{-1}), while Z_{DR} is approximately 0.25 dB. Between -33 and -20°C, DDV remains constant at approximately 0.0025 ms^{-1}, whilst there is a slight increase in the median Z_{DR} to approximately 0.3 dB. This is consistent with the presence of a mixture of columnar or plate-like polycrystals and aggregates thereof, which are known to be the dominant crystal habit at these temperatures (Heymsfield and Knollenberg, 1972; Heymsfield and Iaquinta, 2000; Bailey and Hallett, 2009). Similar to the above case study, between temperatures of -20 and -10°C, some interesting DDV and Z_{DR} signatures are observed. The median Z_{DR} remains approximately constant, however the probability of observing higher Z_{DR} significantly increases, as indicated by the 95$^{\text{th}}$ percentile line. The median DDV in this temperature range increases with temperature to a peak of approximately 0.01 ms^{-1} at -13°C, with a large increase in the probability of observing higher values. There is a clear peak in the DDV 95$^{\text{th}}$ percentile to approximately 0.03 ms^{-1} at -14°C. The overall probability of measuring DDV greater than 0.01 ms^{-1} at any temperature is 29%; 96% of these observations occur warmer than -20°C. Likewise, the 95$^{\text{th}}$ percentile of Z_{DR} increases to approximately 1 dB, but at a slightly warmer temperature than DDV, at -12°C. The probability of observing Z_{DR} greater than 0.8 dB at any temperature is only 5%, but nearly all (99%) of these observations are at temperatures warmer than -20°C. These measurements indicate the existence of plate and dendrite crystals which are known to be the dominant habit between -10 and -20°C (Bailey and Hallett, 2009), and interestingly is at approximately the maximum theoretical mass growth rate of pristine crystals (see section 1.1.5.1). The fact that they correspond to increased DDV is indicative of embedded pristine crystal growth (Type II mixed-phase clouds). Warmer than -10°C, there is a gradual decrease in the median observations of DDV and Z_{DR}; this is indicative of aggregation as fall speed differences and average crystal density is decreasing. Interestingly, there is a small increased chance of observing higher DDV and Z_{DR} at approximately -4°C; it is this temperature that the transition from columnar to plate-like crystal growth occurs and approximately at the peak efficiency of the Hallet-Mossop process (which is approximately -5°C, Hallett and Mossop, 1974). There is an increased chance of observing elevated DDV and Z_{DR}, which suggests that Type II regions are more frequent at warmer temperatures. However, it is clear from these statistics that Z_{DR} measurements are predominantly low. In fact, 79% of the time, Z_{DR} measurements are smaller than 0.5 dB, suggesting that irregular ice particles are responsible for the majority of the radar backscatter.

It is interesting to note that the DDV peak occurs at a colder temperature than peak Z_{DR}. As mentioned above, DDV is a function of the fall speed differences, and the relative concentrations and shapes of the ice particles in the sampling volume. One possible explanation for this behaviour is that newly developing pristine crystals initially have a small mass, therefore contribute little to the radar signal (and produce a small Z_{DR}). They will also initially have a small terminal velocity; this means that their fall speed difference with the surrounding particles is at a maximum. Since DDV is sensitive to this difference in fall speeds, it could be that these crystals are detected by DDV measurements before the crystals weigh the Z_{DR} measurements significantly. Although care must be taken when attempting to interpret composites of many days with potentially differing microphysics, the same behaviour is observed in the case study in figure 2.3, suggesting that this feature is more general, and could contain characteristic microphysical information of ice crystal growth in Type II regions. This is of interest for future work.

2.5 Frequency of occurrence of mixed-phase clouds

Pristine oriented crystals produce high Z_{DR} and indicate the presence of SLW (Hogan *et al.*, 2003a). The combination of Z_{DR} and DDV can therefore be used to distinguish whether these crystals are occurring alone or amongst other crystal habits, and therefore to identify either Type I or Type II mixed-phase clouds. Thus the frequency of occurrence of each of these cloud types that occurred during the 10 weeks of observations can be estimated.

In this section, clouds will be categorized as being (a) Type I mixed-phase, (b)

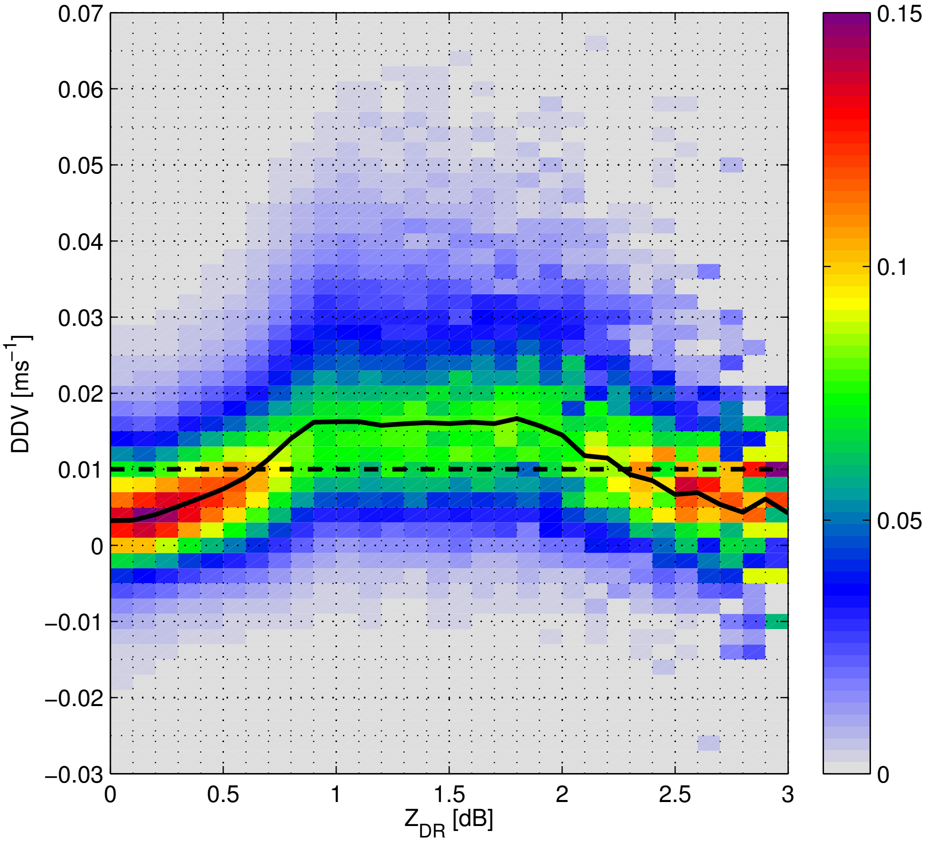

Figure 2.5 Normalised PDF of DDV and Z_{DR}, such that the sum of the probabilities is 1 for each Z_{DR} bin. The median DDV per Z_{DR} bin is shown (solid line). DDV = 0.01 ms^{-1} is used to categorize cloud type (dashed line).

Type II mixed-phase or (c) irregular polycrystals/aggregates, based on the observed DDV and Z_{DR} measurement for each pixel. Figure 2.5 shows a normalised PDF of DDV vs Z_{DR}, such that the sum of probabilities is 1 for each Z_{DR} bin. There is a very clear pattern in the distribution; for both low and high Z_{DR} (corresponding to polycrystals/aggregates only and pristine oriented crystals only), DDV is low as there is only one crystal type. Therefore, Type II clouds can be identified readily as pixels with DDV above a certain value. Figure 2.5 can be used to inform a threshold for which to classify each cloud type. A DDV threshold of 0.01 ms^{-1} is chosen, which is above the upper quartile of DDV for polycrystal dominated regions colder than -20°C. Any pixel with DDV larger than 0.01 ms^{-1} is defined as a Type II mixed-phase cloud. Pixels with Z_{DR} greater than 1 dB and DDV less than 0.01 ms^{-1} are categorised as

Type I clouds. Clouds containing only polycrystals or aggregates are identified as pixels with DDV greater than 0.01 ms^{-1} and Z_{DR} smaller than 1 dB. Occurrences of Z_{DR} greater than 1 dB and DDV smaller than 0.01 ms^{-1} are rare (approximately 1%). The relative occurrences of aggregates/polycrystals and Type I and II mixed-phase cloud are relatively insensitive to these threshold choices.

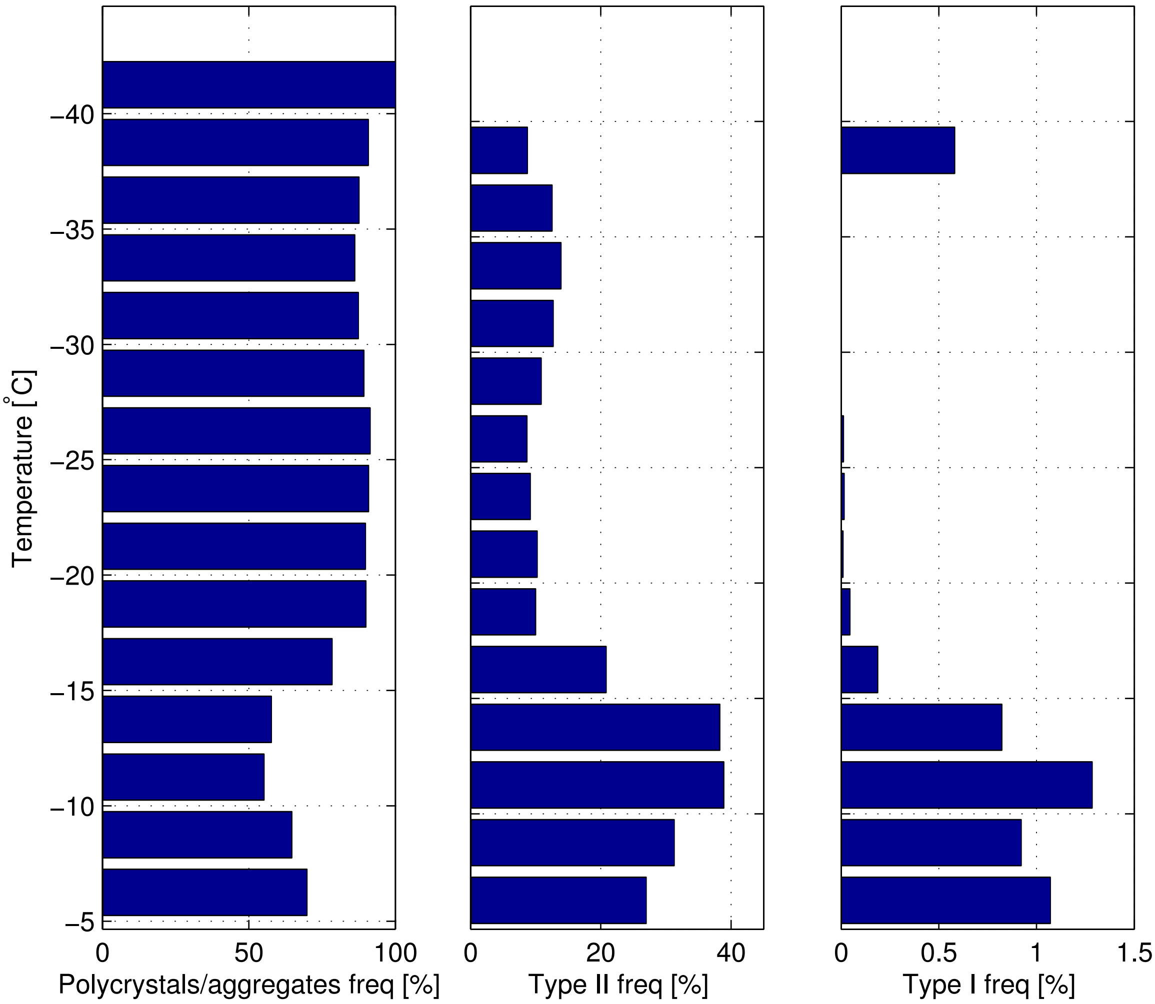

Figure 2.6 Frequency of occurrence of polycrystals and aggregates (left), Type II mixed-phase clouds (middle) and Type I mixed-phase clouds (right) as a function of temperature, binned every 2.5°C.

Overall, using the categorisation above, it is estimated that 72% of all of the ice cloud pixels observed during the 10 week period were polycrystals or aggregates only. The overall frequency of occurrence of Type II mixed-phase clouds is estimated to be 27%, and the fraction of pixels identified as Type I is small; only 1%. This could be, in part, due to the definition of frequency of occurrence used. Mid-level cloud types (such as altocumulus) that would be classified as Type I mixed-phase clouds do occur relatively frequently, but when they do occur they are much shallower compared to frontal systems. It is easy for pixels from longer duration, deeper frontal systems to dwarf the number of those from this cloud type.

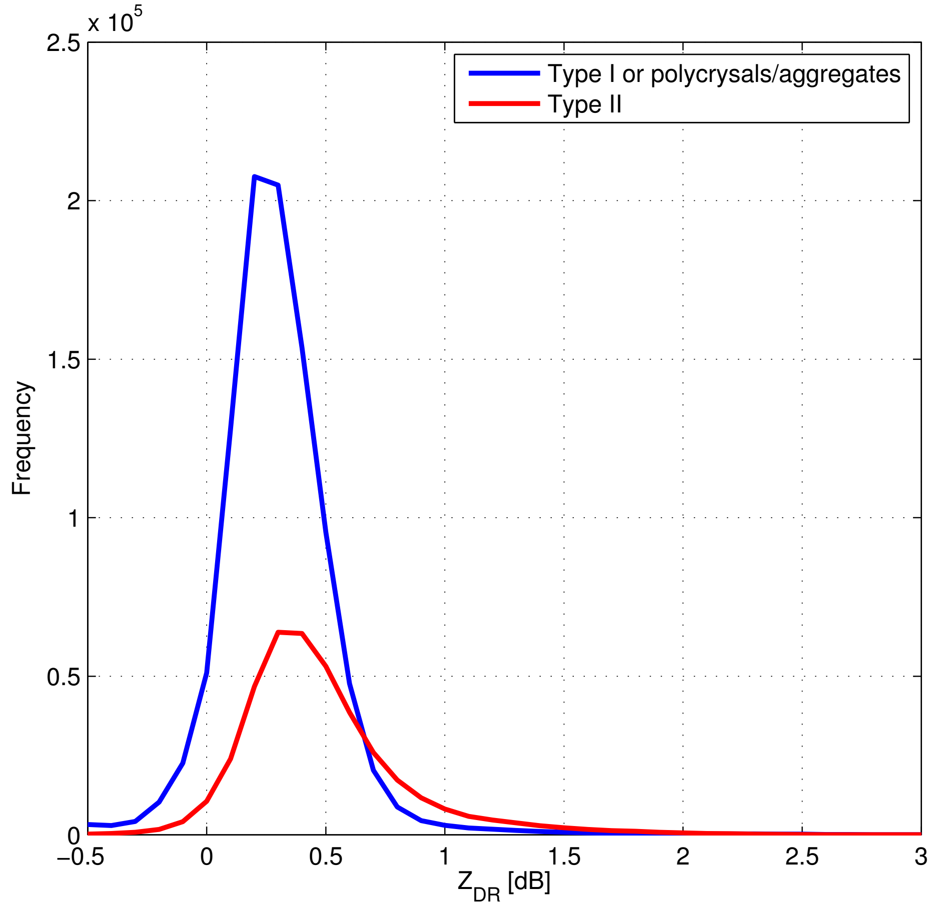

Figure 2.7 Frequency distribution of Z_{DR} for polycrystals and aggregates (blue) and Type II mixed-phase clouds (red). Observations of Z_{DR} alone are not able to distinguish between these cloud types.

Figure 2.6 breaks down the frequency of occurrence with temperature for polycrystals and aggregates (left), Type II mixed-phase clouds (middle) and Type I mixed-phase clouds (right). It can be seen clearly that for every temperature bin, polycrystals and aggregates dominate. At temperatures colder than -17.5°C, polycrystals or aggregates are observed over 85% of the time, and all pixels observed at -40°C were categorised as this type. Even at the temperature of their minimum relative frequency in the -12.5 to -10°C bin, 60% of all pixels are categorised as this type. These statistics appear consistent with the observation of Korolev *et al.* (2000) that 84% of ice particles larger than 125 μm observed in-situ have an irregular shape. However Stoelinga *et al.* (2007) suggest that this could be an overestimate due to the definition of an "irregular" crystal shape used in their study. Figure 2.6 (right) shows that, although few in number, pixels that are identified as Type I clouds nearly all occur warmer than -17.5°C. The exception to this is at approximately -40°C, which presumably is the identification of Type I regions at cloud top. Finally, figure 2.6 (middle) shows frequency of occurrence of Type II mixed-phase clouds as a function of temperature. The results suggest that these cloud types exist down to -40°C; the embedded pristine crystals at these colder temperatures would more likely be columnar. Importantly, there appears to be frequent occurrences of embedded mixed-phase clouds between -15 and -5°C. Almost 40% of the pixels between -15 and -10°C are categorised as Type II mixed-phase clouds, decreasing to 25% at -5°C. These statistics suggest Type II mixed-phase clouds are a significant occurrence in the atmosphere.

The frequencies of occurrence estimated here are not based on direct measurements of mixed-phase conditions, rather they are inferred by elevated Z_{DR} measurements (produced by pristine oriented crystals) which have been shown to be associated with the presence of SLW (Hogan *et al.*, 2003a). Using Z_{DR} to infer the presence of SLW could lead to overestimates of the frequency of occurrence of both mixed-phase types. This is because pristine oriented crystals sediment from the region of SLW producing them, and therefore will likely produce elevated Z_{DR} measurements over a greater depth than the SLW layer itself. Therefore, these frequencies of occurrence may be more appropriately thought of as clouds that have been *influenced* by SLW, rather than those pixels that necessarily contain SLW. The low fraction of occurrence if Type I clouds does not mean they are a rare occurrence, only that pixels that contain only pristine oriented crystals make a small contribution to the total number of observed pixels. This does not change the important conclusion that pristine oriented crystals are frequently embedded in ice clouds.

Figure 2.7 shows the frequency distribution of Z_{DR} for polycrystals and aggregates (blue) and Type II mixed-phase clouds (red). Clearly, many more pixels are identified as polycrystals and aggregates, but the frequency distributions have a similar shape and span a similar range of Z_{DR}. Importantly this means that Z_{DR} alone is not sufficient to identify the occurrence of mixed-phase clouds, since many Type II clouds have similar Z_{DR} to ice-only clouds.

It would be interesting to apply a similar analysis using a 3 GHz radar (where attenuation is negligible) to fully investigate whether there are any microphysical differences in the normalised PDFs of Z_{DR} and DDV between raining and non-raining cases. Also, it would be interesting to use a radar with greater sensitivity, which may better detect the presence of small particles. The mostly likely result of this would be to increase the detection of Type I mixed-phase clouds, which typically produce much lower Z.

2.6 Summary

Statistics of Z_{DR} and DDV were presented from 10 weeks of data collected during July - September 2015, with the aim of helping to address the deficiency in mixed-phase clouds observations. In total, 1.4 million 30 m 10 s pixels were used in the analysis. The statistical polarimetric characteristics of ice clouds have not previously been characterised, nor measurements of DDV been used in this way. Interesting signatures of DDV and Z_{DR} are observed, which can be interpreted microphysically as the result of single or multiple crystal habits occurring at different temperatures. Using DDV and Z_{DR} thresholds, it is possible to estimate the frequency of occurrence of irregular ice particles, and Type I and II mixed-phase clouds, during the 10 weeks of continuous observations. It is estimated that 72% of all pixels contained irregular polycrystals or aggregates only, 27% were Type II mixed-phase clouds, and Type I mixed-phase clouds 1% (although this may be in part due to the choice of definition of a Type I mixed-phase cloud). At warmer temperatures (e.g. -15 and -10°C), the fraction of Type II mixed-phase clouds was shown to be almost 40%. Their significant frequency of occurrence motivates further investigation of this cloud type. This will be the subject of chapter 4.

It was shown that DDV is a useful measurement for categorizing cloud types. However, DDV is a function of three unknown parameters: the relative contribution pristine crystals make to radar reflectivity, the shapes of each of the crystals in the sampling volume and the difference in fall speeds between them. Using only two radar measurements (DDV and Z_{DR}), it is not possible for these parameters to be retrieved separately. The co-polar correlation coefficient, ρ_{hv}, which is also sensitive to shape diversity, was not successfully measured during the 10 week experiment. This is unfortunate because, like Z_{DR}, it only depends on two unknown parameters: the relative contributions of pristine crystal types to the radar reflectivity and their shape. Combinations of ρ_{hv} and Z_{DR} measurements therefore have the potential to be more useful for probing the microphysics of these Type II mixed-phased clouds. This is the focus of chapter 4. However, in order to fully exploit ρ_{hv} quantitatively, the accuracy of ρ_{hv} measurements must first be quantified. This forms the basis of chapter 3.

Chapter 3

Defining a new variable: $L = -\log_{10}(1 - \rho_{hv})$

3.1 Motivation

The co-polar correlation coefficient, ρ_{hv}, between horizontal (H) and vertical (V) polarisation radar signals is a measure of the variety of hydrometeor shapes in a pulse volume. ρ_{hv} dictates both the quality of dual polarisation measurements (Bringi and Chandrasekar, 2001) and their weighting in hydrometeor classification schemes (Park *et al.*, 2009). At present, quantitative use of ρ_{hv} is hampered by lack of rigorous confidence intervals accompanying the ρ_{hv} estimates. Error estimates are available adopting an empirical approach (Illingworth and Caylor, 1991) or a linear perturbation technique (Liu *et al.*, 1994; Torlaschi and Gingras, 2003), but both methods implicitly assume a Gaussian probability distribution for the ρ_{hv} samples. In this chapter, it will be shown that the distribution of ρ_{hv} samples is in fact non-Gaussian and highly negatively skewed. This work has been published in the Journal of Applied Meteorology and Climatology (Keat *et al.*, 2016).

Practically, ρ_{hv} is estimated by correlating successive power or complex (I and Q) measurements. Examples of power time-series in (a) drizzle and (b) heavier rainfall from CAMRa are shown in figure 3.1. The observed fluctuating signals are caused by the superposition of the backscattered waves from each drop in the sample volume; the rate of fluctuation is determined by the Doppler spectral width. For drizzle, since the drops are spherical, Z_{DR} is equal to 0 dB, and the H and V signals are almost perfectly correlated: ρ_{hv} is 0.995. For heavier rainfall, a systematically lower V power is received (Z_{DR} is 1.1 dB), and the signals are visibly less correlated (ρ_{hv} is 0.987), due to the broader axis ratio distributions in the sample volume.

These estimates of ρ_{hv} are derived from a finite number of reshufflings, and therefore there is some uncertainty in them. In what follows, this uncertainty will be quantified.

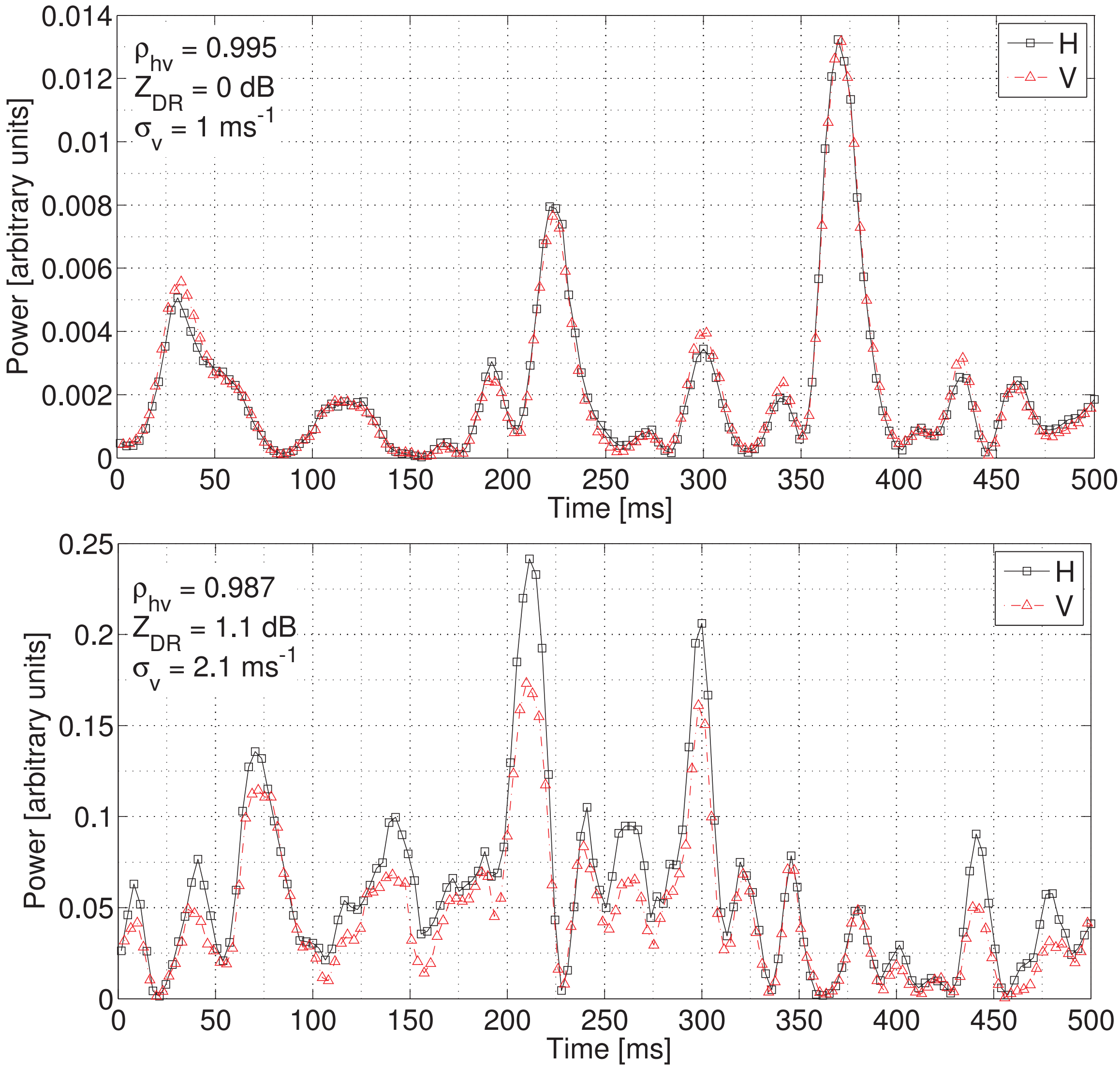

Figure 3.1 Example time-series (0.5 s) for single 75 m gates from 1.5° elevation dwells in (*a*) drizzle ($Z_{DR} = 0$ dB) at 1203 UTC on 6 February 2014, and (*b*) heavier rainfall ($Z_{DR} = 1.1$ dB) at 1706 UTC on 31 January 2014. For both examples, SNR > 40 dB. For drizzle, the H and V echo time-series vary in unison as the drops are all spherical. In heavier rainfall, the broader axis ratio distribution causes the H and V time-series to be less correlated. The rate of fluctuation of the signals is determined by the Doppler spectral width.

3.2 Theoretical error in estimated correlation of time-series

Figure 3.2a shows the distribution of estimates of the correlation coefficient, $\hat{\rho_{hv}}$ (calculated from a finite length time-series), as distinct from the "true" co-polar correlation coefficient, $\overline{\rho_{hv}}$ (that would be measured for a time-series of infinite length). The data was collected during a 1.5° elevation dwell in drizzle (Z_{DR} greater than 0.1 dB), with very high SNR (greater than 40 dB) on 6 February 2014. Each $\hat{\rho_{hv}}$ is calculated from 64 H and V pulse pairs (0.21s dwell) from 75 m range gates where σ_v is 1.1 ± 0.1 ms^{-1}. The distribution of $\hat{\rho_{hv}}$ has a peak that is close to $\overline{\rho_{hv}}$ (which is smaller than 1, see section 3.4.4), but exhibits a very long tail at lower $\hat{\rho_{hv}}$, while there are no data with $\hat{\rho_{hv}}$ greater than 1. Clearly, this distribution is not Gaussian and the negative skewness will negatively bias the mean of many $\hat{\rho_{hv}}$ samples compared to the true value of ρ_{hv}.

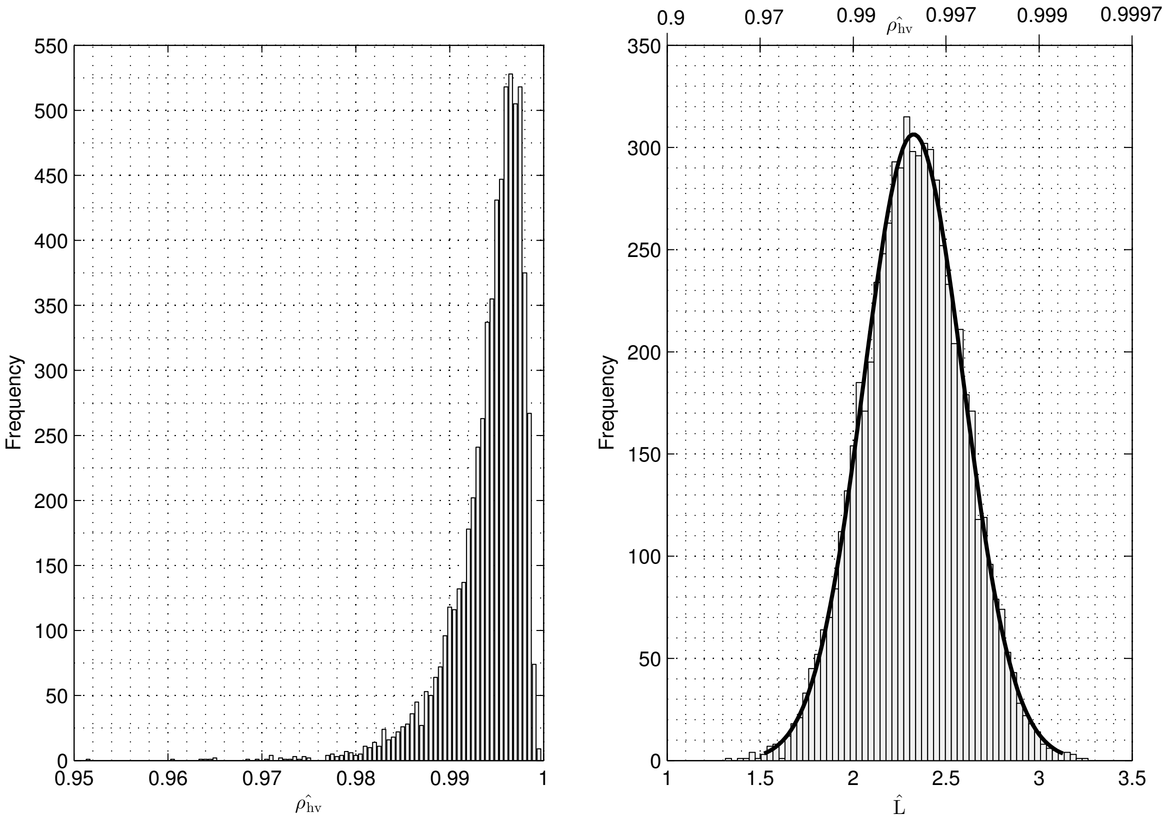

Figure 3.2 The frequency distribution of (a) $\hat{\rho_{hv}}$ calculated from 1159 time-series (0.21 s, 75 m gates) in drizzle ($Z_{DR} < 0.1$ dB) and (b) $\hat{L} = -\log_{10}(1\text{-}\hat{\rho_{hv}})$. The data was collected at 1203 UTC on 6 February 2014 during a 1.5° elevation dwell and has very high SNR (> 40 dB). σ_v for these data is 1±0.1 ms^{-1}. Overplotted on $\hat{L}$ is a Gaussian curve with same mean and standard deviation as the measured distribution.

Fisher (1915) states that sample correlation coefficients ($\hat{\rho}$) of a "true" correlation coefficient ($\overline{\rho}$) calculated from a finite number of Gaussian random variables are skewed for $\overline{\rho}$ not equal to 0. However, the variable:

$$\hat{F} = \frac{1}{2} \ln \left(\frac{1+\hat{\rho}}{1-\hat{\rho}} \right) \tag{3.1}$$

is Gaussian, with a mean of:

$$\bar{F} = \frac{1}{2} \ln \left(\frac{1+\overline{\rho}}{1-\overline{\rho}} \right) \tag{3.2}$$

and standard error of:

$$\sigma_F = \frac{1}{\sqrt{N-3}} \tag{3.3}$$

where N is the number of independent samples used to calculate $\hat{\rho}$.

This is directly applicable to estimates of the radar co-polar correlation coefficient, by realising that the I and Q samples that are used to estimate ρ_{hv} are Gaussian random variables (Doviak and Zrnic, 2006). Noting that $\hat{\rho_{hv}}$ in meteorological targets is always close to unity so that fractional changes in $(1 - \hat{\rho_{hv}})$ are always much greater than $(1 + \hat{\rho_{hv}})$, equation 3.1 can be written as:

$$\hat{F} \approx \frac{1}{2} \ln 2 - \frac{\ln 10}{2} \log_{10}(1 - \hat{\rho_{hv}}) \tag{3.4}$$

Since $\hat{F}$ is normally distributed, the quantity:

$$\hat{L} = -\log_{10}(1 - \hat{\rho_{hv}}) \tag{3.5}$$

is also normally distributed, with a mean:

$$\bar{L} = -\log_{10}(1 - \overline{\rho_{hv}}) \tag{3.6}$$

and standard deviation of:

$$\sigma_L = \frac{2}{\ln 10} \times \frac{1}{\sqrt{N_{IQ} - 3}} \tag{3.7}$$

for $N_{IQ} \gg 3$, where N_{IQ} is the number of independent I and Q samples used to calculate $\hat{\rho_{hv}}$. Despite having similar characteristics, L is preferred over the use of F as it has the convenient property that ρ_{hv} values of 0.9, 0.99 and 0.999 correspond to L values of 1, 2 and 3 respectively and therefore is more intuitive. Illingworth and Caylor (1991) plotted their $\hat{\rho_{hv}}$ data as $\log_{10}(1 - \hat{\rho_{hv}})$ and their histograms also appear Gaussian in shape, although they did not recognise the significance of this. Figure 3.2b illustrates the effect of the transform $\hat{L} = -\log_{10}(1 - \hat{\rho_{hv}})$ on the distribution in figure 3.2a. The histogram is now symmetrical, and bell shaped. A Gaussian curve with an equal mean and standard deviation to the $\hat{L}$ PDF is overplotted and is an excellent fit to the data, showing that the distributions are indeed Gaussian (and Quantile - Quantile plots, not shown here for brevity, confirm this).

The number of independent I and Q samples, N_{IQ}, can be estimated using the autocorrelation function for I and Q samples given by Doviak and Zrnic (2006):

$$R_{IQ}(nT_s) = \exp\left[-8\left(\frac{\pi\sigma_v nT_s}{\lambda}\right)^2\right] \tag{3.8}$$

where T_s is the time spacing between pulses of the same polarisation and nT_s is the total time lag. It was shown by Papoulis (1965):

$$\frac{1}{N_I} = \sum_{(n=-N-1)}^{N-1} \frac{N - |n|}{N^2} R(nT_s) \tag{3.9}$$

where N is the the number of samples and N_I is the number of independent samples. By substituting equation 3.8 into equation 3.9, the time to independence for I and Q samples for large N_{IQ} can be shown to be:

$$\tau_{IQ} = \frac{\lambda}{2\sqrt{2\pi}\sigma_v} \tag{3.10}$$

where λ is the radar wavelength and σ_v is the Doppler spectral width. This is a factor of $\sqrt{2}$ smaller than the more often used time to independence for reflectivity samples. The number of independent I and Q pulses per ρ_{hv} sample can therefore be estimated by:

$$N_{IQ} = \frac{T_{dwell}}{\tau_{IQ}} = \frac{2\sqrt{2\pi}\sigma_v T_{dwell}}{\lambda} \tag{3.11}$$

where T_{dwell} is the dwell time.

The result (equation 3.7) is significant as it shows that a confidence interval for any measurement of ρ_{hv} can be calculated solely in terms of the number of independent I and Q samples used to estimate it, which in turn can be readily estimated using the observed Doppler spectral width and equation 3.11. Furthermore, when multiple samples of $\hat{L}$ are averaged, no bias is introduced to estimates of $\hat{\rho_{hv}}$ because of the non-linear transform. This point is expanded in section 3.3.

To estimate confidence intervals for measurements of $\hat{\rho_{hv}}$, one must:

- Apply the transform $\hat{L} = -\log_{10}(1 - \hat{\rho_{hv}})$
- Calculate the standard deviation of $\hat{L}$ using equation 3.7.
- Apply the inverse transform $1 - 10^{-(\hat{L} \pm \sigma_L)}$ to obtain upper and lower confidence intervals (where σ_L will contain the true value 68% of the time and $2\sigma_L$ 98%).

More conveniently, one can simply transform $\hat{\rho_{hv}}$ data to $\hat{L}$ and use this for any subsequent analysis, with confidence intervals of $\hat{L} \pm \sigma_L$. This is the approach that will be followed in the rest of this thesis. Although most of the data in this thesis has a high signal-to-noise ratio, the theory above should also be valid for weak SNR data, providing that noise introduced is also Gaussian in the I and Q samples.

This theoretical prediction was tested by comparing estimates of σ_L using data collected in homogeneous drizzle (Z_{DR} smaller than 0.1 dB) with very good signal-to-noise (SNR greater than 40 dB). In drizzle, $\overline{L}$ is constant since the drops are spherical, and therefore any variation σ_L is due to the finite N_{IQ}. Pulse-to-pulse H and V powers were recorded, and time series of various lengths between 0.2—30 s were constructed from these data and used to compute the corresponding N_{IQ} and $\hat{L}$ values. Data was

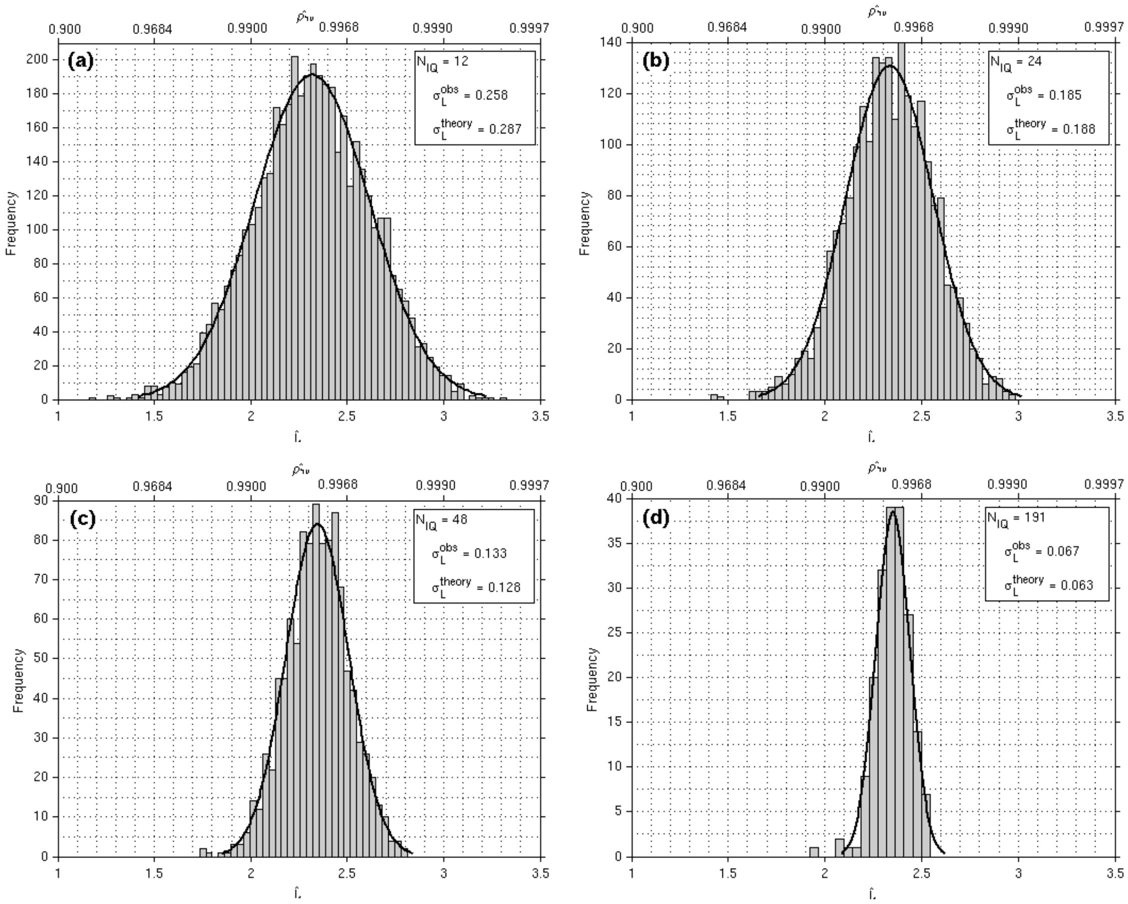

Figure 3.3 Distributions of $\hat{L}$ calculated from (a) N_{IQ} = 12, (b) N_{IQ} = 24, (c) N_{IQ} = 48 and (d) N_{IQ} = 191 in drizzle for Doppler spectral width 1 ± 0.1 ms^{-1}. The observed standard deviation of L (σ_L^{obs}) decreases as N_{IQ} decreases as predicted by theory (σ_L^{theory}). Overplotted on each $\hat{L}$ distribution is a Gaussian curve with an equal mean and standard deviation to the observed distributions.

binned by N_{IQ}, and the standard deviation, σ_L, were computed for each bin. Figure 3.3 shows the PDFs of $\hat{L}$ calculated from N_{IQ} values of (a) 12, (b) 24, (c) 48 and (d) 191 from data with a spectral width of 1.1 ± 0.1 ms^{-1}. Overplotted Gaussian curves with the same mean and standard deviations of the PDF further demonstrate that the distributions of $\hat{L}$ are Gaussian. The same method was applied to data with different spectral widths of 0.92, 0.99, 1.06, 1.13, 1.2 and 1.27 ± 0.035 ms^{-1}. The observed PDF widths are in excellent agreement with the predicted widths. Figure 3.4 shows how σ_L decreases as N_{IQ} is increased over more than two orders of magnitude. σ_L is slightly overestimated for N_{IQ} of approximately 10, but the data is in excellent agreement to that predicted by equation 3.7 for N_{IQ} greater than 30.

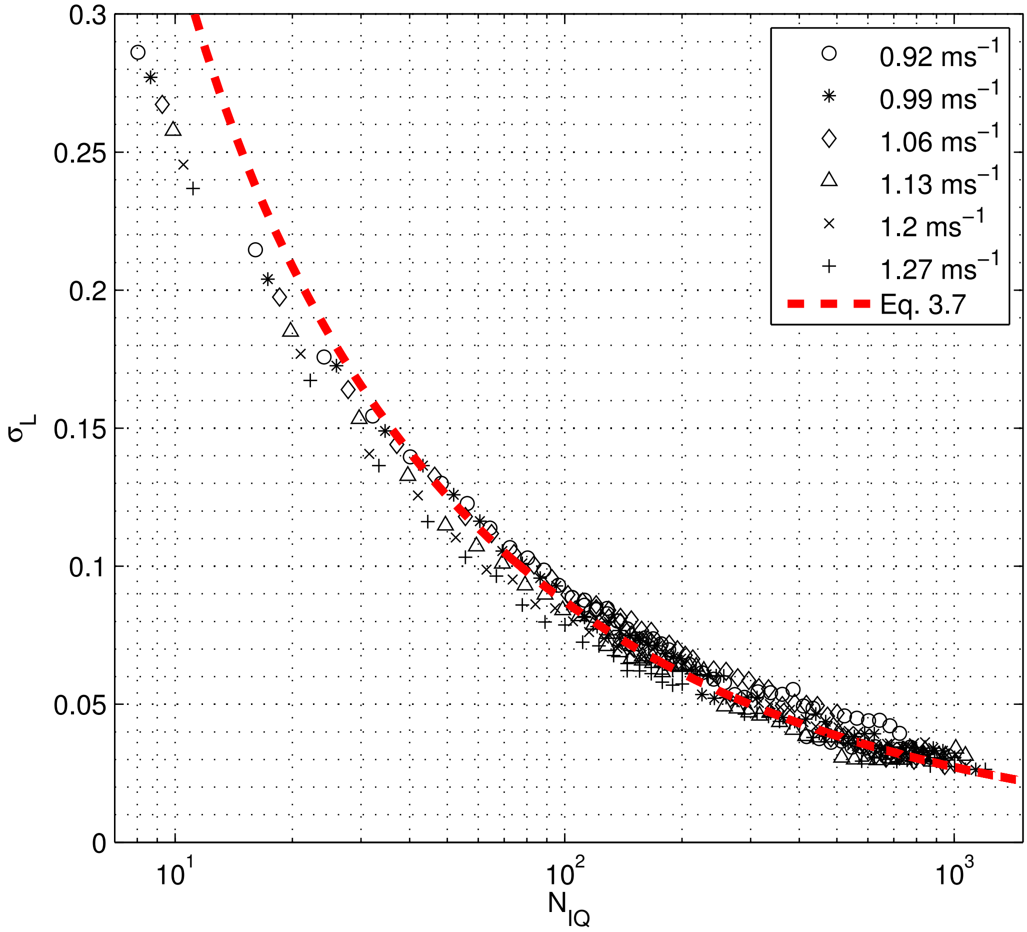

Figure 3.4 σ_L as a function of the number of independent I and Q samples used to estimate L for high SNR measurements in drizzle ($Z_{DR} < 0.1$ dB, SNR > 40 dB) at 1203 UTC on 6 February. Different markers correspond to different Doppler spectral widths.

3.3 Comparison with existing methods

In this section, these new error statistics are compared with existing methods in the literature. From observations of ρ_{hv} in rain, the bright-band and ice, Illingworth and Caylor (1991) derived empirically the relationship between their mean $\hat{\rho_{hv}}$ estimates and their standard deviation:

$$\sigma^{IC}_{\rho_{hv}} \simeq \frac{1.25(1 - \hat{\rho_{hv}})}{\sqrt{n}} \tag{3.12}$$

where n is the number of 0.2 s time-series they used to estimate the mean ρ_{hv}. Using a linear perturbation technique, Torlaschi and Gingras (2003) derive the following equation for the standard deviation on a ρ_{hv} measurement:

$$\sigma_{\rho_{hv}}^{TG} = \frac{1 - \bar{\rho_{hv}}^2}{\sqrt{2N_I}} \tag{3.13}$$

where N_I is the number of independent radar reflectivity samples used in its estimation. Note that $\overline{\rho_{hv}}$ in equation 3.13 is the "true" correlation coefficient one is attempting to measure (rather than the measured value, $\hat{\rho_{hv}}$). This equation represents the standard deviation for infinite SNR conditions, and is valid for simultaneous or accurately interpolated H and V sampling. Neither of these techniques are particularly useful, relying on either knowing a-priori the true correlation coefficient one is attempting to measure (Torlaschi and Gingras, 2003), or a number of time-series (Illingworth and Caylor, 1991), whereas physically one would expect the uncertainty to be related to time. It is not possible to compare the method of Illingworth and Caylor (1991) with the proposed method as σ_v for their data is unknown, and therefore the number of independent pulses in their time-series cannot be quantified.

Figure 3.5a shows the errors on $\hat{\rho_{hv}}$ calculated using the new method compared to those calculated using the linear perturbation method of Torlaschi and Gingras (2003) as a function of N_{IQ} in rain ($\overline{\rho_{hv}}$ is 0.98). The magnitudes of the upper confidence bounds are largely similar, however, for all N_{IQ} the lower confidence interval is higher (i.e. smaller deviations from $\overline{\rho_{hv}}$ are predicted) for the Torlaschi and Gingras (2003) method due to the asymmetric nature of the new confidence intervals on $\hat{\rho_{hv}}$. The largest difference is for small N_{IQ}. As N_{IQ} increases, both the upper and lower confidence intervals for each method converge. Although Figure 3.5a serves as a useful illustration of the difference between the methods, they are not strictly comparable in practice: the error calculation of Torlaschi and Gingras (2003) relies on knowledge of $\overline{\rho_{hv}}$ which in reality is unknown. Conversely, the new method requires no a-priori knowledge of $\overline{\rho_{hv}}$, and so is of much greater practical use.

Figure 3.5b illustrates the theoretical bias introduced by averaging many short samples of $\hat{\rho_{hv}}$, rather than $\hat{L}$, in rain ($\overline{\rho_{hv}}$ is 0.98). This bias is large for small N_{IQ}. For example, when N_{IQ} is 10, the bias on $\hat{L}$ is 0.1, which is significant for the purpose of estimating μ in rainfall (see chapter 5). Since the radar bright band has a lower $\overline{\rho_{hv}}$,

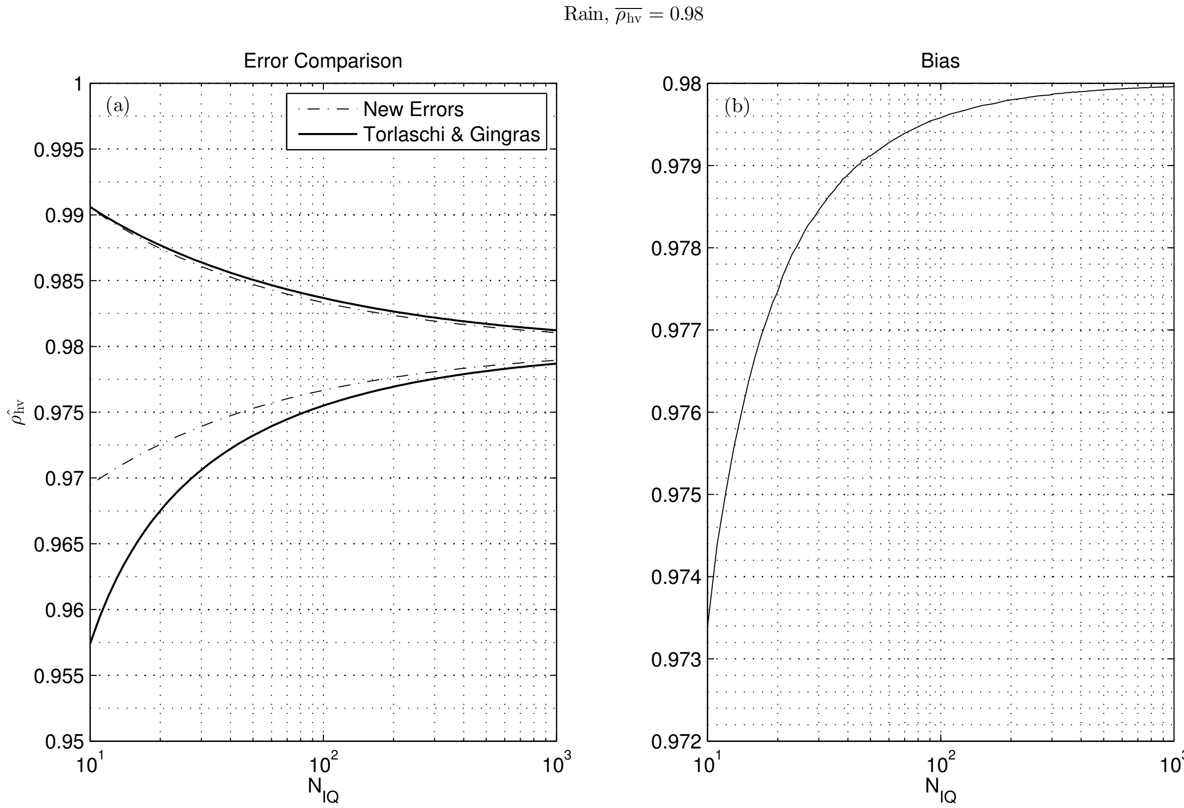

Figure 3.5 (a) A comparison of the confidence intervals calculated using the new method and that of Torlaschi and Gingras (2003) in rain ($\overline{\rho_{hv}} = 0.98$) and (b) the bias introduced by averaging $\hat{\rho_{hv}}$ instead of $\hat{L}$, as a function of N_{IQ}. For all N_{IQ}, the lower confidence interval is higher for the Torlaschi and Gingras (2003) method, particularly for lower N_{IQ}, due to the asymmetric nature of the confidence intervals on ρ_{hv} using the new method. Averaging $\hat{\rho_{hv}}$ and not $\hat{L}$ for small N_{IQ} can lead to a large bias.

this bias has a much larger effect and could potentially lead to mis-classification. It is not important whether spatial or temporal averaging is used to increase the number of independent I and Q samples, as long as $\overline{\rho_{hv}}$ does not vary substantially over the scales considered.

3.4 Practical measurement of ρ_{hv}

To fully exploit L and its statistical properties, some practical considerations for the measurement of ρ_{hv} must first be considered.

3.4.1 Effect of alternate sampling

When estimating the correlation coefficient, the non-simultaneous transmission and reception of H and V pulses must be accounted for. Assuming a Gaussian autocorrelation function to correct for this staggered sampling (Sachidananda and Zrnic, 1989) can lead to unphysical samples where $\hat{\rho_{hv}}$ is greater than 1 (Illingworth and Caylor, 1991). In this analysis, a cubic polynomial interpolation is employed to obtain H and V power estimates at the intermediate sampling intervals (Caylor, 1989), which is very effective. The interpolation scheme works well: for drizzle with $\overline{L}$ equals 2.4 ($\overline{\rho_{hv}}$ equals 0.996), the average values of $\hat{L}$, binned by σ_v, are constant to within ± 0.02 as σ_v varies between 0.1—2 ms^{-1}. This is evidence of successful interpolation, since there is no systematic trend to lower L values at higher spectral widths.

3.4.2 Signal-to-noise ratio

The addition of noise to the received signals acts to reduce the correlation between H and V time-series. The reduction factor, f, has been shown by Bringi *et al.* (1983) to vary predictably as:

$$f = \frac{1}{\left(1 + \frac{1}{SNR_H}\right)^{\frac{1}{2}} \left(1 + \frac{1}{SNR_V}\right)^{\frac{1}{2}}} \tag{3.14}$$

for simultaneous (or accurately interpolated) H and V sampling, where SNR$_H$ and SNR$_V$ are the signal-to-noise ratios for the H and V polarisations respectively. This was verified by Illingworth and Caylor (1991) with measurements of ρ_{hv} in drizzle. However, instrumental effects (described in Section 3.4.4 below) will have the same effect of adding uncorrelated noise, and so in practice these theoretical maximum values are never reached.

3.4.3 Effect of phase error

To avoid a bias in $\hat{\rho_{hv}}$ due to random phase error from the magnetron system (Liu *et al.*, 1994), the powers of the received echoes are correlated as opposed to the complex I and Q signals, and the square root is taken, following Illingworth and Caylor (1991).

3.4.4 Instrumental effects

Even in drizzle with very high SNR, antenna imperfections and other effects such as irregular magnetron pulse timing and pulse shape reproducibility will cause measured ρ_{hv} to always be less than 1 (Illingworth and Caylor, 1991; Liu *et al.*, 1994) as effectively they cause the H and V pulses to sample slightly different volumes. Here, a method to quantify and account for this bias is proposed, analogous to the SNR factor (equation 3.14) suggested by Bringi *et al.* (1983). H and V echoes can be considered to consist of two parts: a common sample volume, and parts of each sample volume which are unique to a particular polarisation. By treating the former as "signal" and the latter as unwanted "noise", an equation similar to equation 3.14 is obtained. Full details are provided in appendix A. The practical upshot is that the measured ρ_{hv} is the "true" ρ_{hv} multiplied by some dimensionless factor, f_{hv}^{max}, relating to how well matched the H and V sample volumes are. For spherical drops, $\overline{\rho_{hv}}$ should be unity. The estimates of $\overline{\rho_{hv}}$ for all such data should therefore be equal to f_{hv}^{max}. When comparing observations with simulated ρ_{hv} in this thesis, each of the predicted values is multiplied by f_{hv}^{max} so that they are directly comparable to the observations. ρ_{hv} has been measured in drizzle (Z_{DR} less than 0.1 dB) for a large number of samples on several days. Typically, f_{hv}^{max} is approximately 0.996, but varies by $\pm$ 0.001 from day to day, which is possibly the result of slightly irregular magnetron pulse timing and shape reproducibility for the CAMRa system, which may be temperature dependent. For this reason, f_{hv}^{max} has been determined individually for each case in this thesis.

3.5 Summary

At present, quantitative use of ρ_{hv} is hampered by lack of rigorous confidence intervals accompanying the ρ_{hv} estimates. A new variable $L = -\log_{10}(1-\rho_{hv})$ is defined that is Gaussian distributed with a width predictable by the number of independent I and Q samples, which in turn can readily be estimated using the Doppler spectral width. This allows, for the first time, the construction of rigorous confidence intervals on each ρ_{hv} measurement. The predicted errors using this new method were verified using high quality measurements in drizzle from the Chilbolton Advanced Meteorological Radar.

The proposed error estimation method is of much greater practical use compared to existing methods, as it does not require knowledge of the unknown "true" ρ_{hv} that one is trying to estimate. The method works for both simultaneous or accurately interpolated alternate sampling. However, it does not work for alternate estimators which rely on the Gaussian autocorrelation function to estimate the zero-lag correlation between H and V pulses (Sachidananda and Zrnic, 1989), where ρ_{hv} estimates can be greater than 1. Failure to use the transform L when averaging short time-series will lead to significant biases in correlation coefficient estimates. This is particularly important for operational ρ_{hv} applications that typically use very short dwell times.

A new technique to account for the imperfect co-location of H and V sampling volumes on ρ_{hv} measurements is also presented which is necessary when comparing theoretical and observed ρ_{hv}.

Chapter 4

Retrieval of pristine ice crystal microphysics in Type II mixed-phase clouds

4.1 Motivation

The microphysical properties of ice crystals are linked to the microphysical processes that created them, and the conditions in which they have grown. Ice crystal shape determines their scattering properties, growth rate and fall speeds, hence cloud scattering properties, microphysical evolution, precipitation rate and cloud lifetime. Furthermore, estimates of ice mass, or number concentration require accurate knowledge of ice particle shape (Westbrook and Heymsfield, 2011). An improved knowledge of their shape, density and fall speeds is therefore essential to understanding these processes and improving their representation in numerical models. Better measurements of these properties are particularly required in Type II mixed-phase clouds which are poorly understood, yet chapter 2 suggests are a common occurrence.

Several studies (Hall *et al.*, 1984; Wolde and Vali, 2001; Hogan *et al.*, 2002, 2003a; Bechini *et al.*, 2011; Kennedy and Rutledge, 2011; Andrić *et al.*, 2013; Moisseev *et al.*, 2015) have noted the existence of strong polarimetric radar signatures above the melting layer. For example, Hall *et al.* (1984) report Z_{DR} greater than 4 dB at the top of stratiform clouds. Hogan *et al.* (2002) observe values of Z_{DR} greater than 3 dB embedded within stratiform ice clouds, and show that these Z_{DR} values tend to be associated with the presence of SLW. Kennedy and Rutledge (2011) observe significant increases in the specific differential phase, K_{DP} (the range derivative of the propagation differential phase shift, which is sensitive to the number and shapes of aligned crystals) at temperatures of about $-15°$C. Interestingly, these were typically situated about

500 m below areas of enhanced Z_{DR}. They conclude that this signature was caused by the presence of dendritic particles with diameters of 0.8—1.2 mm with bulk densities greater than 0.3 g cm^{-3}. Similar enhancements of K_{DP} from 27 days of stratiform precipitation using X (λ approximately 3 cm) and C-Band (λ approximately 5 cm) radar measurements were reported by Bechini *et al.* (2011). They show that for over 70% of cases, the maximum value of K_{DP} above the freezing level was found between -10 and -18°C, and like Kennedy and Rutledge (2011) conclude that the enhancement was most likely produced by dendritic crystals. Furthermore, Bechini *et al.* (2011) present evidence that these enhanced K_{DP} signatures aloft are positively correlated with surface precipitation rate in stratiform rainfall, suggesting that this dendritic ice growth is important. Using a two-moment bulk microphysical model coupled with electromagnetic scattering calculations, Andrić *et al.* (2013) attempted to reconcile vertical profiles of observed and modelled Z_H, Z_{DR}, ρ_{hv} and K_{DP} at S-band. The model microphysics scheme, which included ice crystal nucleation, depositional growth and aggregation, was able to reproduce the shape of the observed profile features, which suggests that vapour deposition and aggregation are able to explain most of the observed radar signatures. However, the magnitudes of the predicted radar variables were not accurately reproduced, implying microphysical processes are either not correctly represented or are missing. Unlike single-layer mixed-phase clouds, multi-layered systems can be complicated by additional microphysical processes such as seeding of SLW layers by ice crystals falling from above (Fleishauer *et al.*, 2002), and riming (Lamb and Verlinde, 2011).

Differential reflectivity (see section 1) is a measure of reflectivity-weighted mean aspect ratio, and so is ideally suited to investigation of ice particles shapes. Although high values of Z_{DR} always indicate the presence of pristine crystals and by implication mixed-phase conditions (Hogan *et al.*, 2003a), its interpretation in deep frontal clouds is ambiguous when these pristine crystals are present amongst other crystals with different shapes, such as aggregates. Aggregate crystals largely consist of air, so have an "effective" dielectric factor proportional to the bulk density of the air-ice mixture (Batten, 1973). This value is typically much less than pure ice (0.917 gcm^{-3}), giving aggregates a small Z_{DR} value (0 — 0.5 dB). Since Z_{DR} is reflectivity-weighted, the presence of even a few (but much larger) aggregate crystals can strongly influence the Z_{DR} measurement (Bader *et al.*, 1987), essentially masking the contribution from pristine oriented crystals. Irregular polycrystal shapes tend to be approximately spherical to the radar and therefore also act to mask the Z_{DR} from the pristine oriented crystals. In order to fully utilise Z_{DR} measurements in deep frontal clouds, the masking effect of the aggregates and/or polycrystals must be removed.

The co-polar correlation coefficient responds to mixtures of particle shapes within a radar sampling volume, thus in Type II mixed-phase clouds that contain pristine oriented crystals and aggregates, one would expect reductions of ρ_{hv} and elevated Z_{DR} signatures. Such reductions have been noted (Moisseev *et al.*, 2009; Andrić *et al.*, 2013), but the quantitative microphysical information contained within ρ_{hv} is yet to be fully exploited. In this chapter, a novel retrieval technique is presented that utilises the variable L, introduced in chapter 3 to reveal the "true" Z_{DR} of the pristine oriented crystals that is otherwise masked by the presence of aggregates. In addition, their contribution to the observed radar reflectivity is retrieved.

4.2 Retrieval development

The variable ρ_{hv} (and its more useful form, L, see chapter 3) contains important microphysical information about the variety of shapes within a sampling volume. Since pristine ice crystal growth in embedded mixed-phased regions causes both an increase in the reflectivity-weighted aspect ratio and overall shape diversity, measurements of L and Z_{DR} are intrinsically linked to pristine oriented crystal shape and their relative contribution to the radar signal. The exploitation of this property forms the basis of the retrieval. For simplicity, the following assumptions are made:

(1) Embedded mixed-phase regions consist only of pristine crystals and pseudo-spherical aggregates or irregular polycrystals, and therefore can be represented by two distinct ice crystal populations. Hereafter, the terms aggregates and polycrystals will be used interchangeably to refer to the pseudo-spherical "background" ice particles

that mask the signal from pristine crystals.

(2) Pristine oriented crystals have a fixed aspect ratio, and fall with their primary axis aligned horizontally, with no flutter (see section 4.3.3). The effect of relaxing of this assumption is discussed in section 4.3.6.

4.2.1 Derivation

Under assumption 1, Z_{DR} can be written in terms of the radar reflectivity contributions from each crystal type:

$$Z_{DR} = \frac{\sum |S_{HH}|^2}{\sum |S_{VV}|^2} = \frac{Z_H}{Z_V} = \frac{Z_H^A + Z_H^P}{Z_V^A + Z_V^P} \tag{4.1}$$

where $\sum S_{HH}$ and $\sum S_{VV}$ are the sums of the co-polar elements of the backscattering matrix (see section 1.3) over all ice crystals; the superscripts A and P correspond to the aggregate and pristine crystal contributions respectively. Dividing both the numerator and denominator by Z_H^A, and assuming polycrystals/aggregates appear spherical to the radar (Z_H^A is equal to Z_V^A):

$$Z_{DR} = \frac{1 + \frac{Z_H^P}{Z_H^A}}{\frac{Z_V^A}{Z_H^A} + \frac{Z_V^P}{Z_H^A}} \tag{4.2}$$

If the pristine crystals all have a fixed aspect ratio, the "intrinsic" Z_{DR} (i.e. the Z_{DR} that would be observed if only the pristine crystals were sampled by the radar) can be defined as:

$$Z_{DRI}^P = \frac{\sum^P |S_{HH}|^2}{\sum^P |S_{VV}|^2} = \frac{Z_H^P}{Z_V^P} \tag{4.3}$$

Then, by defining the relative contribution of Z_H from the pristine oriented crystals to Z_H of the aggregates:

$$C = \frac{\sum^P |S_{HH}|^2}{\sum^A |S_{HH}|^2} = \frac{Z_H^P}{Z_H^A} \tag{4.4}$$

Z_{DR} can be written as:

$$Z_{DR} = \frac{1 + C}{1 + \frac{C}{Z^P_{DRI}}}. \tag{4.5}$$

Similarly, for ρ_{hv}, beginning with its definition:

$$\rho_{hv} = \frac{\sum S_{HH} S_{VV}}{\sqrt{\sum |S_{HH}|^2 + \sum |S_{VV}|^2}}, \tag{4.6}$$

and splitting into contributions from each crystal type:

$$\rho_{hv} = \frac{\sum^A S_{HH} S_{VV} + \sum^P S_{HH} S_{VV}}{\sqrt{(\sum^A |S_{HH}|^2 + \sum^P |S_{HH}|^2)(\sum^A |S_{VV}|^2 + \sum^P |S_{VV}|^2)}}, \tag{4.7}$$

Recognising that:

$${S^P_{VV}}^2 = \frac{{S^P_{HH}}^2}{Z^P_{DRI}}, \tag{4.8}$$

if all pristine crystals have a fixed aspect ratio, then:

$$\rho_{hv} = \frac{\sum^A {S_{HH}}^2 + \sum^P {S_{HH}}^2 / \sqrt{Z^P_{DRI}}}{\sqrt{(Z^A_H + Z^P_H)(Z^A_V + Z^P_V)}}. \tag{4.9}$$

Dividing both the numerator and denominator by Z^A_H yields:

$$\rho_{hv} = \frac{1 + \frac{C}{\sqrt{Z^P_{DRI}}}}{\sqrt{(1 + C) \times \left(1 + \frac{C}{Z^C_{DRI}}\right)}} \tag{4.10}$$

The imaginary components of S_{HH} and S_{VV} are ignored in this derivation; absorption is very small at these wavelengths for ice ($\mathrm{Im}(S_{HH}) \ll \mathrm{Re}(S_{HH})$). As discussed in chapter 3, ρ_{hv} is more useful in the form $L = -\log_{10}(1 - \rho_{hv})$ and so is transformed for use in the retrieval. Two measurements, ρ_{hv} and Z_{DR}, can now be directly related to the two "unknown" parameters, C and Z^P_{DRI}. This forms the basis of the retrieval.

Using equations 4.5 and 4.10, a look up table for L and Z_{DR} was created for C ranging between -20 and 0 dB, and Z^P_{DRI} between 0.1 and 10 dB. Figure 4.1 shows

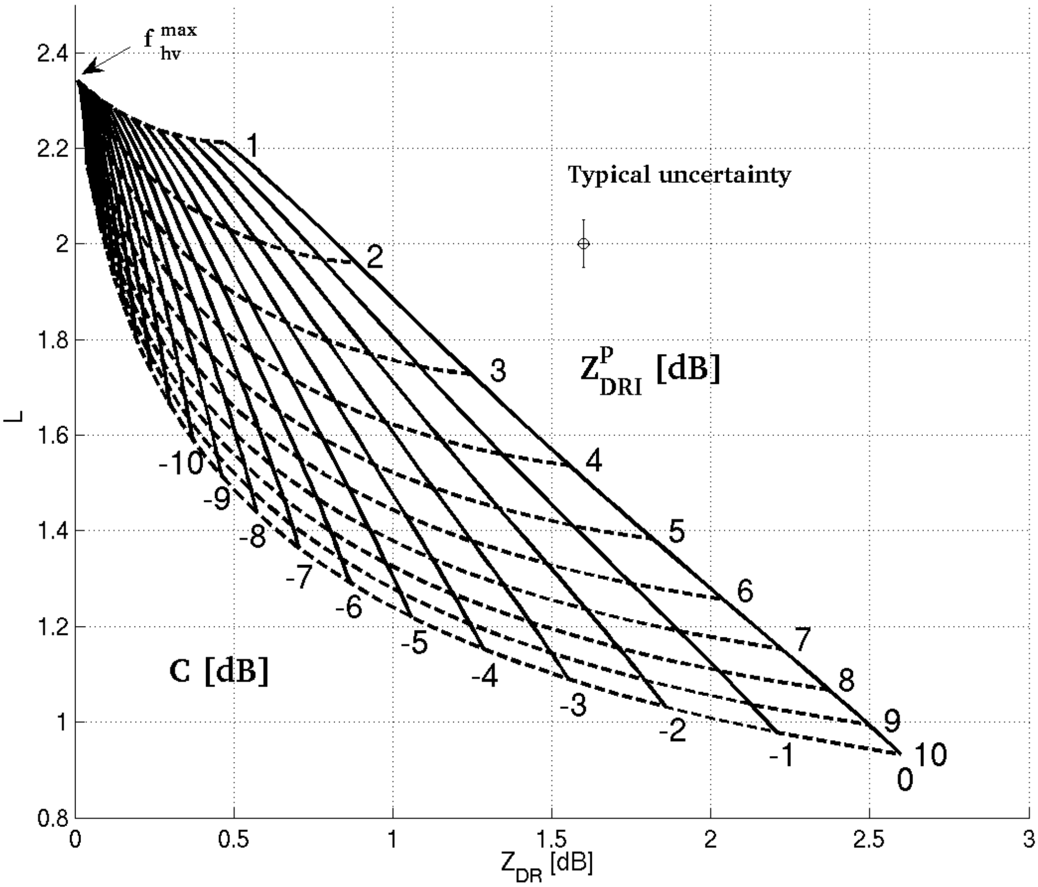

Figure 4.1 Schematic illustrating predicted C (solid lines) and Z^P_{DRI} (dashed lines) as a function of observed L and Z_{DR} based on equations 4.5 and 4.10. A representative f^{max}_{hv} (see section 3.4.4) and typical measurement uncertainty is shown.

how measurements of L and Z_{DR} are related to C and Z^P_{DRI}. The inherent limit of the radar system for the following case study (described in 3.4.4) has been accounted for by multiplying ρ_{hv} in equation 4.10 by f^{max}_{hv}; this gives L equal to 2.35 when no pristine oriented crystals are present. The typical measurement uncertainty on L and Z_{DR} observations (after averaging described in section 4.3) is also shown. When C is small, it is very difficult to distinguish between the possible values of C and Z^P_{DRI}, particularly given the magnitude of the measurement uncertainty. However this becomes easier as C increases, as the lines of constant C and Z^P_{DRI} broaden. The mostly likely pair of C and Z^P_{DRI} are obtained by minimising the differences between the observed and predicted L and Z_{DR} values in the look-up table, weighted by their measurement uncertainty.

4.2.2 Adjusting look-up table for SNR

As discussed in section 3.4.2, ρ_{hv} is sensitive to the signal-to-noise ratio. In order to avoid biases in the retrieval due to poor SNR, look-up tables were created for a range of possible SNR values. The expected ρ_{hv} observation for each C and Z_{DRI}^{P} pair was adjusted using equation 3.14, and translated into L space. This allows the retrieval to be applied even when SNR is relatively low (often in lower Z regions of ice cloud). However, doing this has the effect of increasing the impact of measurement uncertainty on retrieved C and Z_{DRI}^{P} uncertainty, as the same uncertainty in L and Z_{DR} spreads over a larger range of C and Z_{DRI}^{P} in the adjusted look-up tables. Data with SNR less than 10 dB was not included in this analysis. This method is preferable to correcting the observed ρ_{hv} value itself for SNR effects, as σ_L can be used directly.

4.3 Case study I: 31 January 2014

In this section, data collected during the passage of a warm front that crossed over the UK on 31 January 2014 is presented. Figure 4.2 shows the observed radar reflectivity (Z), differential reflectivity (Z_{DR}) and L for an RHI scan taken at 1501 UTC. The melting layer can be clearly identified as the thin layer of enhanced Z (larger than 35 dBZ) at a height of approximately 1 km. Co-located is an elevated Z_{DR} signature, which occurs as ice crystals with positive aspect ratios begin to melt and become water coated, increasing their dielectric constant and therefore radar reflectivity in each polarisation. A decrease in L is also seen due to the mixture of shapes and phases in the melting layer. However, the polarimetric signature of interest for this study can be identified at approximately 4 km in height.

To analyse this signature, figure 4.3 shows a vertical profile of Z, Z_{DR}, L and the temperature profile imported from the operational ECMWF model (indicated by the dashed black line in figure 4.2). The red line is L, corrected for the observed SNR (using equation 3.14). This is the “effective” L that is used in the retrieval once the look-up tables have been adjusted for SNR (as discussed in section 4.2.2). The profile is only shown between the heights of 3 and 5 km, through the polarimetric signature of interest.

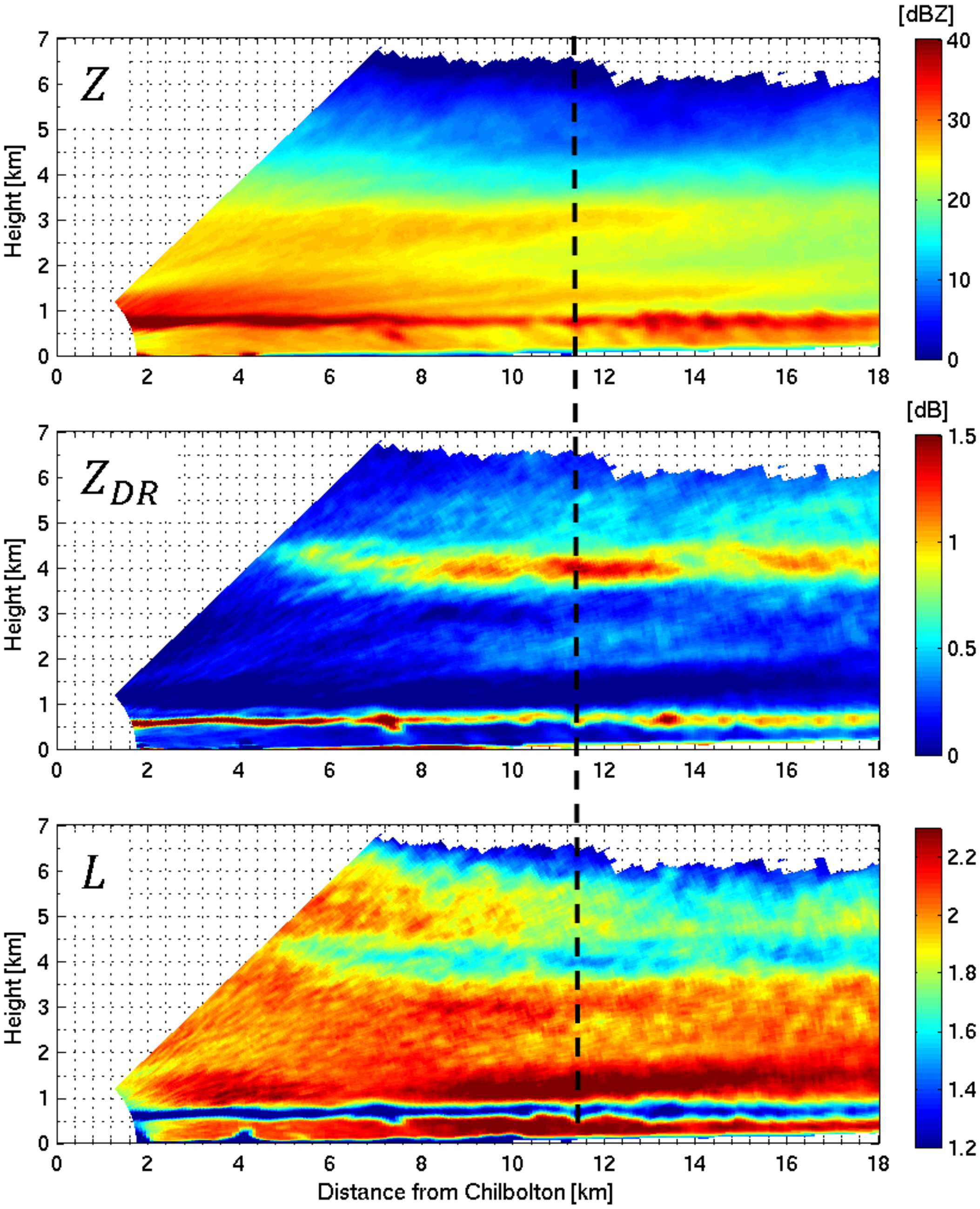

Figure 4.2 RHI scan at 1501 UTC on 31 January 2014 showing Z, Z_{DR} and L. Data has been averaged to 1° and 300 m in range, and is only shown for SNR > 10 dB.

At 5 km, Z is 10 dBZ, whilst Z_{DR} is around 0.5 dB. This is indicative of irregularly shaped polycrystals or pseudo-spherical aggregates. L is relatively high, indicating that the ice crystals producing this Z_{DR} have approximately the same shape. Descending below 4.8 km, Z and Z_{DR} begin to increase with decreasing altitude, peaking just below

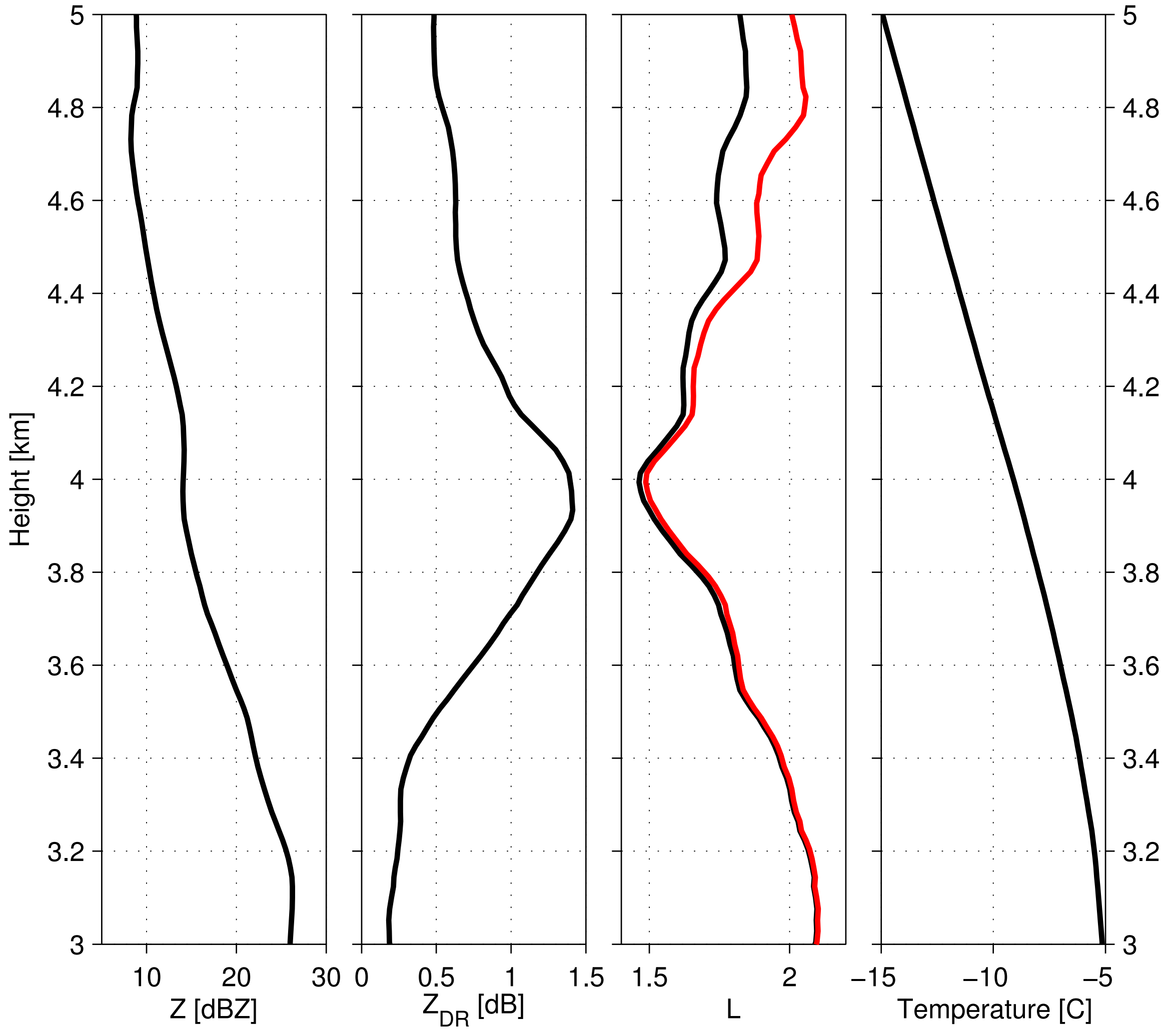

Figure 4.3 Vertical profiles of Z, Z_{DR}, L and temperature at 11.5 km from Chilbolton at 1501 UTC on 31 January 2014 (indicated by dashed black line on figure 4.2). The red line is the "effective" L, i.e. the L measurement adjusted for SNR to illustrate the "real" profile used in the retrieval.

4 km, whilst L decreases to a minimum of 1.5 at 4 km. Interestingly, the L minima also occurs about 50 m higher than the Z_{DR} maxima, suggesting that maximum shape diversity occurs slightly before pristine oriented crystals contribute their most to the radar reflectivity. This feature also appears evident in vertical profiles presented by Andrić *et al.* (2013).

This signature suggests that pristine oriented crystals with large aspect ratios are nucleating at approximately 4.8 km, increasing the diversity of shapes in the sample volume. As the crystals grow by vapour deposition, their contribution to Z increases,

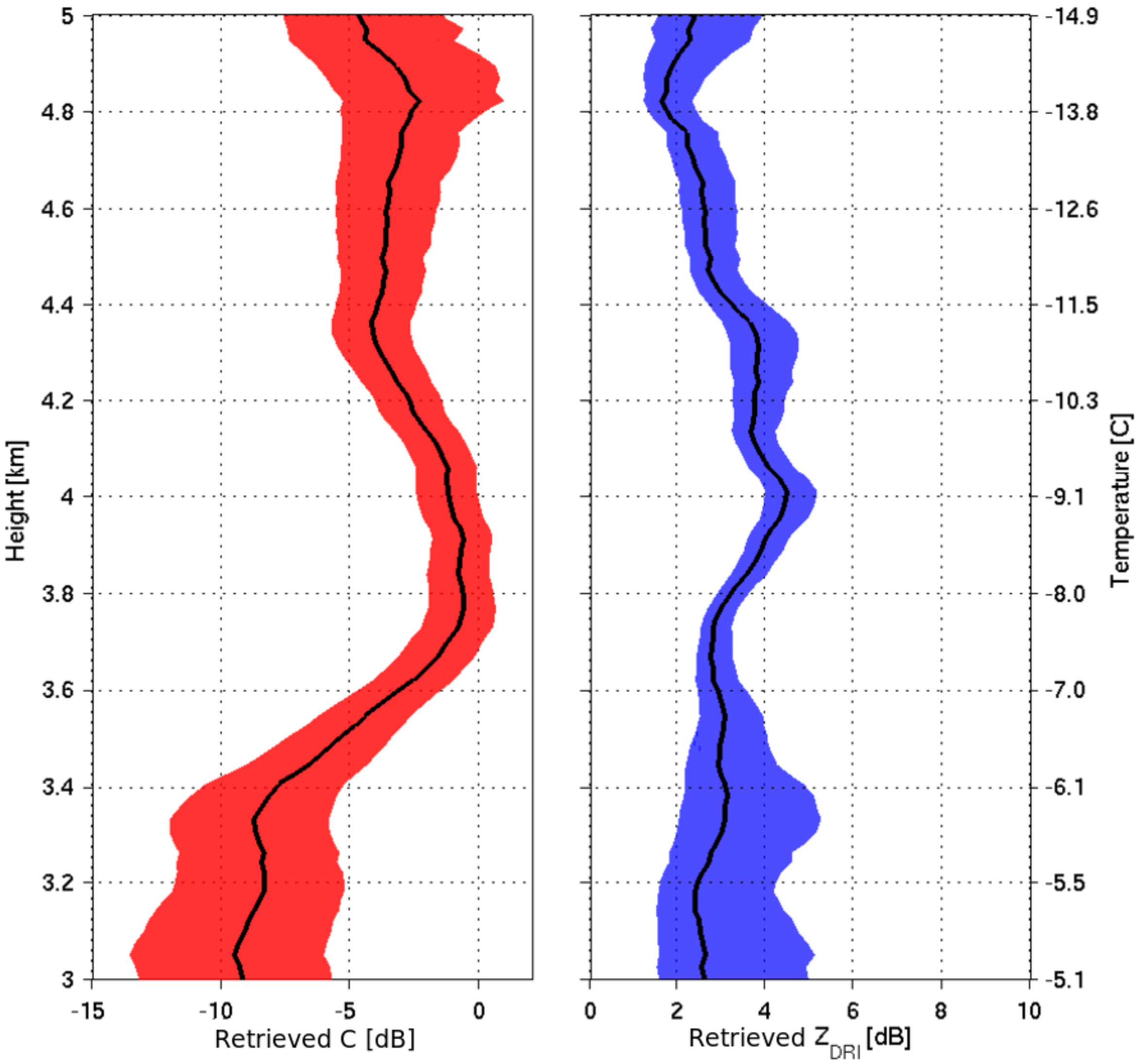

Figure 4.4 Vertical profile of retrieved C and Z^P_{DRI} as a function of height and temperature at 11.5 km from Chilbolton at 1501 UTC on 31 January 2014.

Z_{DR} increases, and L decreases, peaking at approximately 4 km. The temperature at 4.8 km is around -14°C; crystals nucleated at this temperature are most likely to be plate-like (Bailey and Hallett, 2009). The temperature at which the L minimum and Z_{DR} maximum are observed is approximately -9°C. Between 4 and 3.5 km, Z increases by 10 dB, corresponding with a rapid decrease in Z_{DR} and increase in L. This is characteristic of aggregation; the crystals are becoming larger and less dense, while overall shape diversity is decreasing. Just before the melting layer is reached, Z_{DR} is very low (approximately 0.2 dB), and L is very high (approximately 2.3), which is indicative of a monodisperse aggregate population.

Before the retrieval was applied to these profiles, data was averaged over 10 rays (1°) and 4 range gates (300 m) to increase the number of independent I and Q samples (N_{IQ}) and improve the precision of the measurements. Figure 4.4 shows retrieval profiles of C (left) and Z^P_{DRI} (right) for the the observations shown in figure 4.3. The shaded areas depict the uncertainty in the retrieval that results from measurement uncertainty in L and Z_{DR}. This range was calculated as the maximum and minimum possible retrieval values that could result from $L \pm \sigma_L$ and $Z_{DR} \pm \sigma_{Z_{DR}}$. The uncertainty in Z_{DR}, $\sigma_{Z_{DR}}$, was calculated using the method of Bringi and Chandrasekar (2001).

Firstly, examining the profile between 5 and 4.4 km in height, the retrieval reveals that the observed Z_{DR} of approximately 0.5 dB is actually the result of a pristine crystals with relatively large intrinsic Z_{DR}, of approximately 2.5 dB. However, this signal is being masked by aggregates; the contribution of the pristine oriented crystals to the radar reflectivity compared to the aggregates, C, is approximately -3 — -4 dB (approximately 40% that of the aggregates). Fluctuations in Z^P_{DRI} appear to correspond to a fluctuations in measured L; indeed, observation of figure 4.1 reveals that the retrieved Z^P_{DRI} value is most influenced by changes along the L axis. Similarly, the relatively steady behaviour of C can be explained by the fact that C is most influenced by changes in the Z_{DR} axis, and Z_{DR} is more smoothly varying. Between 4.4 and 4 km, both C and Z^P_{DRI} broadly increase. The largest Z^P_{DRI} of just over 4 dB is observed at 4 km in height. There is then a broad maxima in C between 4 and 3.7 km that corresponds to the location of the strongest Z_{DR} signature. Here, C is at its highest, at approximately -1 dB (or 80 % that of aggregates). This maximum C value is maintained down to about 3.7 km, whilst Z^P_{DRI} decreases back to 3 dB, where it remains constant even as C decreases to -8 dB at 3.4 km. The reduction in C implies that the newly formed crystals are aggregating; the relatively constant Z^P_{DRI} suggests that the shape of the remaining unaggregated crystals is constant. This figure demonstrates how the retrieval is able to provide an interpretation of pristine ice crystal properties in deep frontal clouds that was previously unavailable.

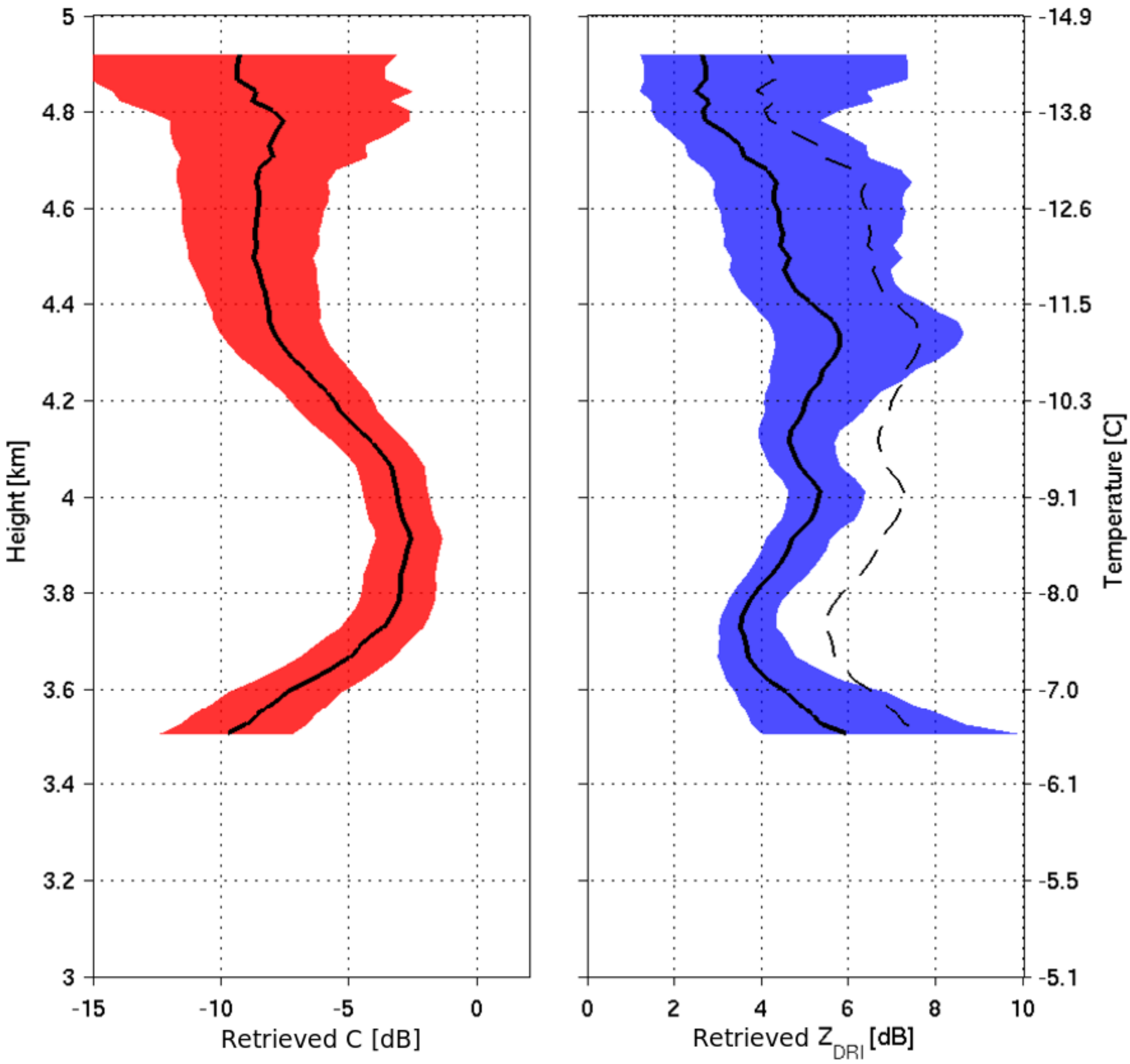

Figure 4.5 Vertical profile of Retrieved C and Z^P_{DRI} as a function of height and temperature at 11.5 km from Chilbolton at 1501 UTC on 31 January 2014. The dashed black line is the "true" Z^P_{DRI} that would be observed at an elevation angle of 0°. The retrieval is only shown when C is greater than -10 dB.

4.3.1 Accounting for non-spherical aggregates

The retrieval is based on the assumption that aggregates are perfectly spherical. In nature, this is not the case, and aggregates are commonly observed to be slightly non-spherical in shape to the radar, with a typical Z_{DR} of 0.2 — 0.3 dB (for example see just above the melting layer in figure 4.2). Assuming aggregates are perfectly spherical rather than slightly non-spherical will result in some of the Z_{DR} signal being mis-attributed to the pristine oriented crystals. It also causes shape diversity to be overestimated; non-spherical aggregates are more similar in shape to pristine oriented crystals. This in turn causes Z^P_{DRI} to be underestimated.

To account for these non-spherical aggregates, a fixed "intrinsic" Z_{DR} of irregular polycrystals or aggregates is assumed, defined as:

$$Z^A_{DRI} = \frac{Z^A_H}{Z^A_V}. \tag{4.11}$$

To account for this, equation 4.5 can been slightly modified to:

$$Z_{DR} = \frac{1+C}{\frac{C}{Z^P_{DRI}} + \frac{1}{Z^A_{DRI}}} \tag{4.12}$$

Similarly, Equation 4.10 can be written as:

$$\rho_{hv} = \frac{\frac{1}{\sqrt{Z^A_{DRI}}} + \frac{C}{\sqrt{Z^P_{DRI}}}}{\sqrt{(1+C) \times \left(\frac{1}{Z^A_{DRI}} + \frac{C}{Z^P_{DRI}}\right)}} \tag{4.13}$$

Figure 4.5 shows the same profiles as figure 4.4 but with Z^A_{DRI} is equal to 0.3 dB. Broadly, the profile characteristics remain similar to the case when Z^A_{DRI} is equal to 0 dB. Retrieved quantities are only shown where the polarimetric signature is strong enough to produce C greater than -10 dB. Two local maxima are observed at the same heights, and the broad maxima in C is still present between 4.4 and 3.5 km. However, the magnitudes of the retrieved quantities differ. C has typically decreased at all heights, whereas Z^P_{DRI} has typically increased. The peak in C is now approximately -3 dB rather than -1 dB, and typical Z^P_{DRI} values are now 5 rather than 4 dB. Retrieval uncertainty is slightly larger, because adjusting for Z^A_{DRI} puts the observed L and Z_{DR} into the more sensitive part of the forward model, therefore the same measurement uncertainty spans over a larger range of possible values. The precise magnitudes of these changes depend on the sensitivity of the forward model for each particular pair of L and Z_{DR} observations. This will be quantified in section 4.3.4.

The RHI scan used in this case study uses elevation angles up to 45°. As the elevation angle increases, the V polarisation increasingly samples the same plane as the H polarisation. Thus, for planar ice crystals, with increasing elevation angle, the "true" Z_{DRI}^{P} (i.e. that that would be seen at horizontal incidence) will become increasingly underestimated. For microphysical interpretation, it is therefore the Z_{DRI}^{P} corrected for elevation angle (θ), hereafter denoted $Z_{DRI}^{P}(0)$, that is of interest. With knowledge of the radar elevation angle, $Z_{DRI}^{P}(0)$ can be readily computed from $Z_{DRI}(\theta)$ by assuming they are hexagonal prisms and using the modified Gans-theory equations of Westbrook (2013). For this case study, $Z_{DRI}^{P}(0)$ is typically 2 dB larger than implied by the retrieval Z_{DRI}^{P} (shown by the dashed black line in figure 4.5). Details of this correction can be found in appendix B.

4.3.2 Estimating pristine oriented crystal density

An interesting feature of figure 4.5 is the variability and decreasing trend of Z_{DRI}^{P} as C increases. Z_{DRI}^{P} of an ice crystal is a function if its effective density and aspect ratio. The C signature suggests that there is strong vapour depositional growth between 4.4 and 3.8 km, but at the same time Z_{DRI}^{P} is decreasing. This is consistent with a decrease in the effective densities of plate-like crystals as they develop extensions or branch-like structures (Takahashi *et al.*, 1991).

The aspect ratios of thick plates tend to be small; their minor axes are relatively large compared to their major axis. Thin plates have much smaller minor compared to their major axes, and so have larger aspect ratios. Laboratory ice crystal growth experiments show that after just 3 minutes, plates, sectors and dendrites growing at -12.2, -14.4 and -16.5°C respectively have aspect ratios larger than 15 (Takahashi *et al.*, 1991). As can be seen in figure 1.9, most of the increase in a crystals Z_{DRI}^{P} occurs below this aspect ratio, and so Z_{DRI}^{P} is primarily a function of effective density. Z_{DRI}^{P} was computed assuming an aspect ratio of 15 for a range of effective densities; the effective density is then found by minimising the difference between the observed and predicted Z_{DRI}^{P} values.

At 4.3 km, before the rapid increase in C, $Z_{DRI}^{P}(0)$ is approximately 7.5 dB, which corresponds to an effective density of 0.90 gcm^{-3}. Just below the peak C (3.7 km), $Z_{DRI}^{P}(0)$ has dropped to approximately 5.5 dB, which corresponds to 0.63 gcm^{-3}. The assumption of much larger aspect ratios (e.g. 100) does not largely impact these effective densities; 7.5 dB and 5.5 dB correspond to 0.71 gcm^{-3} and 0.50 gcm^{-3} respectively. This range of effective densities is consistent with laboratory estimates for plate crystals nucleated at temperatures between -12 and -16°C (Takahashi *et al.*, 1991; Fukuta and Takahashi, 1999). This further supports the interpretation of the retrieved profiles: plates, initially with a density very close to pure ice, are growing rapidly by vapour deposition, eventually developing extensions or branches which are decreasing their effective density.

4.3.3 Retrieval of ice particle fall speeds

During this case study, at the same location as the strong L and Z_{DR} measurements, there was also an appreciable Differential Doppler Velocity (DDV) signatures. As discussed in section 1.3.4, DDV is sensitive to the relative contribution of pristine oriented crystals to aggregates, their shapes and fall velocity differences. Both C and Z^P_{DRI} are known from the retrieval in section 4.2. Therefore, with an assumption for Z^A_{DRI}, the information provided by measurements of DDV can be used to estimate the difference in fall speeds between the pristine oriented crystals and the aggregates. Starting with the definition of DDV:

$$DDV = \frac{U_H - U_V}{\sin\theta}, \tag{4.14}$$

where U_H and U_V are the Doppler velocity estimates for the H and V polarisations respectively, and θ is the elevation angle. As above, assuming two distinct ice particle populations of pristine crystals with fixed aspect ratio and aggregates, U_H and U_V can be written as:

$$U_H = \frac{Z^P_H \times V^{POC} + Z^A_H \times V^{AGG}}{Z^P_H + Z^A_H} \tag{4.15}$$

$$U_V = \frac{Z^P_V \times V^{POC} + Z^A_V \times V^{AGG}}{Z^P_V + Z^A_V} \tag{4.16}$$

where V^{POC} and V^{AGG} are the fall velocities of the pristine crystals and aggregates respectively. Dividing both the numerator and denominator of both equations by Z_H^P, and assuming Z_{DRI}^A yields:

$$U_H = \frac{V^{POC} + \frac{1}{C} \times V^{AGG}}{1 + \frac{1}{C}} \tag{4.17}$$

$$U_V = \frac{\frac{1}{Z_{DRI}^P} \times V^{POC} + \frac{1}{C \times Z_{DRI}^A} \times V^{AGG}}{\frac{1}{Z_{DRI}^P} + \frac{1}{C \times Z_{DRI}^A}} \tag{4.18}$$

Substituting the fall speed differences: $\Delta U = V^{AGG} - V^{POC}$ into equations 4.17, 4.18 and 4.14 yields:

$$DDV = \Delta U \times \frac{\frac{1}{C \times Z_{DRI}^P} - \frac{1}{C \times Z_{DRI}^A}}{\sin(\theta)\left(1 + \frac{1}{C}\right)\left(\frac{1}{Z_{DRI}^P} + \frac{1}{C \times Z_{DRI}^A}\right)} \tag{4.19}$$

Using this equation, a look-up table was created, and ΔU was estimated as the most likely value given the pair of retrieved C and Z_{DRI}^P at the location of the DDV measurements. The retrieved Z_{DRI}^P was corrected for elevation angle for microphysical interpretation, and Z_{DRI}^A was assumed to be 0.3 dB. Once ΔU is known, the individual fall speeds of each of the crystal type can be estimated using the observed vertical Doppler velocity from the vertically pointing 35 GHz Copernicus radar.

Figure 4.6 shows the observed Doppler velocity at each height, averaged between 14:50 and 15:10 UTC (black), and the estimated fall speeds of the pristine crystals (red) and aggregates (blue) for the 11.5 km profile in figure 4.3. The observed V initially decreases, consistent with the increasing contribution from slower falling pristine oriented crystals as the observed Doppler velocity is reflectivity-weighted. The fall speeds of the aggregate crystals are always larger than the observed Doppler velocity if C is finite; the larger C, the larger the aggregate fall speed must be to produce the observed V. The retrieved pristine crystal fall speeds are approximately 70 $\pm$10 cm s^{-1}. There is also variability in the profile which could simply be the result of using DDV, which can be quite noisy, especially for lower elevation angles where there is less component of the particle fall speeds in the Doppler velocity measurement. There is not an increase

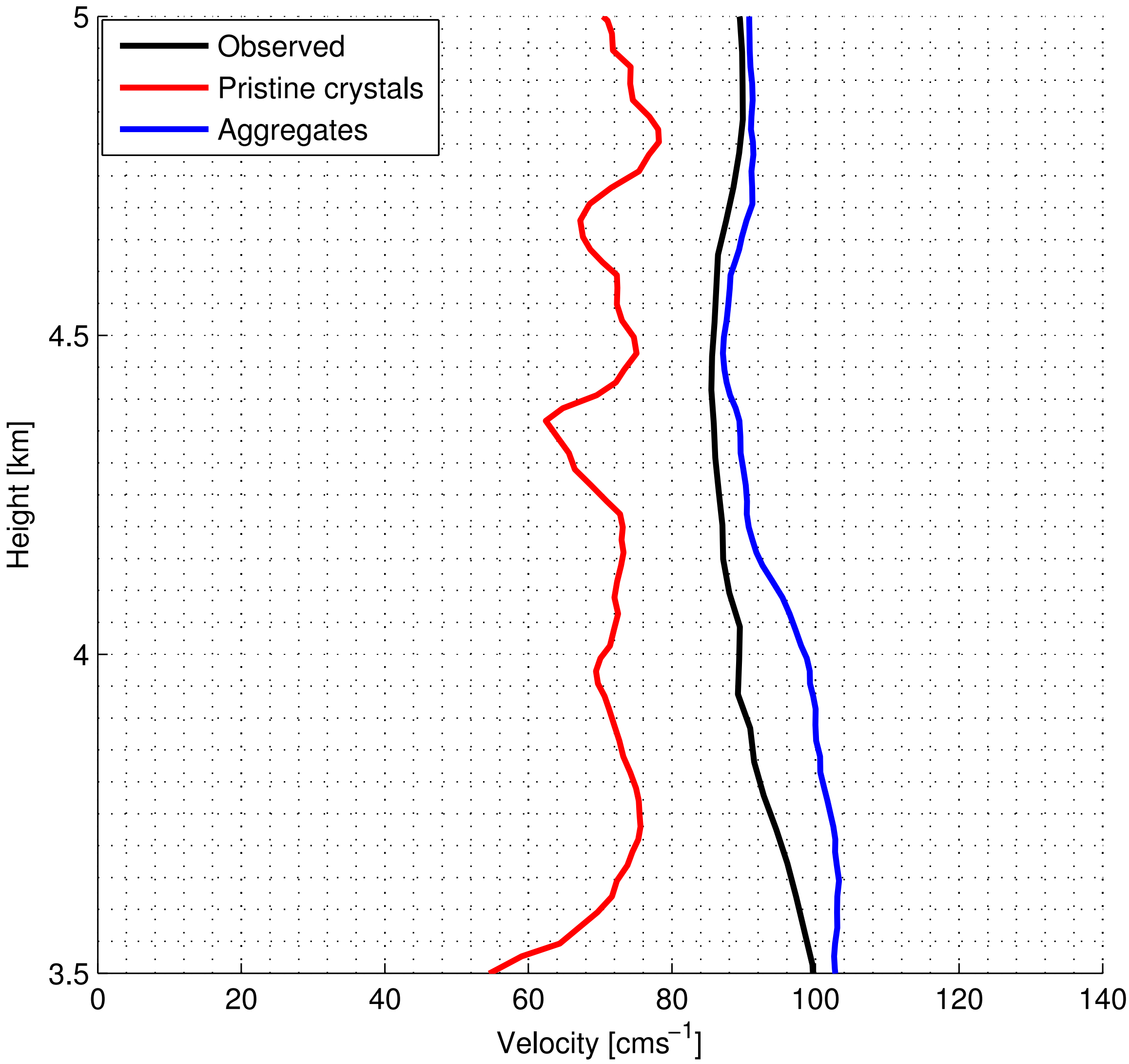

Figure 4.6 The observed Doppler velocity, averaged between 14:50 and 15:10 UTC from the vertically pointing 35 GHz Copernicus radar installed at Chilbolton (black), retrieved pristine oriented crystal fall speed (red) and aggregate crystal fall speed (blue) for the 31 January profile.

in fall speed with decreasing height as one might expect if these crystals are growing. However, the magnitude is consistent with the presence of large pristine crystals, or smaller, lightly rimed pristine crystals (Locatelli and Hobbs, 1974). This method could be useful to identify regions where riming is occurring (e.g. Yau and Rogers 1996). The additional microphysical insight into Type II mixed-phase clouds provided by using a combination of DDV, Z_{DR} and L would be interesting to investigate further in future work.

4.3.4 Sensitivity to the aggregate Z_{DR} assumption

In this section, the sensitivity of the retrieval to the assumption of aggregate Z_{DR} is investigated. To do this, L and Z_{DR} were forward modelled using Z_{DRI}^{A} assumptions of 0 and 0.3 dB. The sensitivity of the forward model is defined as the absolute difference in retrieved C and Z_{DRI}^{P} due to Z_{DRI}^{A}, for a given pair of L and Z_{DR} observations. Figure 4.7 shows the sensitivity of C (top) and Z_{DRI}^{P} (bottom) to assuming Z_{DRI}^{A} is 0.3 dB as opposed to 0 dB. Both C and Z_{DRI} are increasingly sensitive for higher L and lower Z_{DR}. This is not surprising, as the polarimetric signature here is weaker, and C and Z_{DRI}^{P} lines are almost indistinguishable (see figure 4.1). It is clear that C is most sensitive to the choice of Z_{DRI}^{A}, exhibiting sensitivity greater than or equal to 2.5 dB up to Z_{DR} equals 1 dB. This sensitivity decreases as Z_{DR} increases; for a Z_{DR} of 1.5 dB (the upper range of the data presented here), the sensitivity is 1 — 2 dB.

Z_{DRI}^{P} is also sensitive to the choice of Z_{DRI}^{A}, especially for low L (i.e. where retrieved Z_{DRI}^{P} values are highest). Above Z_{DR} equals 1 dB, the sensitivity is typically 1—2 dB. Clearly, care should be taken when interpreting the retrieval results, especially for weaker polarimetric signatures.

4.3.5 Accounting for pristine oriented crystal aspect ratio variability

Another assumption made in the retrieval is that all of the pristine oriented crystals have a fixed aspect ratio. In reality, ice crystals are nucleated at different depths within a SLW layer and can grow at different rates, leading to an eventual distribution of aspect ratios for a given crystal habit. Not accounting for a variety of crystal aspect ratios will cause retrieved Z_{DRI}^{P} for a given L measurement in the forward model to be overestimated. This is because the measured L includes a contribution from pristine crystal shape diversity, which would be misinterpreted as being the result of pristine crystals with more extreme aspect ratios. Consequently, it would cause C to be underestimated for a given Z_{DR} measurement.

The expected Z_{DR} value will not be affected by an increase in shape variety, as uniform distributions are defined about a fixed Z_{DRI}^{P} value, such that the "average"

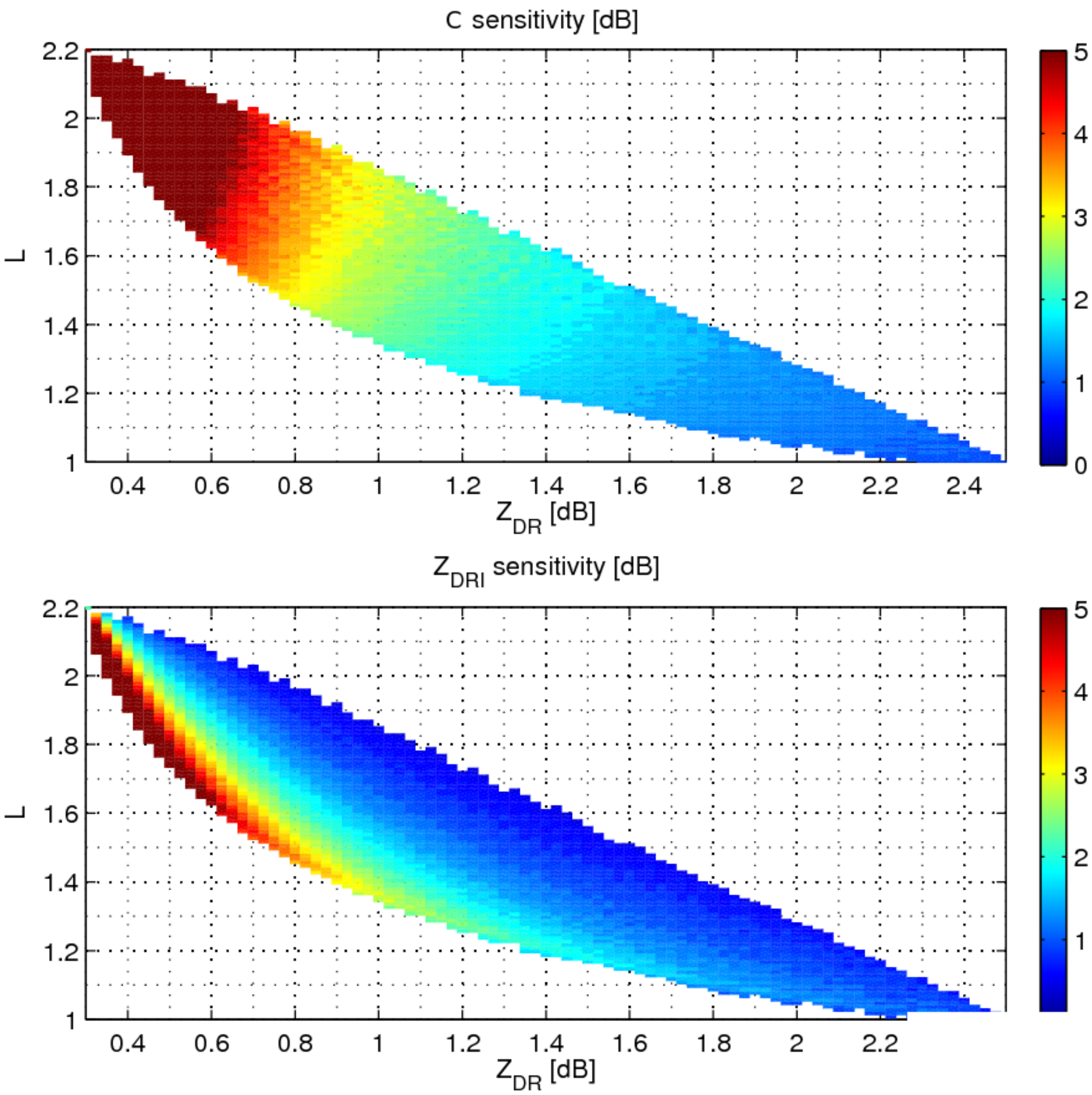

Figure 4.7 The sensitivity of retrieved C and Z^P_{DRI} to the assumption of Z^A_{DRI}, expressed as the difference between assuming $Z^A_{DRI} = 0.3$ dB as opposed to 0 dB.

Z^P_{DRI} remains the same. Therefore, Z_{DR} can be written identically to equation 4.5, but should be interpreted as the mean value of a distribution of Z^P_{DRI}. However, it will have an effect on L, which *is* sensitive to variability in shape. An equation can be derived in a similar manner to equation 4.10, using the definitions of C and Z^P_{DRI} given by equations 4.3 and 4.4.

Starting with the definition of ρ_{hv}, and separating to the contributions from each crystal type:

$$\rho_{hv} = \frac{\sum^A S_{HH}S_{VV} + \sum^P S_{HH}S_{VV}}{\sqrt{(\sum^A |S_{HH}|^2 + \sum^P |S_{HH}|^2)(\sum^A |S_{VV}|^2 + \sum^P |S_{VV}|^2)}} \tag{4.20}$$

Dividing both the numerator and denominator by Z_H^A, and assuming that aggregates are spherical (S_{HH} is equal to S_{VV}):

$$\rho_{hv} = \frac{1 + \frac{\sum^P S_{HH}S_{VV}}{Z_H^A}}{\sqrt{\left(1 + \frac{Z_H^P}{Z_H^A}\right)\left(\frac{Z_H^P}{Z_H^A} + \frac{Z_H^P}{Z_H^A}\right)}} \tag{4.21}$$

Noting that in the numerator,

$$\frac{\sum^P S_{HH}S_{VV}}{Z_H^A} = \frac{Z_H^P}{Z_H^P} \times \frac{\sum^P S_{HH}S_{VV}}{Z_H^A} = C \times \frac{\sum^P S_{HH}S_{VV}}{Z_H^P}, \tag{4.22}$$

$$C \times \frac{\sum^P S_{HH}S_{VV}}{Z_H^P} = C \times \frac{\sum^P S_{HH}S_{VV}}{\sqrt{\sum^P |S_{HH}|^2 \sum^P |S_{VV}|^2}} \times \sqrt{\frac{\sum^P |S_{VV}|^2}{\sum^P |S_{HH}|^2}}$$

$$= C \times \rho_{hv}^P \times \sqrt{\frac{1}{Z_{DRI}^P}}, \tag{4.23}$$

then:

$$\rho_{hv} = \frac{1 + C \times \rho_{hv}^P \times \sqrt{\frac{1}{Z_{DRI}^P}}}{\sqrt{\left(1 + \frac{Z_H^P}{Z_H^A}\right)\left(\frac{Z_H^P}{Z_H^A} + \frac{Z_H^P}{Z_H^A}\right)}} \tag{4.24}$$

where ρ_{hv}^P is the co-polar correlation coefficient that would result from the mixture of pristine crystals in the absence of any aggregates, characterising the shape diversity of the pristine crystal population. Therefore:

$$\rho_{hv} = \frac{1 + C \times \rho_{hv}^P \times \sqrt{\frac{1}{Z_{DRI}^P}}}{\sqrt{(1 + C) \times \left(1 + \frac{C}{Z_{DRI}^P}\right)}} \tag{4.25}$$

Note that this equation can be readily modified to include the effect of a background

Z^{A}_{DRI}:

$$\rho_{hv} = \frac{\frac{1}{\sqrt{Z^{A}_{DRI}}} + C \times \rho^{P}_{hv} \times \sqrt{\frac{1}{Z^{P}_{DRI}}}}{\sqrt{(1+C) \times \left(\frac{1}{Z^{A}_{DRI}} + \frac{C}{Z^{P}_{DRI}}\right)}} \tag{4.26}$$

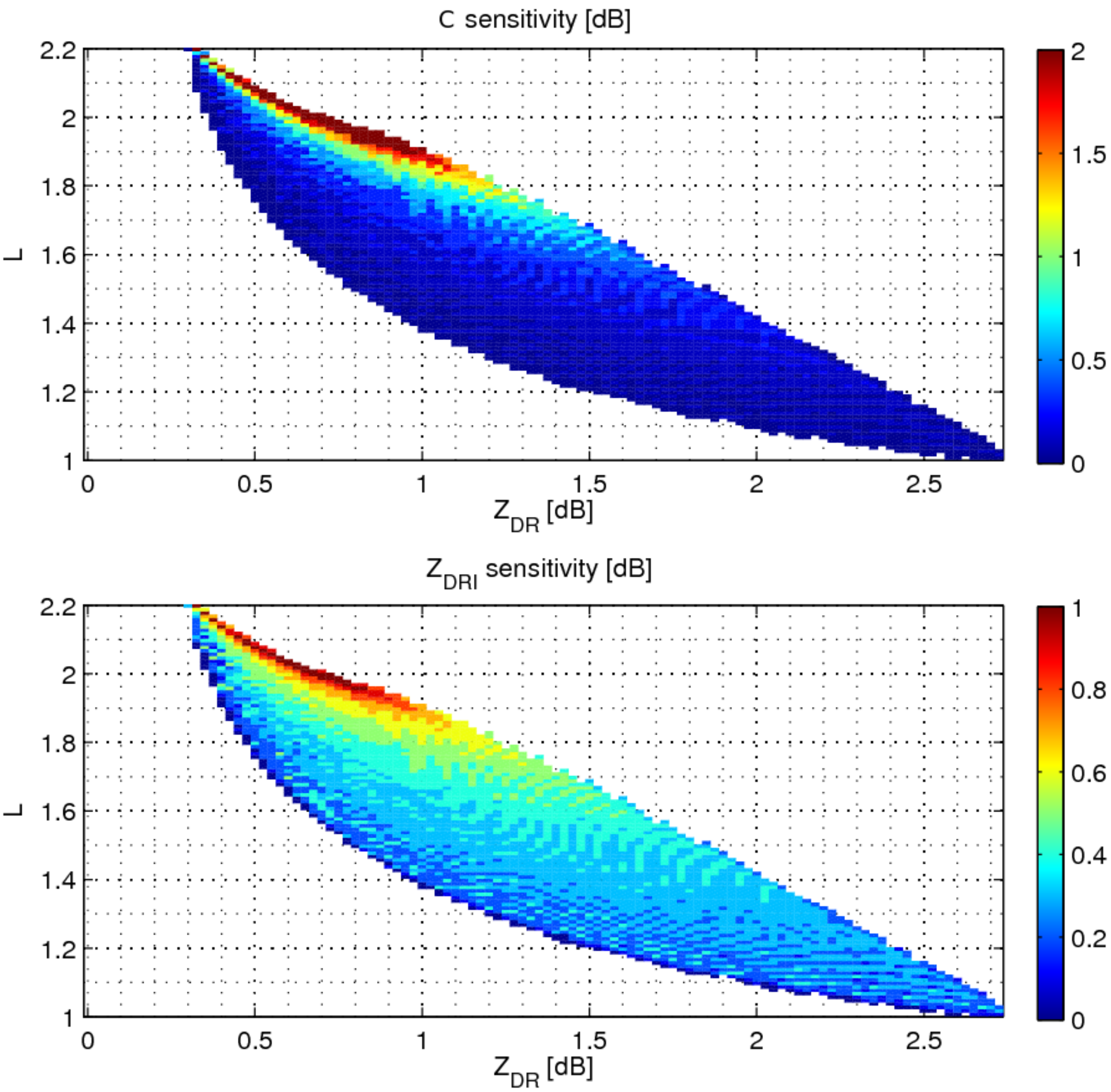

Figure 4.8 The sensitivity of retrieved C and Z^{P}_{DRI} to assuming a uniform Z^{P}_{DRI} distribution width of 1 dB compared to assuming a fixed aspect ratio.

4.3.6 Sensitivity to fixed aspect ratio assumption

To test the sensitivity of the retrieval to the assumption of a fixed aspect ratio, the same method as that used to test the sensitivity to the assumption of Z_{DRI}^{A} was applied. L and Z_{DR} were forward modelled as before, but for each Z_{DRI}^{P} value, a uniform distribution of Z_{DRI}^{P} with a width of 1 dB was assumed. Sensitivity was defined as the absolute difference in retrieved C and Z_{DRI}^{P} values for a pair of L and Z_{DR} observations. Figure 4.8 shows the sensitivity of C (top) and Z_{DRI} (bottom) to assuming a uniform 1 dB distribution width compared to a fixed aspect ratio.

It can clearly be seen that both retrieved quantities are much less sensitive to the assumption of a fixed aspect ratio compared to the assumption of background Z_{DR} of the aggregate crystals. The greatest sensitivity in both C and Z_{DRI}^{P} again occurs when the polarimetric signal is relatively weak (L greater 1.8 and Z_{DR} smaller than 1 dB). There is pronounced sensitivity to a distribution of pristine oriented crystal shapes for higher L (which corresponds to smaller predicted Z_{DRI}^{P} values). This is because the contribution to the reduction of L caused by pristine oriented crystal aspect ratio variability (ρ_{hv}^{P} in equation 4.24) is larger when the Z_{DRI}^{P} distribution width is comparable in magnitude to the mean Z_{DRI}^{P} value. Again, the retrieved C is most sensitive to the assumption. For high L and low Z_{DR}, it is as large as 2 dB, but, for the majority of L and Z_{DR} values the sensitivity is lower than 0.5 dB. Z_{DRI}^{P} is less sensitive overall, and broadly less than 0.5 dB. The retrieval can therefore be considered insensitive to pristine crystal shape variability, apart from when the polarimetric signature is very weak.

4.4 Case study II: 17 February 2016

On February 17 2016, an occluded front stalled over the UK, producing precipitation over Chilbolton that lasted over 12 hours. In addition to collecting radar data of the deep ice cloud on this day, the FAAM aircraft also made in-situ measurements at various altitudes between 1200 and 1400 UTC. Furthermore, Doppler spectra were also measured from the vertically pointing Copernicus 35 GHz Doppler radar.

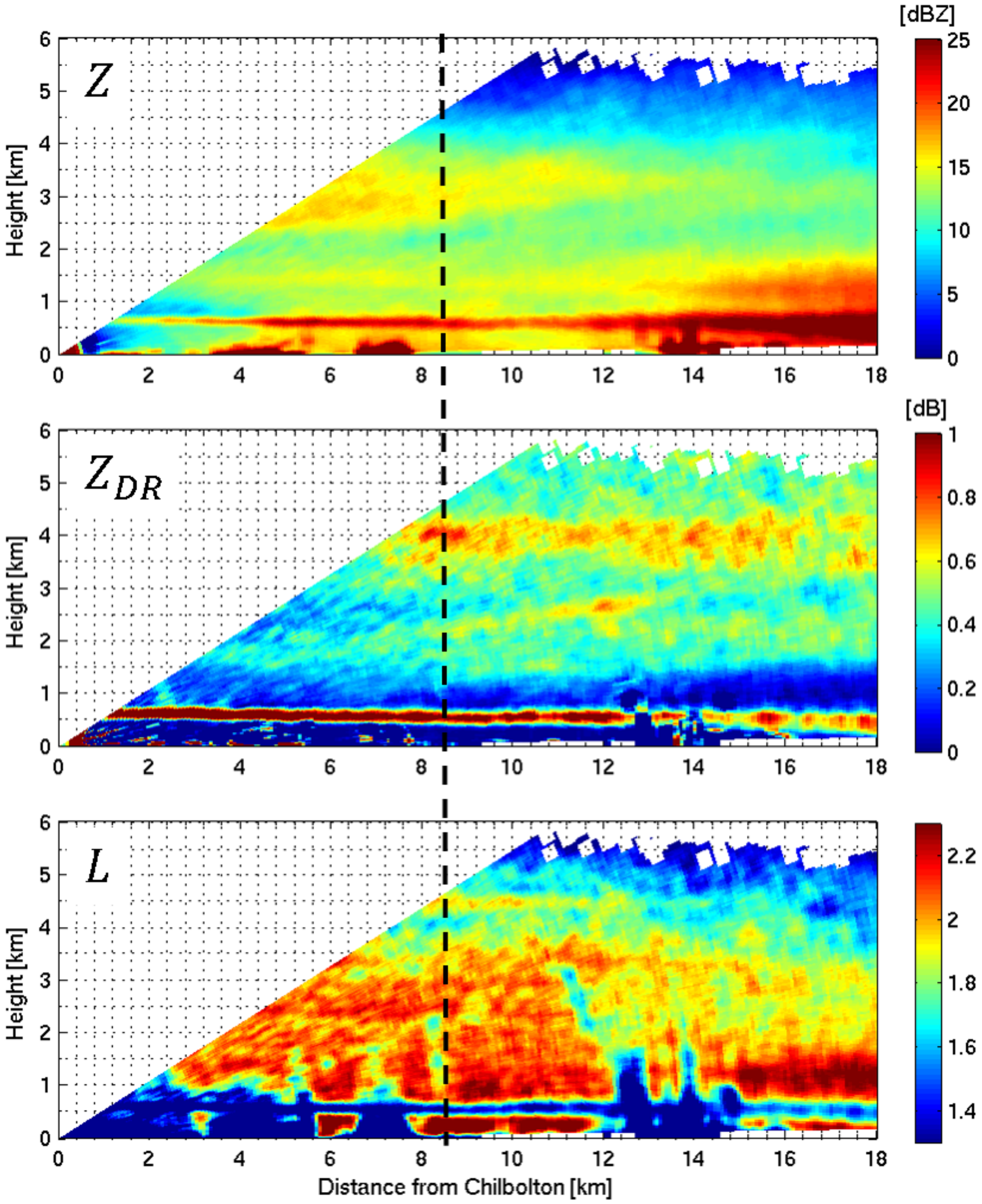

Figure 4.9 RHI scans of Z, Z_{DR}. and L at 1156 UTC on 17 February 2016. Data has been averaged to 1° and 300 m in range, and is only shown for SNR > 10 dB.

Figure 4.9 shows the observed Z, Z_{DR} and L for an example RHI scan taken at 1156 UTC. The melting layer can again be clearly identified by the enhanced Z, Z_{DR} and decreased L at approximately 500 m in height. A similar polarimetric signature is seen above the melting layer at approximately the same height (4 km) as in case

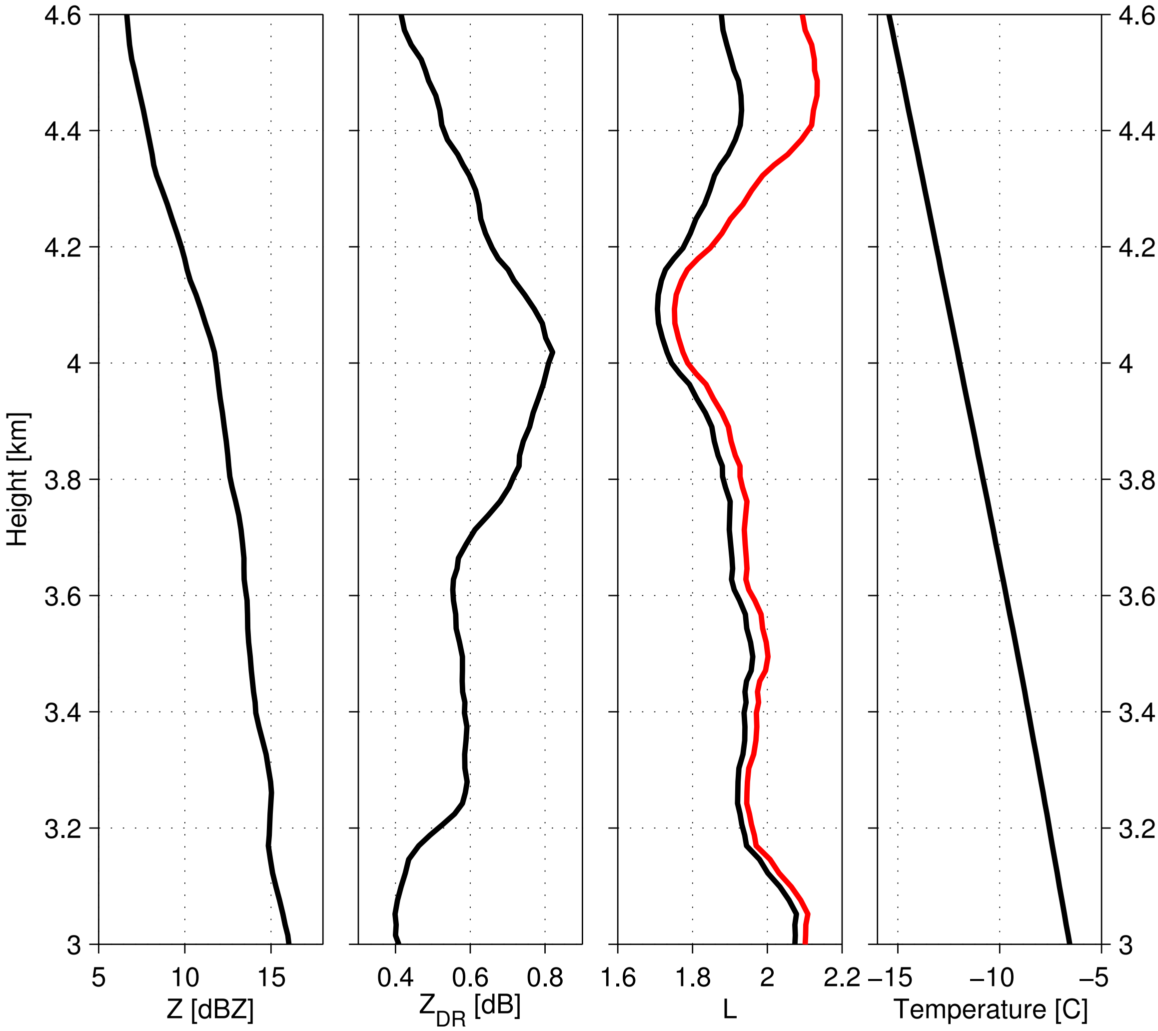

Figure 4.10 Vertical profiles of Z, Z_{DR}, L and temperature at 8.5 km in range at 1156 UTC on 17 Feb 2016 (indicated by dashed black line on figure 4.9). The red line is L adjusted for SNR effects.

study I, however the increase in Z and Z_{DR} and reduction in L are weaker in this case study. Peak Z_{DR} reaches approximately 1 dB, and minimum L is approximately 1.7. L is lower towards the cloud top than in case study I, as the SNR is lower. Evidence of further pristine ice crystal growth is indicated by enhanced Z_{DR} between 2 and 3 km. There is also a corresponding increase in Z at this level. Unfortunately, the strength of this secondary signature is insufficient for a reliable retrieval. It is also interesting to note that, from vertically pointing radar earlier on this day that at this temperature there appeared to be a layer of ice production; this also features in the January 31 2014 case study.

Figure 4.10 shows the observed profiles of Z, Z_{DR}, observed and "effective" L and temperature imported from the operational ECMWF model, at a range of 8.5 km from Chilbolton (black dashed line in figure 4.9). The interpretation of these profiles is broadly similar to that of case study I. At 4.6 km, the temperature is approximately -15°C; Z is approximately 7 dBZ, whilst Z_{DR} is approximately 0.4 dB and L is high at approximately 1.9; this is consistent with a monodisperse population of small, irregular polycrystals or aggregates. Below, L decreases to approximately 1.7 at 4.1 km, whilst Z_{DR} increases to a peak of 0.8 dB at 4 km; again the minima in L appears to be slightly higher in altitude than the peak in Z_{DR}. Below 4 km, Z_{DR} decreases, whilst L increases, indicative of aggregation as the reflectivity-weighted shape is becoming more spherical whilst the crystal shapes are becoming more monodisperse. Sharp gradients in Z_{DR} and L at 3.2 km (-7°C) and a corresponding increase in Z seem to suggest rapid aggregation.

4.4.1 Retrieval profiles

As before, C and Z_{DRI}^{P} are retrieved using look-up tables based on equations 4.13 and 4.5 (including a background Z_{DR} of 0.3 dB and assuming a fixed aspect ratio). The results are shown in figure 4.11. At a height of 4.4 km, C is approximately -7 dB. After decreasing slightly, it gradually increases until a maxima of -6 dB is reached at a height of 3.9 km. Meanwhile, Z_{DRI}^{P}, which is initially 2 dB, gradually increases to its maxima of approximately 5 dB at 4.1 km, approximately 200 m higher than the peak in C. From there, Z_{DRI} continually decreases to approximately 3 dB at the location of maximum C (3.9 km), where it remains down to 3.2 km (other than a small peak at 3.6 km).

The retrieval results are broadly similar to those of the first case study. Physically, the dominant characteristics of these profiles can be explained by plate-like crystals nucleating at approximately -15°C, and growing by vapour deposition. The decrease in Z_{DRI}^{P} whilst C increases or remains constant suggests that the crystals are growing extensions or branches, which are reducing their effective density. At 4.1 km (above the peak C), the effective density is estimated to be 0.85 gcm^{-3}. This decreases to

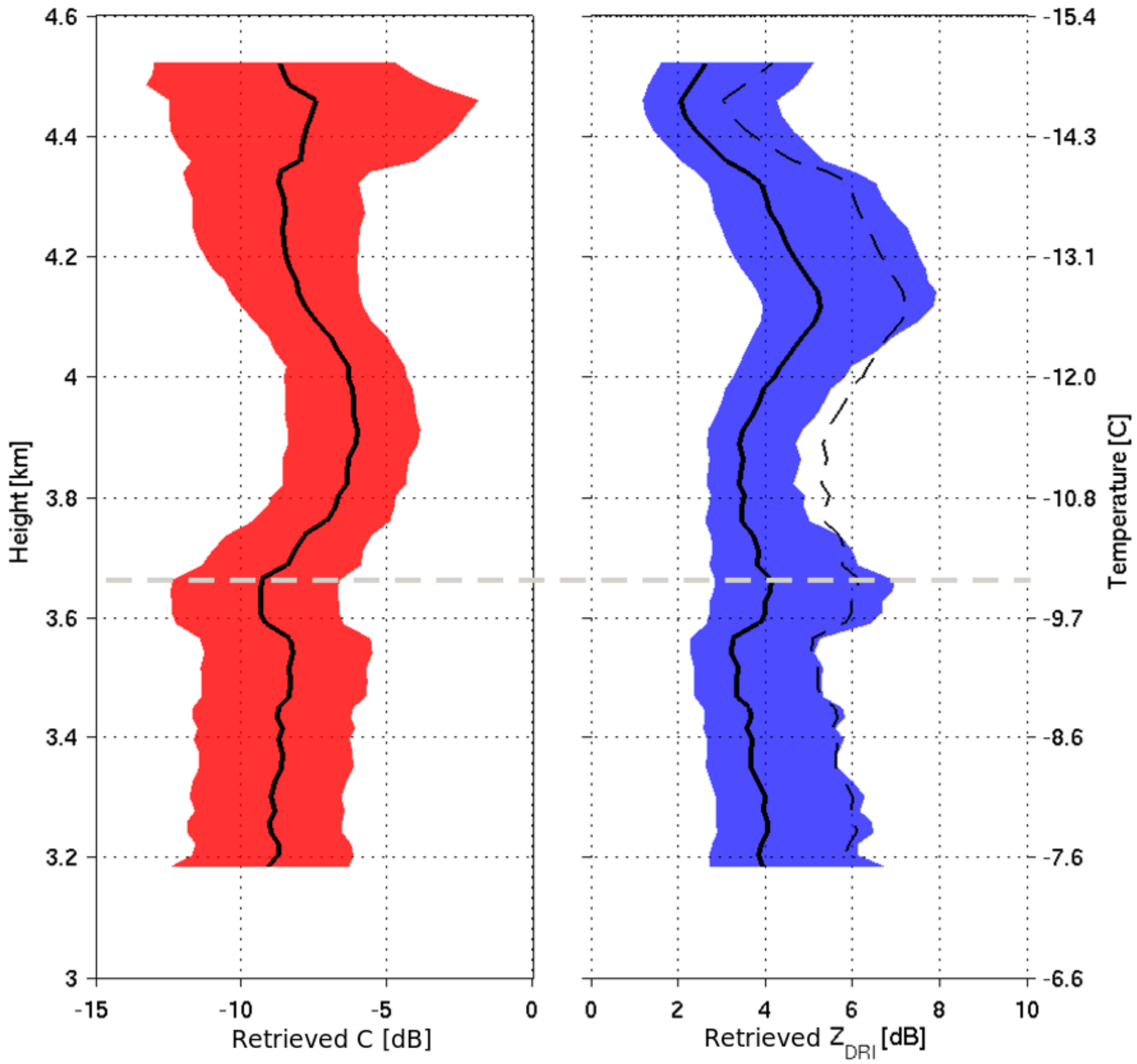

Figure 4.11 Retrieved C and Z_{DRI}^{P} as a function of height and temperature at 8.5 km from Chilbolton on 17 February 2016. The dashed black line is the "true" Z_{DRI}^{P} that would be observed at an elevation angle of 0°. The grey dashed line corresponds to an aircraft flight, made at a height of 3650 m.

approximately 0.64 gcm^{-3} at 3.8 km, just below the height of peak C.

4.4.2 Coincident Doppler spectra

Further to the polarimetric information from CAMRa, the 35 GHz Copernicus Doppler radar was operating at vertical measuring Doppler velocity spectra on this day. Doppler spectra provide an insight into the distribution of backscattered power from hydrometeors as a function of their Doppler velocity. This is a powerful tool for the study of microphysical processes; the fall speeds of hydrometeors are linked to their microphysics and the processes that formed them. The Doppler velocities are reflectivity-weighted, and so dominated by contributions from the largest hydrometeors. Figure 4.12 shows an example Doppler spectra from 1238 UTC. Power [dB] is displayed as a function of the observed Doppler velocity [ms^{-1}] integrated over 10 s for height bins of 30 m. At 7.5 km in height, a single peak in backscattered power is measured. The corresponding Doppler velocities are measured to be 0.5 — 0.6 ms^{-1}. This indicates that hydrometeors producing this backscatter are relatively small, and are all falling at approximately the same speed. At approximately 5.5 km, both magnitude of the backscattered powers and width of the power spectra increase, indicating that there is an increase in the number and/or size of the ice particles, and a greater spread in their fall speeds. The peak power corresponds to fall speeds of approximately 1 ms^{-1}. In general, this trend of increasing power and associated Doppler velocity increase continues as the ice crystals grow larger by aggregation, until their mean fall speeds reach 1.3 ms^{-1} at approximately 3 km. The fluctuation in the power spectra at approximately 1.5 km is likely to be the result of strong turbulence; observed Doppler velocities also contain contributions from ambient air motions within the cloud.

Of particular interest in this Doppler spectra is a feature between 3.5 and 4.5 km (indicated by the box in figure 4.12). At this height, the power spectra is bi-modal; there are two peaks in power at two different Doppler velocities. This separation suggest that at this height there are two distinct ice populations, one falling very slowly (at approximately 0.1 ms^{-1} and the other more quickly, at approximately 0.8 ms^{-1}. This occurs at the same height as the enhanced polarimetric signatures observed by CAMRa (figure 4.9), supporting the interpretation of the retrieval; pristine oriented crystals are growing rapidly at these heights by vapour deposition. Their consequent growth by vapour deposition (increase in mass) is illustrated by the gradual increase in the power and the Doppler velocity down to a height 3.5 km; below which the crystals have become large enough and/or have aggregated so that their fall speeds are comparable to the "background" ice particles, and the spectrum once again becomes monomodal. However, there is evidence of slight bi-modality even down to 2.5 km, which would be consistent with elevated Z_{DR} signature shown by CAMRa. Further bi-modality in the Doppler spectra can be observed between 1.5 and 2.5 km in height. It is unclear whether this is the result of fresh pristine growth from another SLW layer, or whether it could perhaps be the result of secondary ice production at these warmer temperatures (Hallett and Mossop, 1974).

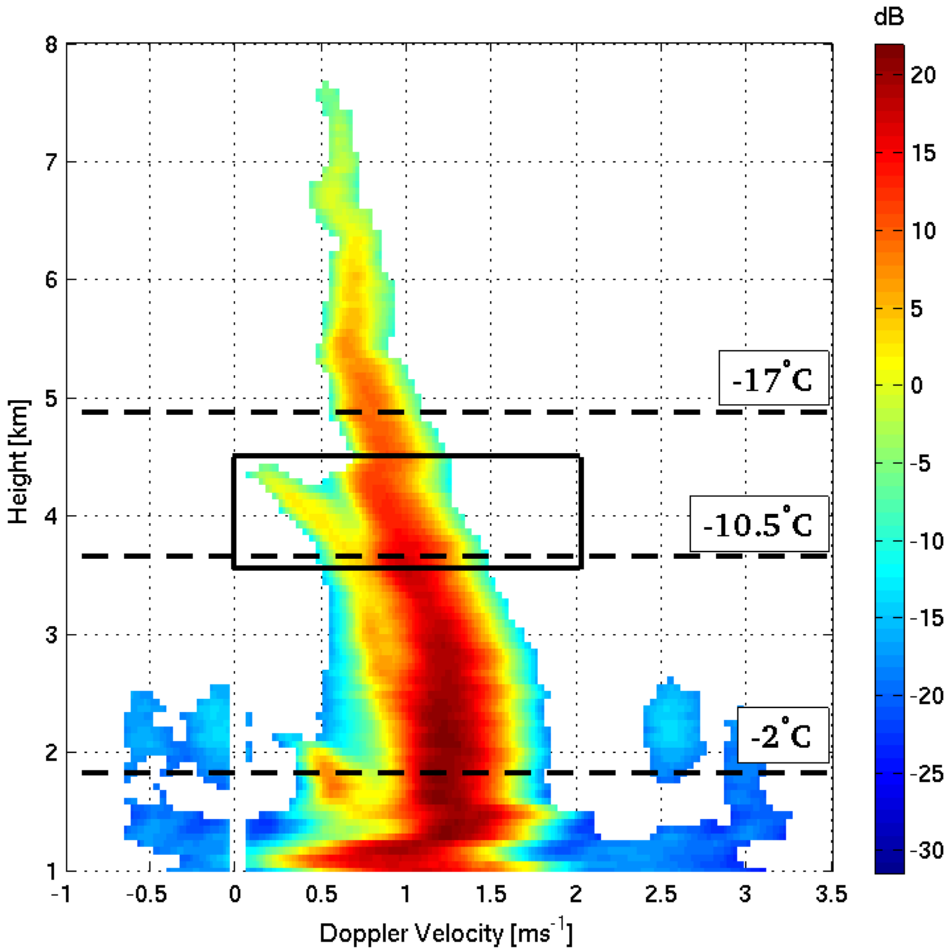

Figure 4.12 Doppler spectra from the 35 GHz radar at 1238 UTC on Feb 17th 2016. The box indicates the primary signature of interest. The dashed lines correspond to the flight altitudes of the FAAM aircraft.

The strong bi-modality of the spectra between 3.5 and 4.5 km in height provide an opportunity to independently estimate the contribution of the slower falling pristine crystals to the radar reflectivity, for comparison with that from the newly developed retrieval technique. Estimates of the radar reflectivity from each crystal type can be made by integrating the power spectrum over the range of velocities from each of the crystal types. This analysis requires that power contributions from each particle type are able to be separated by a given velocity threshold. An adaptive velocity threshold (ranging from 0.4 ms^{-1} at 4.3 km to 0.8 ms^{-1} at 3.4 km) was used to ensure that the power backscattered from increasingly faster falling pristine oriented crystals remained separated from the aggregates and polycrystals. Figure 4.13 (a) to (c) show the observed power spectrum (and 11^{th} order polynomial fits) at heights of 4.3, 4.1 and 3.8 km respectively. At 4.3 km, not long after the ice crystals have been nucleated, there is a very clear bi-modal power spectrum. By 4.1 km, the pristine oriented crystals have grown larger, but their peak is still clearly distinguishable from the aggregates. By 3.8 km, the pristine crystals are almost falling at the same rate, leading to an almost monomodal distribution. Figure 4.13 (d) shows C as a function of height estimated using this Doppler spectral method. Qualitatively, C estimated with this method behaves very similarly to C retrieved using the polarimetric retrieval. The broad maxima in C is reproduced at the correct heights. This provides evidence that the newly developed polarimetric retrieval technique is capturing the presence of these pristine oriented crystals, however the magnitude of C appears lower compared to the polarimetric retrieval. Part of this underestimation could be Copernicus, despite having a shorter wavelength, is less sensitive than CAMRa. The effect of this is that some of the smaller crystals that are being observed by CAMRa may not be seen by Copernicus, but this effect is likely to be small. Direct quantitative comparison is not meaningful however, because the profiles are not co-located in space.

4.4.3 In-situ aircraft measurements

Also on this day, the FAAM aircraft, equipped with an array of cloud microphysical probes, made a series of flight runs at several temperatures of microphysical interest. At 1338 UTC, the aircraft flew at 3650 m (-10°C) in order to sample the aforementioned bi-modal feature. At 1358 UTC, the aircraft flew at 4900 m (-17°C), in order to sample the polycrystals and aggregates above the region of pristine oriented crystal growth. The altitudes of these flights are indicated by the dashed lines on figures 4.11 and 4.12. The quasi-stationary nature of this front means that, although these measure-

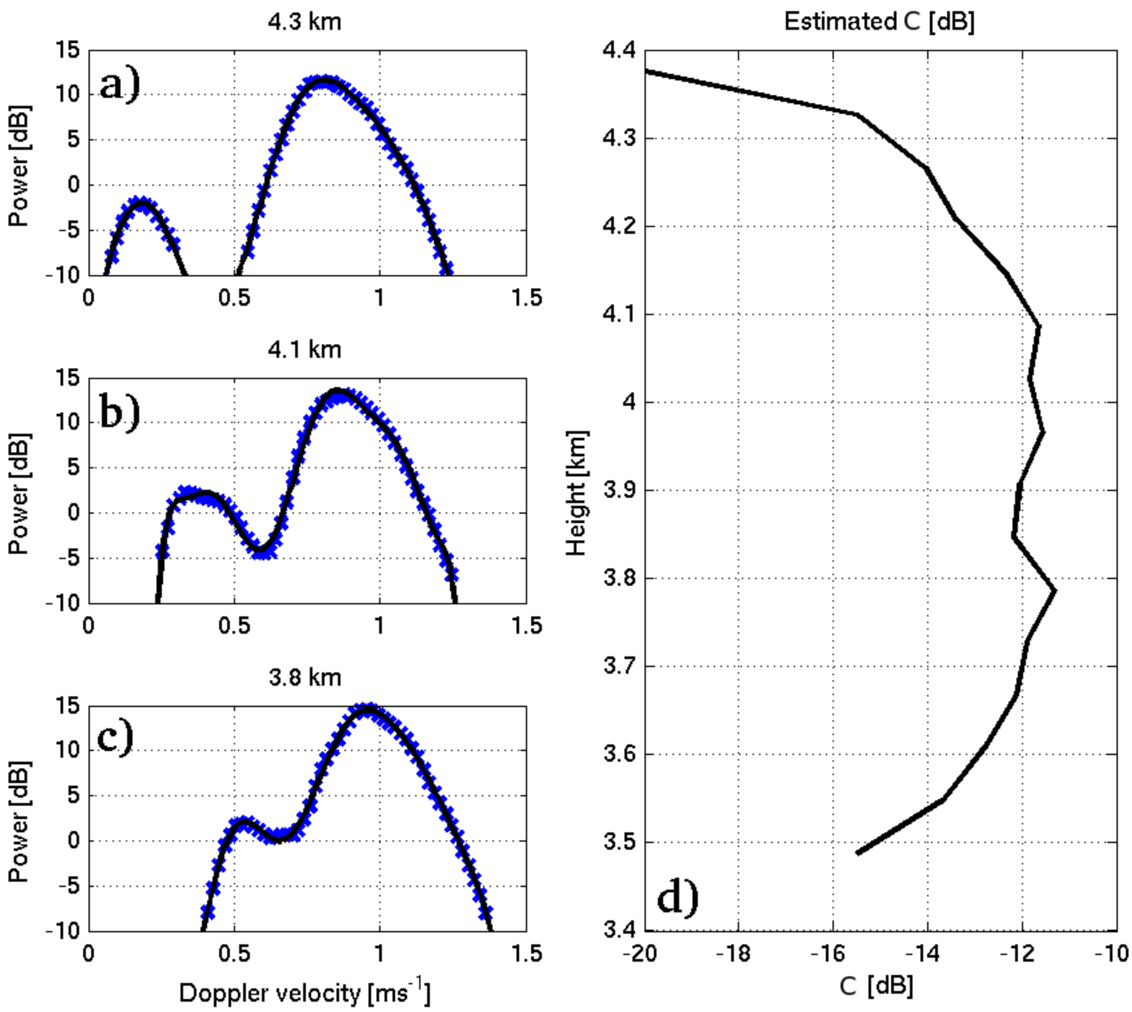

Figure 4.13 Power distributions at heights of (a) 4.3 km, (b) 4.1 km and (c) 3.8 km from the Doppler spectra in figure 4.12. (d) shows C estimated from these power spectra.

ments were separated in time, they are representative of the microphysics throughout the measurement period. Amongst the aircraft instruments were 15 μm and 100 μm resolution cloud imaging probes (CIPs): CIP-15 and CIP-100 respectively. These were fitted with anti-shatter Korolev-tips to minimise contamination of the sample area by particle shattering (Korolev *et al.*, 2011).

Figure 4.14 shows example images from the CIP-100 (left) and CIP-15 cloud imaging probes (right) at 1357 UTC during the 4900 m (-17°C) flight run. Each box is 1 s sample; in total, 13 s worth of data from each probe is shown. It is clear from the CIP-100 image that the ice crystals present at this temperature are highly irregular

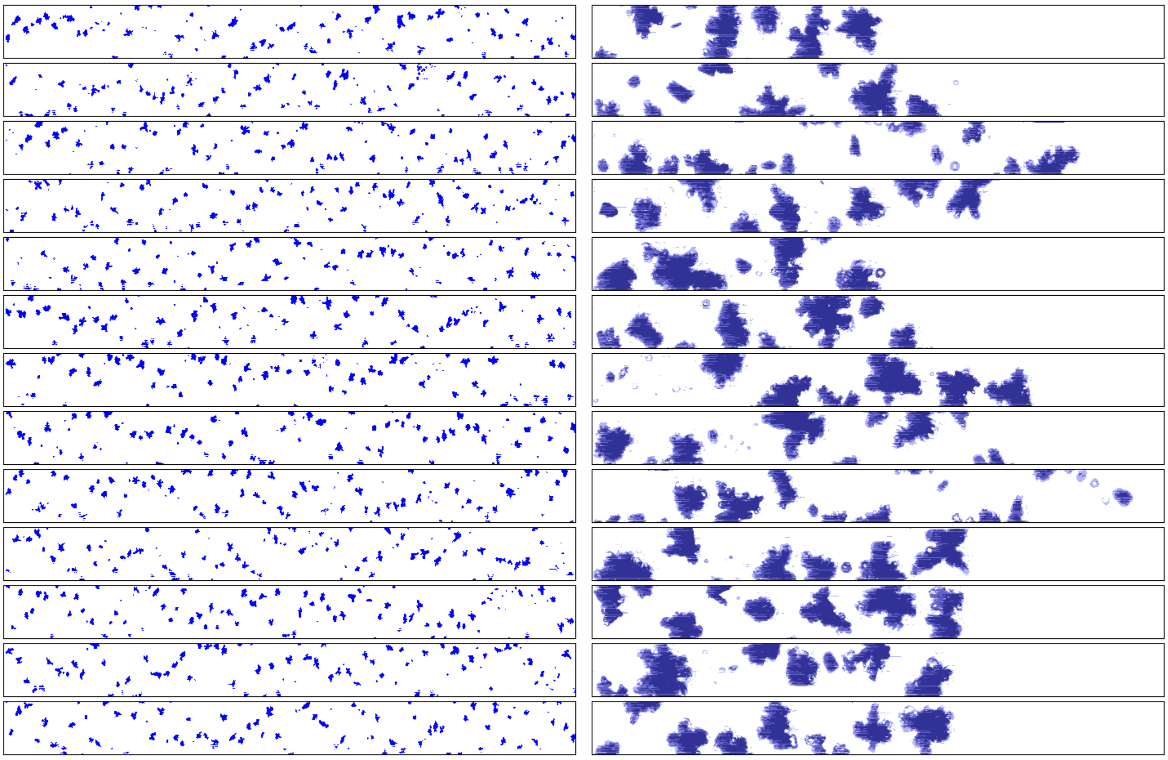

Figure 4.14 Example 1 s CIP-100 (left) and CIP-15 (right) images from the 4900 m (-17.5°C) flight run at 1357 UTC. The image widths are 6400 and 960 microns respectively.

polycrystals and aggregates, with typical major dimensions of 1 mm, with occasional crystals as large as 2 mm. This is confirmed from the CIP-15 image; the higher resolution of this image reveals the highly irregular nature of these crystals. Comparison of these images with figure 1.4 indicates that these crystals were likely nucleated at temperatures below -20°C (Bailey and Hallett, 2009), and have fallen to the warmer temperatures in which they are now observed.

Figure 4.15 shows CIP-100 and CIP-15 images from the 3650 m (-10.5°C) flight level. The CIP-100 image shows that the particles are predominantly irregular and typically larger at this temperature; large polycrystals and some aggregate crystals can be identified. This is consistent with the increase in backscattered power and gradual increase in fall speeds observed in the Doppler spectra. The CIP-15 images reveal that amongst these crystals, plate-like pristine crystals with extensions (Magono *et al.*, 1966) are present. The apparent random orientation of these crystals is due to local accelerations as they were drawn into the probe (Gayet *et al.*, 1993). Labo-

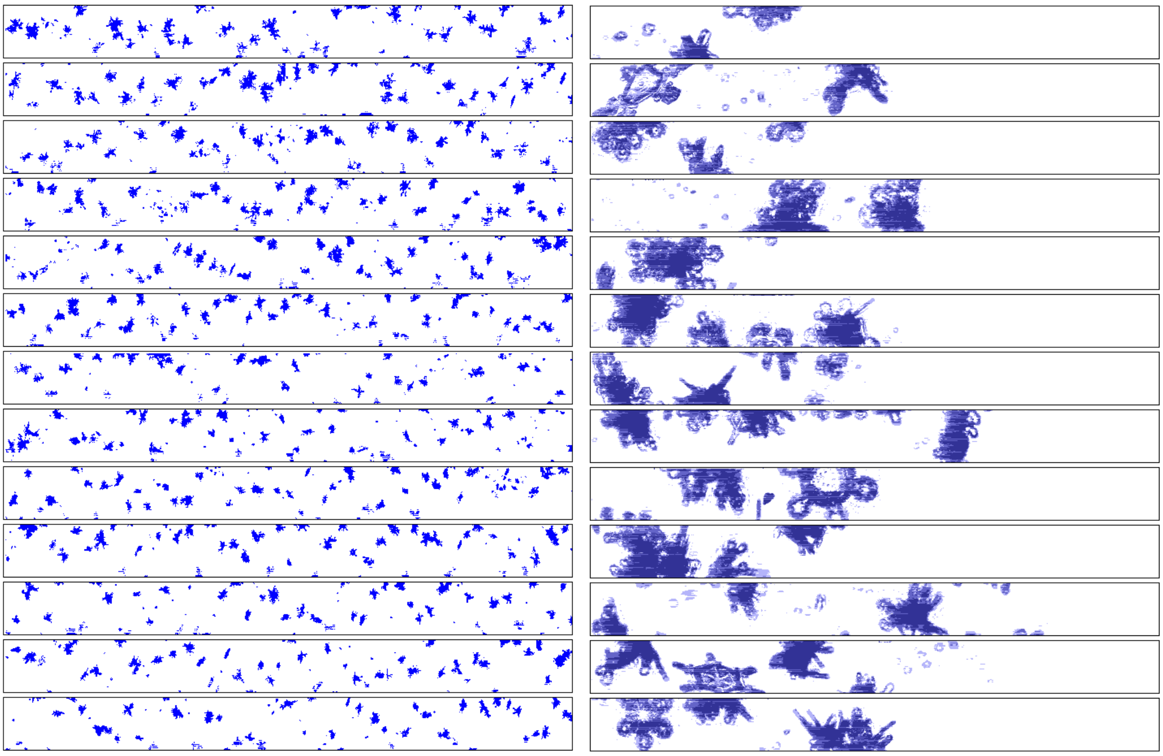

Figure 4.15 Example 1 s CIP-100 (left) and CIP-15 (right) images from the 3650 m (-10°C) flight run at 1338 UTC. The image widths are 6400 and 960 microns respectively.

ratory experiments show that such structures tend to form when plate crystals grow preferentially at the corners in highly saturated environments, typically between -13.5 and -14.5°C (Takahashi *et al.*, 1991; Takahashi, 2014). This is consistent with the conceptual model and retrieval results.

4.5 Discussion

The retrieval profiles for both case studies have broadly similar characteristics. Additional information provided by aircraft imaging probes and Doppler spectra during the February 17 case study support the conceptual model used to develop the polarimetric retrieval technique. Pristine oriented crystals were observed amongst polycrystals and pseudo-spherical aggregates in cloud imaging probes at approximately -10.5°C, corresponding to bi-modal spectra that indicate a slower falling ice crystal population amongst a larger, faster falling crystals at the same height. C estimated by integrating the power spectrum over the expected velocity ranges for each crystal population is qualitatively similar to that retrieved using the polarimetric method, and the retrieved Z_{DRI}^{P} values are consistent with laboratory experiments of ice crystal growth (Takahashi *et al.*, 1991; Takahashi, 2014). The fall speed estimates of these crystals retrieved with the DDV are also consistent with laboratory results (Locatelli and Hobbs, 1974).

The lack of quantitative agreement between Doppler spectra and polarimetric estimates of C in case study II could simply be because the profiles are not co-located in space, although the quasi-stationary nature of the front on 17 February should mean that the profiles are qualitatively comparable. It is interesting to note that systematically larger C estimates from the polarimetric technique would occur if the Z_{DRI} of the aggregates is assumed to be too low. Particularly in case study II, where the polarimetric signatures are relatively weak, all but the strongest $L - Z_{DR}$ measurements are located in the part of the forward model most sensitive to this assumption (figure 4.7). The basis of this assumption is from Z_{DR} observations of aggregates just above the melting layer (which are approximately 0.3 dB in figures 4.2 and 4.9). Without corresponding in-situ measurements, it is difficult to constrain the background ice particle shape directly using the observed Z_{DR} above the embedded mixed-phase growth, as the state of aggregation of pristine crystals is not known. However, there is observational evidence that the background Z_{DR} above the embedded mixed-phase regions of interest is larger than the Z_{DR} of the aggregates which were used to make the assumption of Z_{DRI}^{A} used in this retrieval. This is supported by observations of Z_{DR} greater than 0.3 dB corresponding to the mono-disperse population of irregular polycrystals seen in the CIP-15 and CIP-100 images on 17 February. A general increase in Z_{DR} with height is also evident from the median Z_{DR} profile from the 3 month 35 GHz campaign (chapter 2, figure 2.4).

The pristine oriented crystal and aggregate fall speed retrieval is relatively insensitive to this Z_{DRI}^{A} assumption. However, as well as an overestimate of C, an underestimated Z_{DRI}^{A} would also lead to an underestimate in retrieved Z_{DRI}^{P} and therefore estimates of effective densities. Clearly, successful interpretation of the retrieval presented in this chapter relies upon an accurate characterisation of Z_{DRI}^{A} profile, and so this warrants further investigation.

4.6 Summary

A novel polarimetric technique has been developed that reveals the radar signal from pristine oriented crystals that is otherwise masked by the presence of polycrystals or large aggregates. By utilising measurements of L and Z_{DR} from the 3 GHz Chilbolton Advanced Meteorological radar, retrievals of both the intrinsic Z_{DR} of pristine crystals (Z_{DRI}^{P}) and their relative contribution to radar reflectivity (C) in embedded mixed-phase clouds is presented in two case studies. In the second case study, coincident in-situ measurements were also collected by the FAAM aircraft at microphysically significant heights. Images from cloud imaging probes are consistent with the conceptual model and the retrieval results. The retrieval profiles show that enhancements of Z_{DR} embedded within deep ice are typically produced by pristine oriented crystals with large Z_{DRI} values (4—7 dB), but with varying contributions to the radar reflectivity. The effective densities of the retrieved pristine crystals were estimated from the retrieved Z_{DRI}^{P}, and were consistent with the CIP-15 and CIP-100 images and laboratory estimates of ice crystal density. In the first case study, a technique using differential Doppler velocity measurements to estimate the difference in fall speeds between the pristine crystals and aggregates was demonstrated. Knowledge of the observed vertical velocity from the Copernicus 35 GHz Doppler radar then allowed the individual fall speeds of each ice crystal type to be estimated. The results were consistent with large pristine crystals, or smaller but lightly rimed crystals.

Bi-modal Doppler spectra were also measured by the Copernicus radar for the second case study, further supporting the retrieval concept and results. Furthermore, this provided the opportunity to separate ice crystal types according to their fall velocity and estimate C independently, which was found to be qualitatively similar to C estimates, but several dB lower than that using the new polarimetric retrieval. The retrieval was shown to be sensitive to the specification of aggregate shape, which was based on the Z_{DR} measurement just above the melting layer where it is known that large pseudo-spherical aggregates dominate Z_{DR} and because it is difficult to measure directly above the embedded mixed-phase region. Aircraft data and Z_{DR} measurements (as well as observational evidence from Z_{DR} profiles in chapter 2) suggest that Z_{DRI}^{A} may increase as a function of height. This would be consistent with overestimating of C with the polarimetric technique, although strictly a quantitative comparison is not possible since the profiles are not co-located in space. Since the retrieval is sensitive to this specification, it would be interesting to investigate this in future work.

There is also the potential for further microphysical information to be gained from this retrieval. It would be interesting to incorporate other polarimetric measurements into the analysis, such as K_{DP}, which is only sensitive to the number and shape of aligned particles. Combined with retrieved Z_{DRI}^{P}, this could be used to estimate ice water contents of the pristine crystals using a method similar to Ryzhkov and Zrnic (1998). Furthermore, gradients in retrieved radar reflectivities with height could allow estimation of the growth rates of pristine crystals and aggregates. More case studies with stronger polarimetric signatures would be useful to fully exploit this new retrieval technique to further investigate the microphysical properties and processes in deep stratiform ice clouds.

Chapter 5

Rain drop size distribution retrieval

5.1 Motivation

Knowledge of the drop size distribution (DSD) is important for radar derived estimates of rain rate. Dual polarisation radar allows information about drop shapes to be estimated. However, even with knowledge of median drop diameter (D_0), uncertainty in the shape parameter (μ) in the gamma drop size distribution can still cause large errors in retrieved rain rate. Figure 1.8 shows rain rate per unit radar reflectivity as a function of Z_{DR} for various μ values; rain rate can vary by almost a factor of 2 for a given pair of Z and Z_{DR} observations as a result of uncertainty in μ. Disdrometer instruments suffer from poor sampling of small and large drops, and so calculating μ from moments of the DSD can lead to estimates being biased high (Johnson *et al.*, 2014). Therefore, estimating DSD parameters using a radar is preferable due to the very large number of drops being sampled. There have been a number of attempts to estimate μ with radar. Wilson *et al.* (1997) made radar observations dwelling in rain at elevation angles above 20° and report that DDV provides an estimate of μ, which were in the range of 1 to 11, and, once Z_{DR} exceeded 0.5 dB, all the values were above 4. Doppler spectra of rain at vertical incidence with multiple wavelength radars, including wind profiler frequencies that respond to the clear air motion have been utilised to estimate μ (Williams, 2002; Schafer *et al.*, 2002). These experiments find μ ranges between 0 and 18, but is typically 0—6. Unal (2015) fits observed Doppler spectra to theoretical drop spectra at S-band, and retrieves μ in the range of -1—5. The disadvantage of these techniques is that they use high elevation angles; for operational monitoring of surface rainfall, measurements at low elevation angles are preferable.

Illingworth and Caylor (1991) and Thurai *et al.* (2008) inferred μ from the decrease in ρ_{hv} as Z_{DR} increases using measurements from CAMRa. The difficulty here is that any mis-matches in the H and V beams will introduce an uncorrelated noise component, so that even for perfectly spherical drizzle droplets, where the "true" ρ_{hv} is unity, the radar will always measure a value less than one (defined as f_{hv}^{max}, see section 3.4). From measurements in rain at short range, Illingworth and Caylor (1991) inferred μ values, which if corrected for f_{hv}^{max} were in the range 0—2, but even for long dwells the estimated errors in μ were quite large. Thurai *et al.* (2008) analysed ρ_{hv} measurements from an operational radar and obtained estimates of μ in the range of 1—3, however their approach relies on empirically derived relationships between ρ_{hv} and DSD widths from 2 dimensional video disdrometer (2DVD) measurements. Furthermore, the technique is only valid for intense rain (Z_{DR} greater than or equal to 2 dB and ρ_{hv} smaller than 0.98).

The aim of this chapter is to use the newly defined variable $L = -\log_{10}(1 - \rho_{hv})$, to make estimates of μ in rainfall. This is achieved by comparing measured L and Z_{DR} with predicted observations for various three-parameter gamma distributions. The possibility of using this technique to retrieve μ using operational radars is then discussed. This work has been published in the Journal of Applied Meteorology and Climatology (Keat *et al.*, 2016).

5.2 Choosing a drop shape model

The independence of (D_0, μ) and (L, Z_{DR}) on the drop number concentration means that a single L and Z_{DR} observation pair corresponds to a unique D_0 and μ value. In order to forward model L and Z_{DR} for various gamma distributions, a drop shape model must be assumed. There are numerous drop shape parameterisations in the literature; here the recent models of Thurai and Bringi (2005), Szakáll *et al.* (2008) and Brandes *et al.* (2002) are compared. Thurai and Bringi (2005) produced artificial rain drops from a bridge using a fire hose which then fell 80 m to the valley floor, where the number and mean drop axis ratio were measured with a 2D video disdrometer (2DVD,

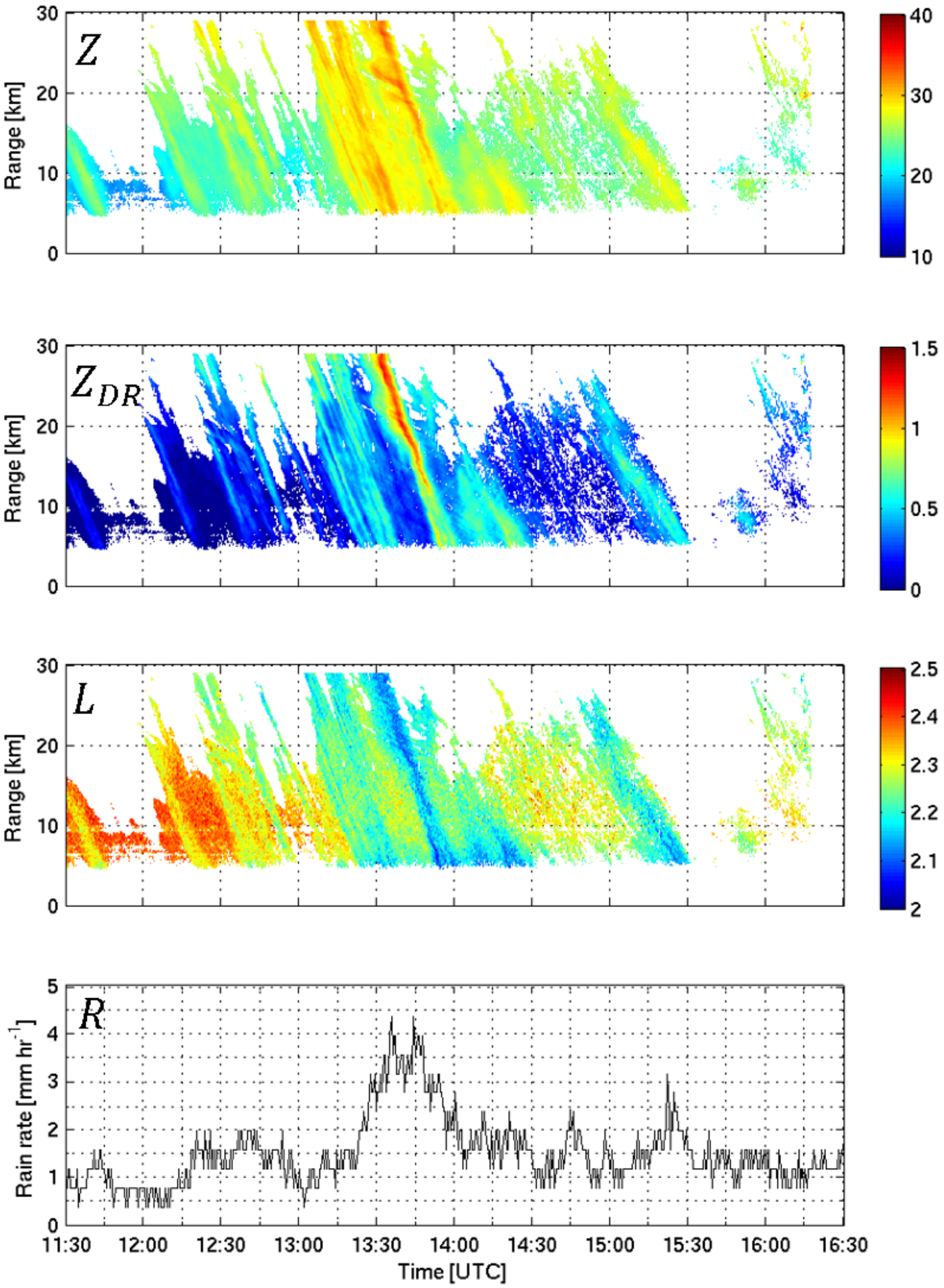

Figure 5.1 1.5° elevation dwell of Z, Z_{DR} and L from a 5 hour dwell on 25 April 2014. Also shown is rain rate from a rain gauge situated at Sparsholt, which is located at approximately 7 km in range from the radar. Data has been averaged to 300 m and 30 s.

Schönhuber *et al.*, 2008). Szakáll *et al.* (2008) made new measurements of rain drop shape for drop diameters up to 7 mm in the Mainz wind tunnel. The model of Brandes *et al.* (2002) is a 4^{th} order polynomial fit to several other laboratory experiments.

To choose the best mean drop shape model, a 5 hour dwell was made with CAMRa at a 1.5° elevation angle over a nearby Joss-Waldvogel RD-80 impact disdrometer (situated at Sparsholt, approximately 7 km away) in a frontal rain band on 25 April 2014. Figure 5.1 shows the observed Z, Z_{DR} and L, along with disdrometer calculated rain rate on this day. The disdrometer measures drop sizes in 127 size bins from 0.3 to 5.0 mm. The instrument is regularly calibrated by the manufacturer and rain rate estimated with this instrument agrees very well with that from a co-located rain gauge. Radar measurements of Z_{DR} are calibrated regularly (to within ±0.1 dB) using observations of drizzle (low Z), which is known to have a Z_{DR} value of 0 dB. The range resolution of the radar measurements is 75 m, and averaged to 30 s to match the integration time used by the disdrometer to estimate the DSD parameters. At this elevation angle, the radar was sampling rain at a height of 183 m above the disdrometer.

Figure 5.2a shows the mean axis ratio as a function of drop diameter, for each of these models. The Thurai and Bringi (2005) data suggests that mean drop shapes are slightly prolate for D smaller than 1 mm, although it is in the margin of measurement error that the drops are spherical (Beard *et al.*, 2010). Since it is known that drops become spherical as their diameter tends to 0 mm due to surface tension, the fit to the data is adapted so that drops with a diameter smaller than 1 mm are precisely spherical. Panels b—d show the observed radar measurement from the closest gate to the disdrometer and the corresponding disdrometer estimated Z_{DR} values for the Thurai and Bringi (2005), Szakáll *et al.* (2008) and Brandes *et al.* (2002) drop shape models respectively. These disdrometer Z_{DR} values are calculated using Gans theory (Gans, 1912), by assuming that rain drops can be approximated as oblate spheroids. The number and diameter of drops is measured by the disdrometer, therefore the full DSD is known. The co-polar elements of the backscattering matrix (S_{HH} and S_{VV}) can therefore be readily calculated for each drop size bin using each of the drop size-shape relationships. Z_{DR} is then calculated by integrating S_{HH} and S_{VV} over the whole DSD.

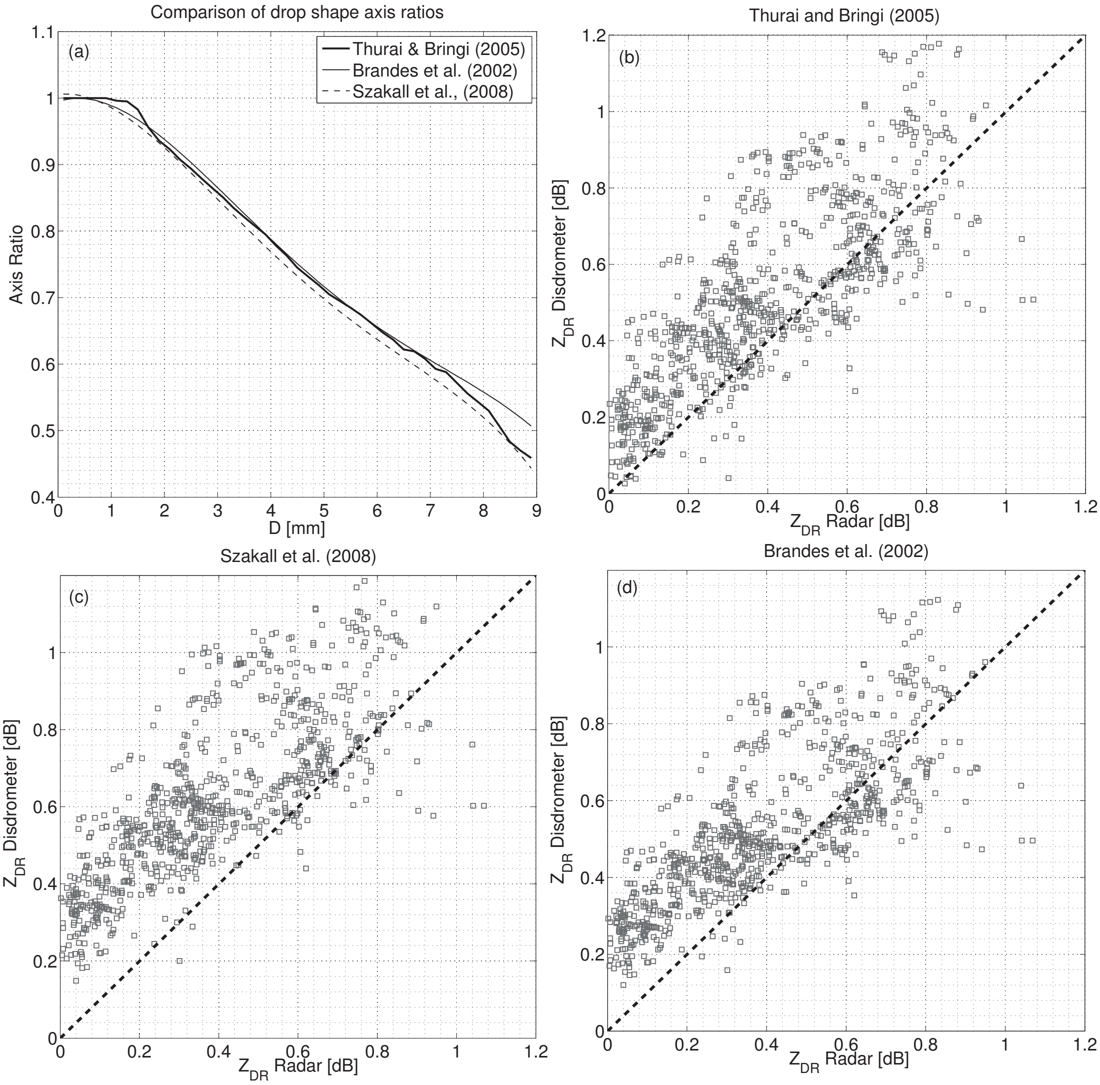

Figure 5.2 (a) Comparison of mean drop axis ratios as a function of equivalent drop diameter (D) from recent experiments of Thurai and Bringi (2005), Szakáll *et al.* (2008) and the 4$^{\text{th}}$ order polynomial fit of older experimental data constructed by Brandes *et al.* (2002). The model of Thurai and Bringi (2005) has been adapted so that drops with D smaller than 1 mm are spherical. Panels b—d show radar and disdrometer Z_{DR} comparisons calculated using Thurai and Bringi (2005), Szakáll *et al.* (2008) and Brandes *et al.* (2002) from a 5 hour dwell over a nearby Joss-Waldvogel RD-80 impact disdrometer (approximately 7 km away) in a frontal rain band on 25 April 2014. The time resolution of the radar measurements was decreased to 30 s to match the integration time of the disdrometer. At a 1.5° elevation angle, the radar was sampling rain at a height of approximately 183 m above the disdrometer. The dashed line is a 1:1 line.

Details of the computation of S_{HH} and S_{VV} for rain drops can be found in appendix B.

The Szakáll *et al.* (2008) axis ratios are systematically smaller compared to both of the other models for almost all D. Using this model makes the disdrometer estimates of Z_{DR} always larger than the radar estimates. Thurai and Bringi (2005) and Brandes *et al.* (2002) agree for D between 2 and 7 mm, after which the axis ratios of Thurai and Bringi (2005) are closer to those of Szakáll *et al.* (2008). Therefore, radar and disdrometer Z_{DR} for the Thurai and Bringi (2005) and Brandes *et al.* (2002) models largely agree, apart from $Z_{DR} \lesssim 0.4$ dB. The largest differences between these models occurs for D smaller than 2 mm. Here, Szakáll *et al.* (2008) and Brandes *et al.* (2002) predict more oblate drops than Thurai and Bringi (2005).

The Szakáll *et al.* (2008) model produces the largest radar-disdrometer overall bias of $\approx$ 0.23 dB. The biases from Brandes *et al.* (2002) for Z_{DR} bins of 0.2, 0.4 and 0.6 dB ($\pm$ 0.1 dB bin width) are 0.09, 0.16 and 0.13 dB respectively. For the Thurai and Bringi (2005) model, they are only 0.04, 0.08 and 0.09 dB respectively, and are very similar to Brandes *et al.* (2002) at higher Z_{DR}. These reduced biases at low Z_{DR} suggest that the experimental results of Thurai and Bringi (2005) best represent natural raindrop shapes; this model is chosen for this analysis. It is unclear why the very small residual difference between radar and disdrometer estimates of Z_{DR} using the Thurai and Bringi (2005) shape model is observed. Some possible explanations are that the radar calibration is slightly out causing a systematic underestimation, the small sampling volume of the disdrometer could be biasing Z_{DR}, or there could be residual error in the mean drop shape model. However, this very small difference is unimportant for retrievals that follow.

5.3 Parameterising drop oscillations

Drop oscillations increase the variety of shapes within a radar pulse volume at any given time. This means that the "true" L will be lower than that predicted by modelling only the mean drop axis ratios for drops of a given size. In order to account for this, these drop oscillations must be parameterised. The bridge experiment of Thurai and Bringi (2005) measured approximately 115000 drops, and the 80 m fall distance is

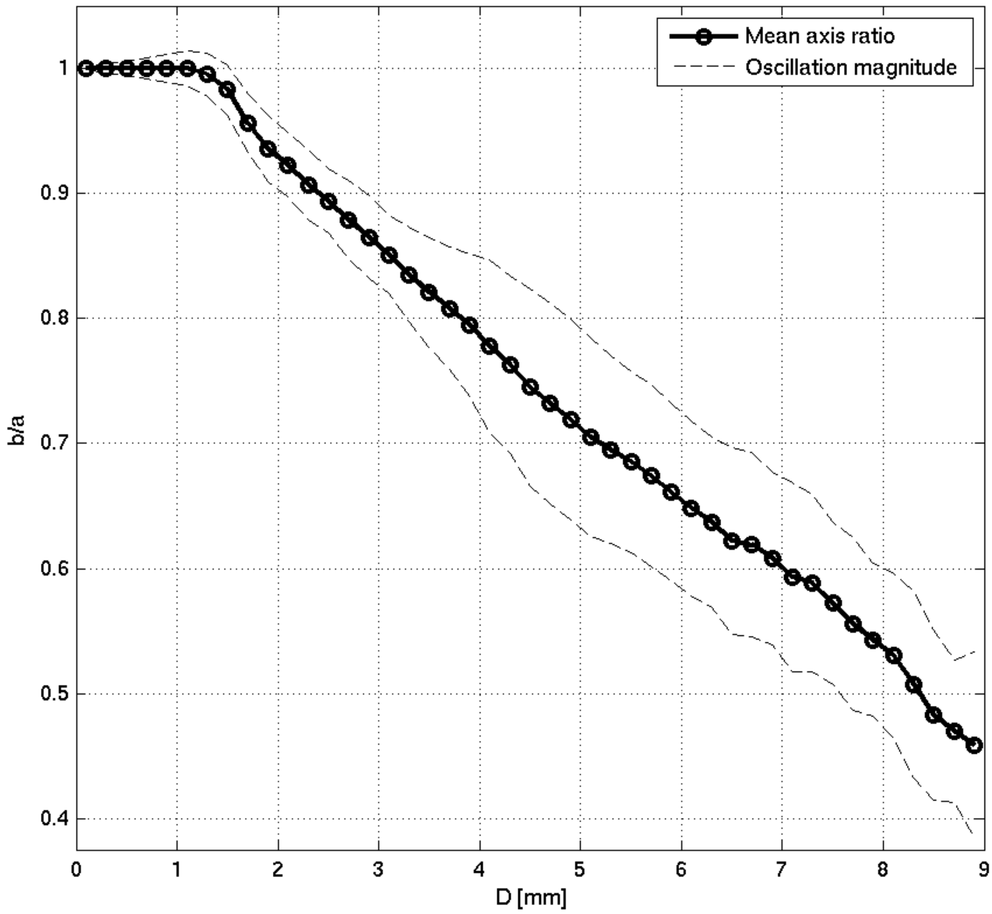

Figure 5.3 Drop axis ratio vs equivalent drop diameter (solid black line) for the chosen drop shape model. The chosen oscillation model is shown by the dashed black lines.

more than sufficient to allow the drops to achieve steady state oscillations, and so the standard deviations of axis ratios measured in this experiment are interpreted as drop oscillation amplitudes. These oscillations are therefore chosen as the model. However, the large standard deviations of the axis ratios for D greater than 2 mm are likely artificial, caused by the finite resolution of the 2DVD instrument (Beard *et al.*, 2010). Since drop oscillations are thought to originate from vortex shedding (Beard *et al.*, 2010) which increases as a function of drop size, the magnitude of oscillations should decrease eventually to zero as the drop diameter tends to 0 mm. Beard and Kubesh (1991) suggest that resonant drop oscillations occur for drop sizes between 1.1 and

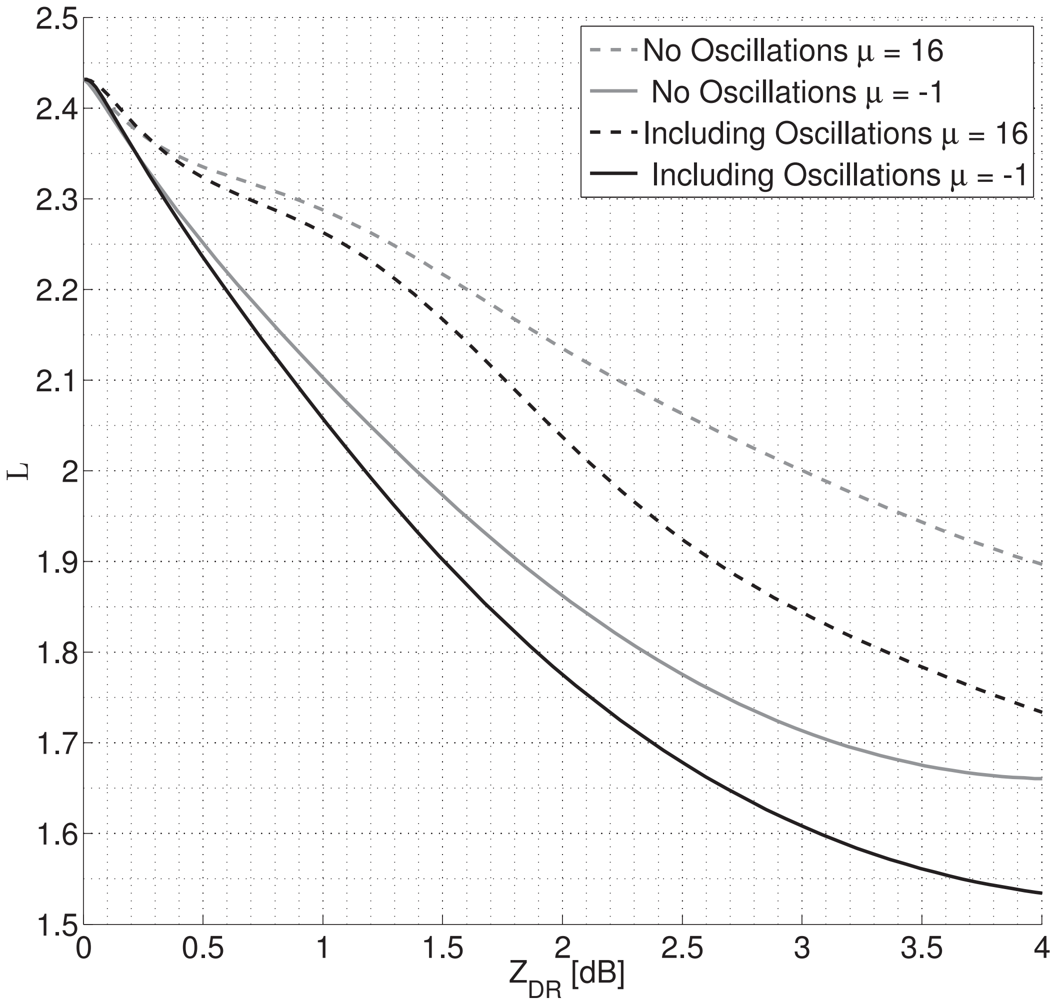

Figure 5.4 Predicted L and Z_{DR} values for gamma distributions of μ = -1 (solid) and 16 (dashed) with no oscillations (grey), and including oscillations (black). The inclusion of drop oscillations are crucial to interpretation of L and Z_{DR} measurements. The f_{hv}^{max} is assumed to be 0.9963 to match the case study in Section 5.4.

1.6 mm, however more recent measurements from the Mainz wind tunnel show that amplitudes of the axis ratios for these drop sizes were less than 0.025 (Szakáll *et al.*, 2010). For this reason, the polynomial fit to oscillation amplitude data from the Mainz wind tunnel (Szakáll *et al.*, 2010) is used for D smaller than 2 mm, which has the desired reduction in oscillation amplitude for small drops [1]. For D larger than 2 mm, the more statistically robust drop oscillations from Thurai and Bringi (2005) are used. Since the oscillations are aerodynamically induced, with an amplitude only a function

[1]Equation 1 in Szakáll *et al.* (2010) does not agree with the fit in their figure 3 (black line). By digitising the Mainz wind tunnel data, it is calculated that their equation 1 should in fact be $1.8\times10^{-3}{D_0}^2 + 1.07 \times 10^{-2}D_0$

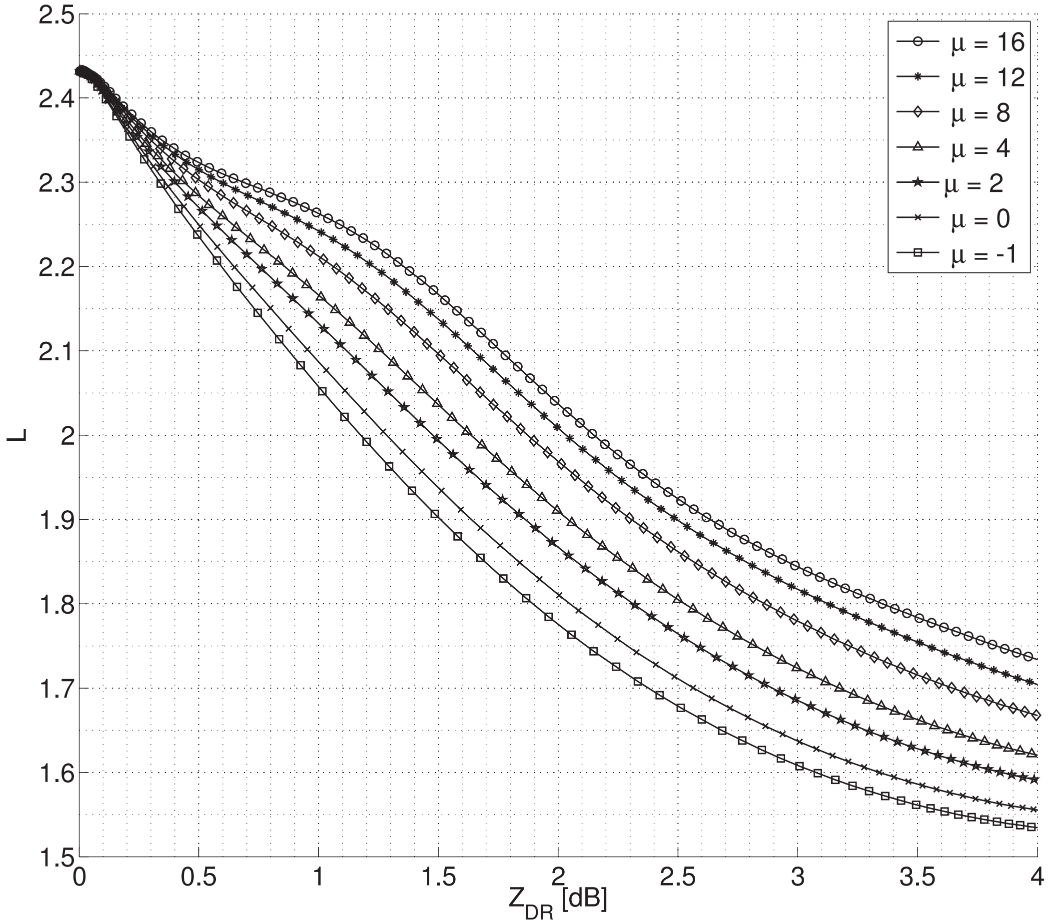

Figure 5.5 Theoretical L and Z_{DR} computed using Gans theory for gamma distributions with μ = -1, 0, 2, 4, 8, 12 and 16, using Thurai and Bringi (2005) mean drop axis ratios and oscillation model described in section 5.2 and 5.3. The precision of L required to estimate μ decreases as Z_{DR} increases. The f_{hv}^{max} is assumed to be 0.9963 to match the case study in Section 5.4.

of the drop size, they should not vary with environmental conditions. In this analysis, the oscillations are included in the $L-Z_{DR}$ forward model by integrating over Gaussian PDFs of axis ratios (Thurai and Bringi, 2005) in the Gans theory computations. Figure 5.3 shows the choice of drop shape model and oscillations used in the following retrieval. Figure 5.4 shows the effect of including drop oscillations on computed L and Z_{DR} for values of μ equals -1 (solid lines) and μ equals 16 (dashed lines). The grey lines show when no oscillations are included in computations of L and Z_{DR}, and the black lines show when the oscillations shown in figure 5.3 are included. The importance of including drop oscillations for the purpose of estimating μ increases with increasing Z_{DR}; the difference between L at μ equals 16 computed with and without oscillations is as large as an equivalent change in μ of approximately 8. The modification of the oscillation magnitudes for drop diameters smaller than 2 mm has a relatively small impact (less than 0.01) on predicted L for Z_{DR} larger than 0.8 dB where retrievals of μ are attempted. However, it is found that the use of Szakáll *et al.* (2010) oscillations for all drop diameters has a large impact on predicted L values (for μ equals -1, L is approximately 0.1 lower). This is potentially important for retrievals of μ.

Comparatively large amplitude (but short lived, lasting less than approximately 0.4 s) collision induced oscillations can also occur (Szakáll *et al.*, 2014). Rogers (1989) estimate that the collision rate for an average rain drop in a 55 dBZ rain column is approximately 1 min^{-1}. This would imply that rain drops (even in very heavy rainfall) spend an almost negligible fraction of time (approximately 0.5%) affected by collision-induced oscillations. Rain drop clustering increases the likelihood of these collisions (Jameson and Kostinski, 1998). For rain rates of around 10 mm hr^{-1} (comparable to those presented in the following case studies), McFarquhar (2004) estimate the collision rate to be approximately 5 min^{-1}, implying drops are affected only 3% of the time. For very large rain rates (100 mm hr^{-1}), this fraction increases to 6% as the collision rate approximately doubles to 10 min^{-1}. Consequently, their impact on L measurements is likely to be small and can be ignored, other than for exceptional rain rates (Thurai and Mitra, 2013).

Figure 5.5 shows how L varies as a function of Z_{DR} for gamma distributions with μ equal to -1, 0, 2, 4, 8, 12 and 16 computed using Gans theory with the drop shape and oscillation model discussed above (shown in figure 5.3). Note that lines of constant μ diverge with increasing Z_{DR}. For $Z_{DR} \gtrsim 0.5$ dB, it becomes possible to distinguish μ, given the typical error on an L measurement (shown in Figure 5.7).

5.4 Case study: 25 November 2014

On the 25 November 2014, some showers passed near Chilbolton and were sampled by CAMRa. Several dwells were made at 1.5°, for a total of approximately 2.5 hours. Strict data quality filters were applied: SNR greater than 34 dB to avoid biasing

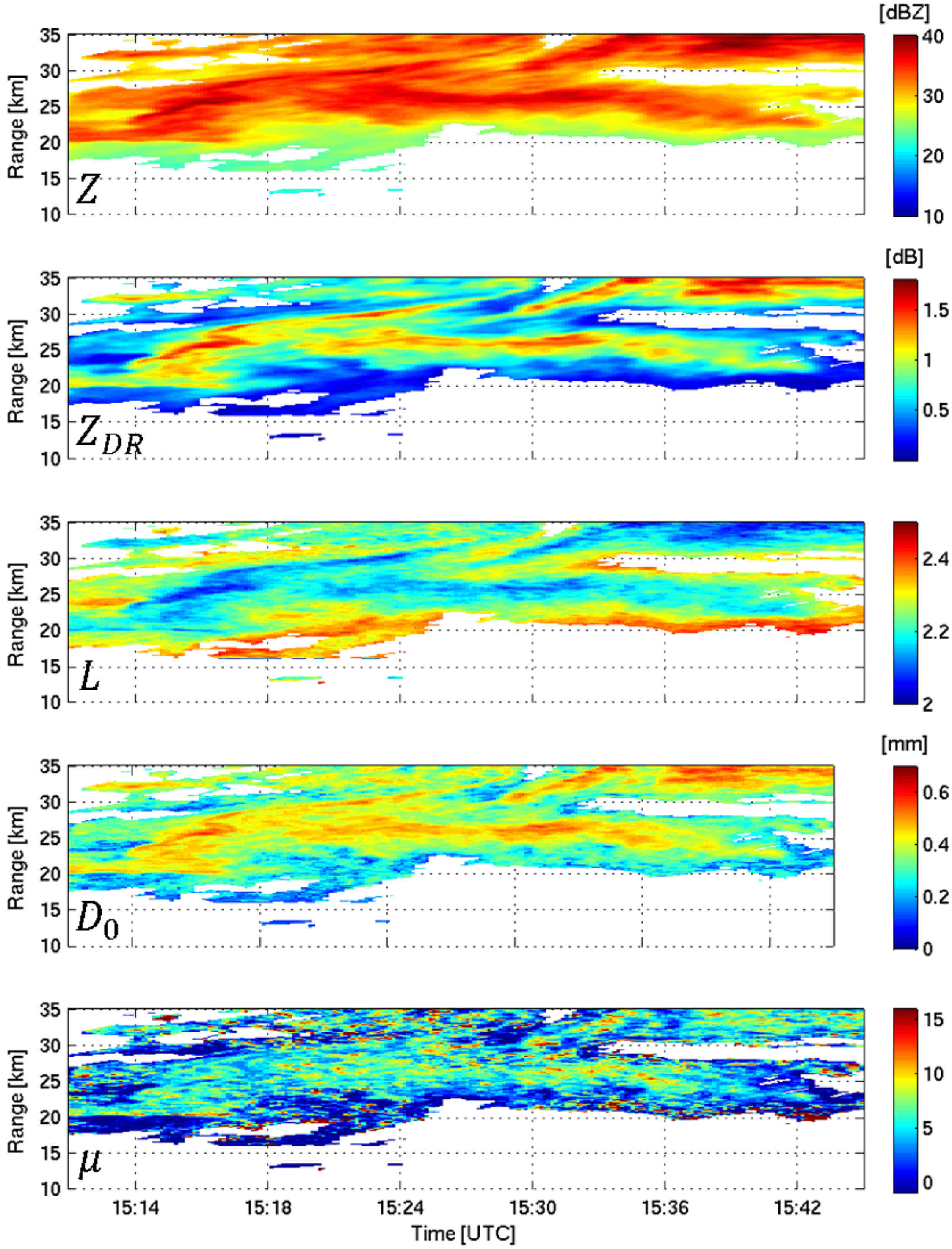

Figure 5.6 1.5° elevation dwell of Z, Z_{DR} and L from 1510 UTC on 25 November. Data has been averaged to 300 m and 30 s. Also shown are the retrieved D_0 and μ values for this case study.

L low, linear depolarisation ratio (LDR) smaller than -27 dB to ensure no melting particle contamination or ground clutter and range greater than 5 km to avoid near-field effects. Figure 5.6 shows the observed Z, Z_{DR} and L from an example dwell made at 1510 UTC. The inverse relationship between Z_{DR} and L is clearly evident from these observations; L decreases as Z_{DR} increases due to the increase in the breadth of the drop axis ratio distributions. At its peak, Z_{DR} is approximately 1.8, and its minimum, L is approximately 2.

To estimate μ and D_0, theoretical L and Z_{DR} were computed using Gans theory and the drop shape and oscillation model discussed in sections 5.2 and 5.3 (see figure 5.5). Observations were averaged from 10 to 30 s and from range gates of 75 to 300 m to increase the measurement precision of L. At each gate, the most likely pair of μ and D_0 given the observed L and Z_{DR} values was obtained by selecting the closest point in a look-up table of Gamma DSD calculations. The retrieved μ and D_0 are shown in figure 5.6. Figure 5.7a shows the observed L (binned every 0.02) and Z_{DR} (binned every 0.05 dB) for this day. Overlayed are lines of constant μ equal to -1, 0, 2, 4, 8, 12 and 16. Figure 5.7b is the same distribution normalised to sum to 1 for each Z_{DR} bin. The f_{hv}^{max} on this day was calculated to be 0.9963 (see section 3.4.4). The observations of L and Z_{DR} are generally well contained within the expected range. The median error on each L measurement, σ_L, is approximately 0.025, and is shown as a representative error bar in figure 5.7. A comparison of these data with disdrometer measurements from Williams *et al.* (2014) and Cao *et al.* (2008) is included. In the Williams *et al.* (2014) experiment, the mass spectrum mean diameter (D_m) and mass spectrum standard deviation (σ_m) were measured using a 2DVD. A $\sigma_m - D_m$ fit was derived from 18969 1-minute drop spectra (which can readily be converted to a $\mu - D_0$ fit). This was in turn used to predict a $L - Z_{DR}$ relationship, shown by the grey dashed line. L and Z_{DR} were also predicted using the Cao *et al.* (2008) $\mu - \Lambda$ relationship, also derived from a 2DVD, where:

$$\Lambda = \frac{3.67 + \mu}{D_0} \tag{5.1}$$

Predicted L and Z_{DR} using this relationship are shown by the black dashed line in

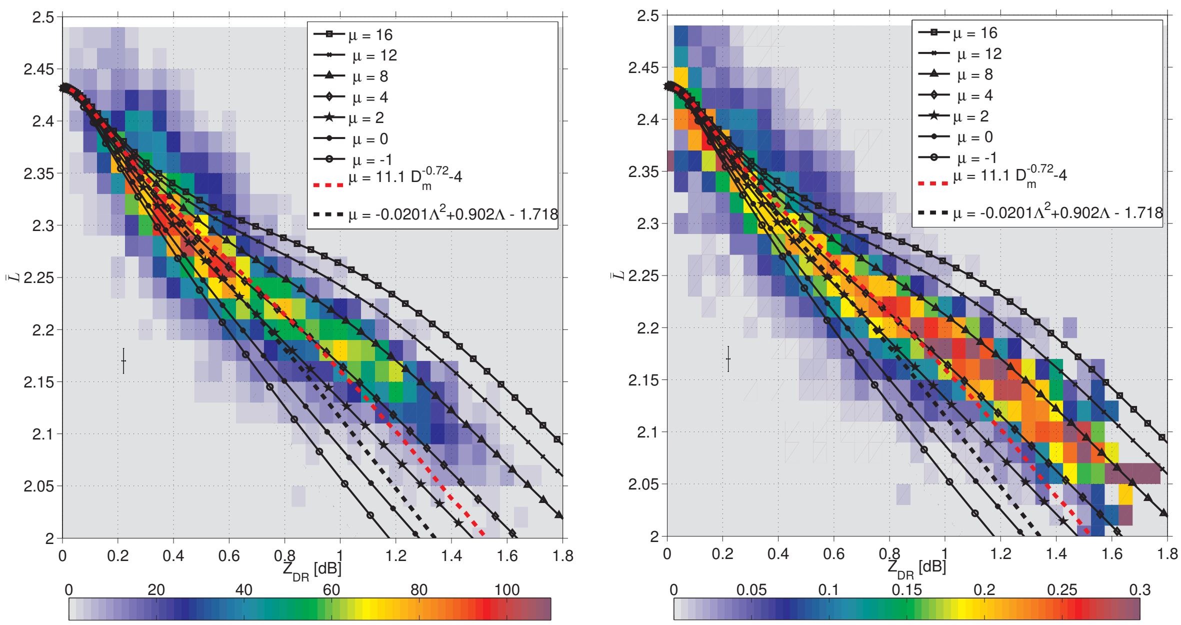

Figure 5.7 (a) 2D PDF of L and Z_{DR} observations, and (b) normalised 2D PDF such that the distribution equals 1 for each Z_{DR} bin for observations of L and Z_{DR} collected from dwells on 25 November 2014. L is binned ever 0.02, and Z_{DR} every 0.05 dB. Overplotted are theoretical L and Z_{DR} computed using Gans theory for gamma distributions of μ equal to -1, 0, 2, 4, 8, 12 and 16. Typical errors on L and Z_{DR} are shown as error bars; the error on Z_{DR} is very small. The red dashed line is the predicted L and Z_{DR} observations using DSD parameters from the power-law fit to disdrometer measurements in Williams *et al.* (2014). The black dashed line is the predicted L and Z_{DR} observations using the $\mu - \Lambda$ relationship of Cao *et al.* (2008). The f_{hv}^{max} for this day is measured to be 0.9963.

figure 5.7.

The median and inter-quartile range of retrieved μ per Z_{DR} bin for this day is shown in figure 5.8. The median retrieved μ is 5 when Z_{DR} is 0.8 dB, increasing to 8 when Z_{DR} is 1.6 dB. There is significant spread in retrieved μ values, containing contributions

Table 5.1: Typical rain rates (R) for each of the case studies, calculated from disdrometer measurements (April) and radar retrieved N_0, D_0 and μ values (January, May and November)

Month	Typical R (mm hr^{-1})	Peak R (mm hr^{-1})
31 January 2014	1–3	8
25 April 2014	2–3	7
22 May 2014	2–7	>30
25 November 2014	2–5	10

from measurement uncertainty on L, as well as "true " microphysical variability. The impact of changes in L on retrieved μ is non-linearly related to μ; σ_L contributes more to retrieved μ variability for more monodisperse (higher μ) DSDs, compared to more polydisperse (lower μ) DSDs. Conversely, the contribution of σ_L to retrieved μ variability decreases as Z_{DR} increases, as the dual polarisation signature is larger and μ is more easily distinguishable (see figure 5.5). To estimate the contribution that the uncertainty on L measurements makes to this observed variability, μ was retrieved using the median $L \pm$ the representative uncertainty depicted in figure 5.7. This was then compared to the inter-quartile range of the retrieved μ for each Z_{DR} bin. For Z_{DR} bins of 0.8, 1, 1.2, 1.4 and 1.6 dB, it is estimated that 88%, 66% 32%, 31% and 27% of the variability respectively can be attributed to σ_L. For Z_{DR} greater than 1 dB, most of the variability seen in figure 5.8 can be attributed to "true" microphysical variability.

Further case studies of 31 January, 25 April and 22 May 2014 were also investigated. Typical rain rates for each of these case studies can be found in table 5.1. Figure 5.9 shows a comparison with retrieved μ for all of the case studies collected. Each of the dwells in January, April and November were made in stratiform rain, whereas the May case study contains dwells from convective rain. Overlayed are predicted mean μ values (solid grey) and upper and lower bounds that contain 55% of the measurements (dashed grey) of Williams *et al.* (2014) as a function of Z_{DR} from the disdrometer measurements. The solid black line shows the predicted $\mu - Z_{DR}$ using the $\mu - \Lambda$ relationship of Cao *et al.* (2008). There is a large spread in the radar retrieved median μ values from case to case. Each median μ estimate is from a very large number of retrieved μ estimates, such that the standard error is smaller than the markers themselves, and so is not shown. The values of retrieved μ in January are approximately 0, close to an exponential DSD for all Z_{DR} smaller than 1.1 dB. This is below that predicted by Williams *et al.* (2014), but agrees well with μ predicted by Cao *et al.* (2008). Interestingly, the case studies of April and November show μ increasing with Z_{DR} between 0.5 dB and 1.5 dB, compared to the trend seen by Williams *et al.* (2014) and Cao *et al.* (2008) towards an exponential DSD. The retrieved median μ values from the May case study, although agreeing with the decreasing trend with Z_{DR}, are significantly above the Cao *et al.* (2008) predictions

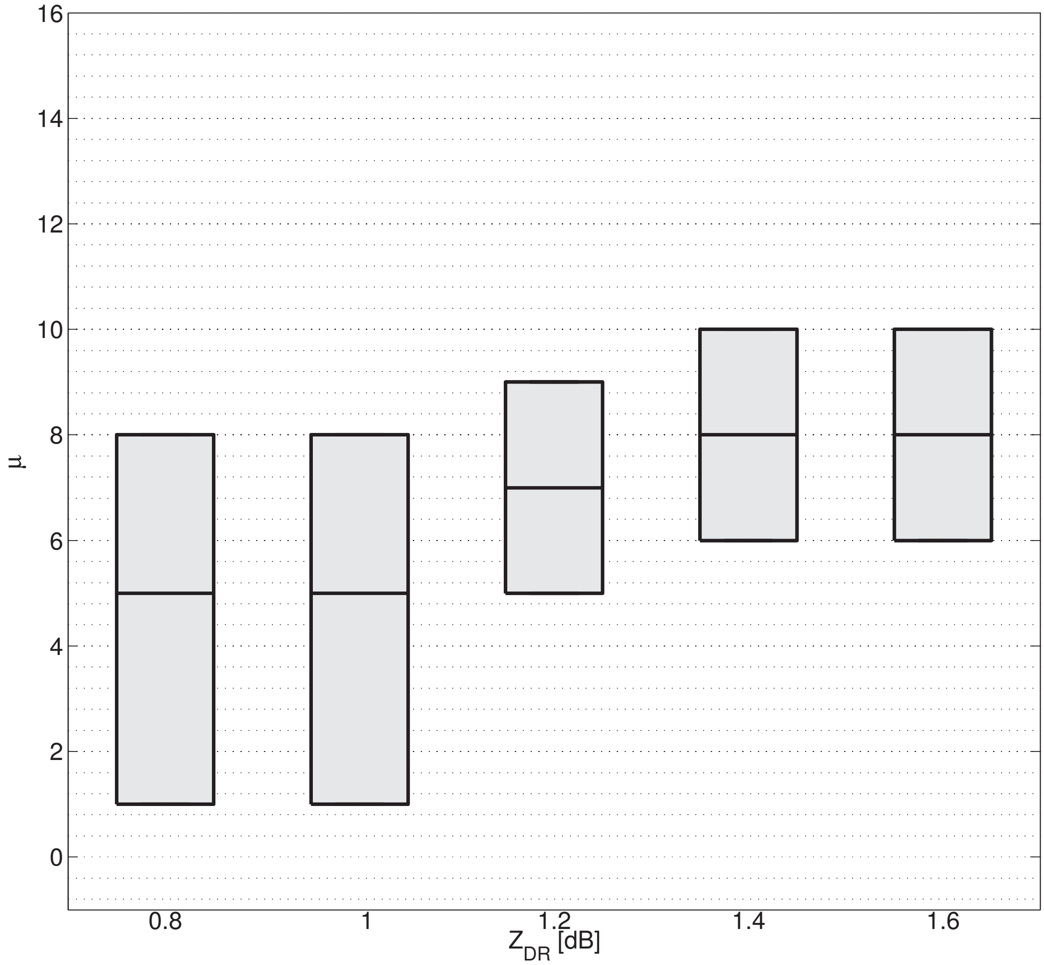

Figure 5.8 Box plot of retrieved μ as a function of Z_{DR} for Z_{DR} bins of 0.2 dB on 25 November 2014, showing the median and inter-quartile range of the data.

and the upper bound of μ from Williams *et al.* (2014). The retrieval suggests that in this case, the rain rate would be overestimated by almost 2 dB if an exponential DSD or the fit of Cao *et al.* (2008) is assumed. Whereas the μ values are not outside the full range of data measured by Williams *et al.* (2014), the use of the proposed $\mu - D_m$ relationship would cause an overestimate of approximately 1 dB (see figure 1.8).

5.5 Discussion

The retrievals of μ shown here using L and Z_{DR} are typically larger than the radar estimates of μ of between 1—3 made by Thurai *et al.* (2008) and 0—2 of Illingworth and Caylor (1991). Perhaps this is not surprising, given that the imperfect co-location

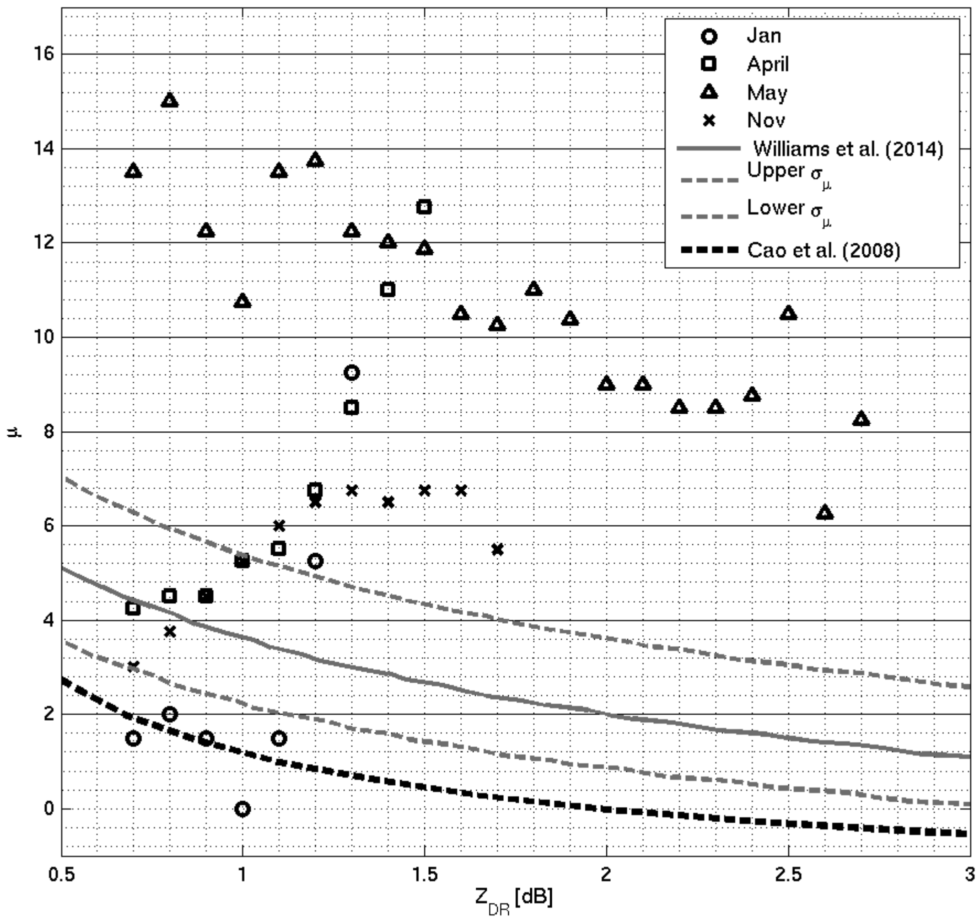

Figure 5.9 Median retrieved μ as a function of Z_{DR} for Z_{DR} bins of 0.1 dB for case studies of 31 January, 25 April, 22 May and 25 November 2014. The solid line is the predicted μ as a function of Z_{DR} from the power law fit to disdrometer measurements of Williams *et al.* (2014), and σ_μ corresponds to the upper and lower bounds that contain 55% of the data. The solid black line shows the predicted $\mu - Z_{DR}$ using the $\mu - \Lambda$ relationship of Cao *et al.* (2008).

of the H and V sample volumes was unaccounted for, and their $\hat{\rho_{hv}}$ would have been biased low due to averaging ρ_{hv} rather than L (see section 3.3), both of which are accounted for in our data. Furthermore, Illingworth and Caylor (1991) do not include drop oscillations in their retrievals, which will have led to a significant underestimate of μ. Whereas there is some agreement of the magnitudes of μ with predicted Williams *et al.* (2014) and Cao *et al.* (2008) values for Z_{DR} smaller than 1 dB, the apparent opposite trend towards more monodisperse distributions is consistent among 3 of the

4 case studies. For the retrieved μ to agree with the trend predicted by Williams *et al.* (2014) or Cao *et al.* (2008), a reduction in the drop oscillation amplitudes for smaller drops would be required so that predicted L values are higher. However, this would not explain the difference between the May retrieval results and the predicted μ from disdrometer measurements; it would require oscillations that are at least an order of magnitude *larger* to bring these median μ estimates into agreement with Williams *et al.* (2014) or Cao *et al.* (2008). An incorrect parameterisation of the drop oscillations alone is unlikely to be able to account for the disagreement with Williams *et al.* (2014) and Cao *et al.* (2008), however, to better establish the accuracy of the technique, a better quantification of raindrop oscillations is desirable.

μ estimates derived using radar are sensitive to higher moments of the DSD, whereas disdrometer estimates tend to use lower moments of the DSD (Cao and Zhang, 2009). This could be partly responsible for the differences between the radar and disdrometer estimated μ values. If the DSD shape is not perfectly described by equation 1.3, the "effective " μ which is derived may be different even if the underlying DSD shape is the same. It is also possible that this is simply natural variability of the DSD in different types of rainfall (i.e. convective and stratiform) has been observed, and there is not a universal $\mu - D_0$ relationship. More case studies are needed to gather a statistical understanding of the behaviour of μ using this retrieval method.

5.6 Implications for operational use of L

Operational radar networks favour the use of rapid scan rates to maximise sample frequency and volume. The UK Met Office operational network uses C-band (5.5 cm wavelength) radars, typically transmitting either a short (0.25 μs) or long pulse (2 μs) with a pulse repetition frequency of 300 Hz. These provide range gates of 75 m and 300 m respectively; the shorter pulse allows a greater maximum unambiguous velocity. The half power beamwidth of these radars is 1°. Operationally, it is desirable to retrieve rain rates with a spatial resolution of 2 km or better. In what follows, the potential of these radars to retrieve μ operationally (to 1 km^2 resolution) is discussed, based on the use of the "short" radar pulse. It is difficult to quantify the scales of "true" μ variability from figure 5.6, as for Z_{DR} smaller than approximately 0.8 dB, there is a dominating contribution to μ variability from measurement uncertainty in L. However, based on the standard deviation of the 300 m 30 s resolution measurements in figure 5.8 (when Z_{DR} is greater than 0.8 dB), it appears reasonable to assume μ is approximately constant over scales of 1 km^2.

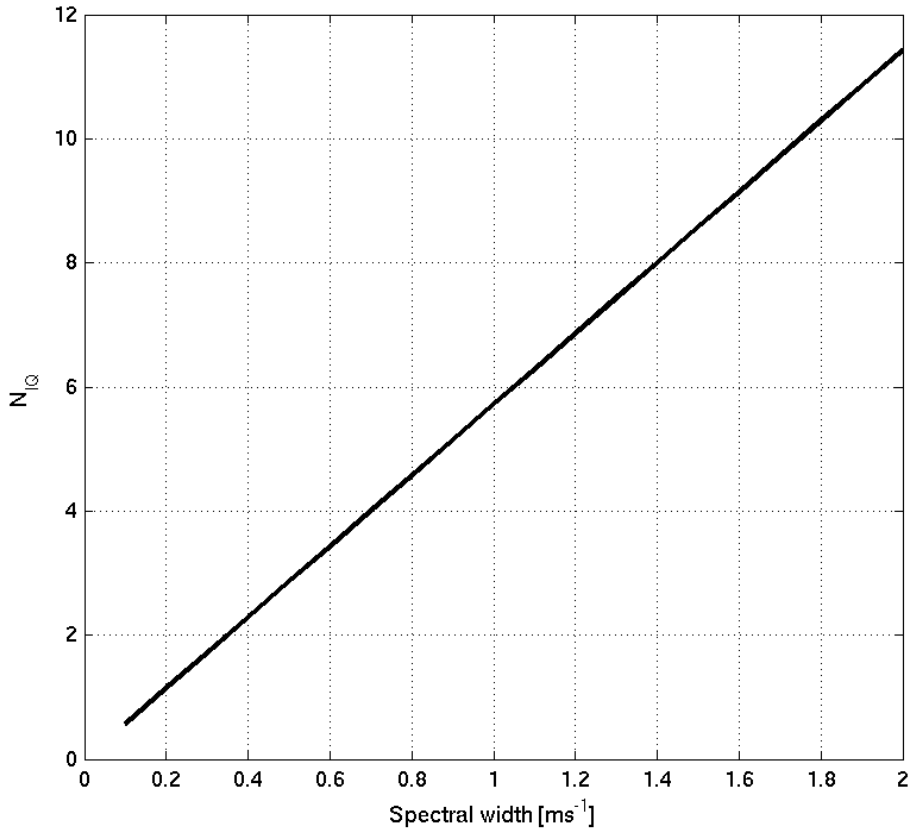

Figure 5.10 The number of independent pulses per 300 m range gate, assuming a dwell time of 0.11 s, which is typical per ray for the Met Office radars.

The low elevation angle plan position indicator (PPI) scans take approximately 40 s to complete, which means that the dwell time for each 1° beam is 0.11 s. The number of independent I and Q pulses in each 75 m range gate for this dwell time as a function of spectral width is shown figure 5.10; for a typical spectral width of 1 ms^{-1}, only approximately 6 pulses are independent. For example, at a range of 30 km, an area of 1 km^2 corresponds to 2° of azimuth (two rays) and approximately thirteen 75 m range gates. The number of independent pulses is therefore approximately $2 \times 13 \times 6 = 156$; σ_L is 0.07. Whereas this may not be sufficient to distinguish μ to as high a resolution as the retrieval presented here (which can afford more averaging), it is sufficient to decipher whether μ is 'high' or 'low' (see figure 5.5). Practically, as illustrated in figure 1.8, this may be all that is necessary to offer improved rain rate estimates; that is to say it is relatively unimportant whether μ is 8 or 16, but it is very important to know if it is 0 or 4. Therefore, this method could (with sufficient care to ensure only rain echoes and good SNR) allow for improved rain rates using Z, Z_{DR} and L compared to only Z and Z_{DR}.

For the typical σ_L used in these calculations, the approximate error on the retrieved rain rate can be approximated by considering the contribution of σ_L to the uncertainty in μ and referring to figure 5.5. For a "typical" μ of 6, the range of retrieved μ is approximately $\pm$ 4. Referring to figure 1.8, it can be seen that this corresponds to a difference in rain rate of $\pm$ 0.5 dB, or $\pm$ 12.5%. The impact of uncertainty in μ on rain rate is almost constant for all Z_{DR} (each of the μ lines are approximately parallel in figure 1.8 for $Z_{DR} \gtrsim 0.5$ dB). Therefore, this error will decrease for higher rain rates as the contribution of σ_L to uncertainty in μ decreases as a function of Z_{DR}. However, at larger rain rates, attenuation at C-band can be severe.

The use of the longer pulse would result in the averaging of less gates; N_{IQ} per 1 km^2 would be a factor of four smaller, and σ_L would therefore be a factor of two larger (0.14). Consequently, the uncertainty in μ is likely to be quite large in comparison, and is unlikely to offer much improvement over using only Z and Z_{DR}. However, as discussed above, it is in principle possible to retrieve μ using the shorter pulses. The SNR for the shorter pulses is less than for longer pulses as less total power is transmitted. The requirement of a strict SNR threshold potentially restricts the use of this technique to areas close to the radar. It would be interesting to examine the possibility of correcting for poor SNR in this retrieval technique in future work.

5.7 Summary

High-precision measurements of L and Z_{DR} in rainfall are used to estimate μ in the gamma DSD for four case studies. Estimates of μ in stratiform rain somewhat agree in magnitude with those from disdrometer studies for small Z_{DR}, but there appears to be a tendency to more monodisperse DSDs between Z_{DR} equals 0.8 and 1.5 dB, unlike the trend towards an exponential distribution suggested by disdrometer measurements. The convective case study does display this trend toward lower μ as Z_{DR} increases, but the magnitude of μ remains much larger than predicted by disdrometer measurements. If true, this would lead to overestimates of retrieved rain rate by approximately 1 dB if the $\mu - D_m$ relationship of Williams *et al.* (2014) is used, or 2 dB if an exponential distribution or the $\mu - \Lambda$ relationship of Cao *et al.* (2008) is used. We find that the μ retrieval exhibits sensitivity to the choice of drop oscillation model. A better understanding of raindrop oscillations would be useful to fully establish the accuracy of the retrieval technique.

The variability in the radar retrieved μ could simply be natural variability of the DSD between convective and stratiform rainfall; there may not be a universal $\mu - D_0$ relationship. More case studies are desirable to investigate this further.

The μ retrieval technique employed here offers improvements over the radar estimates of Illingworth and Caylor (1991) and Thurai *et al.* (2008). Illingworth and Caylor (1991) did not take into account the imperfect co-location of the H and V sample volumes on measurements of ρ_{hv}, the effect of drop oscillations, or the fact their ρ_{hv} estimates would be biased low by averaging short time-series. Each of these effects would cause μ to be underestimated. The same is true of Thurai *et al.* (2008), however drop shapes measured by 2DVD measurements include oscillations, and so are included in their μ estimates.

The use of L operationally to retrieve μ is limited by use of rapid scan rates and the corresponding few independent I and Q samples. However, assuming that μ is a smoothly varying parameter, averaging L could help improve rain rate retrievals; the uncertainty on operationally retrieved rain rates using the retrieval technique presented here is estimated to be approximately $\pm$ 12.5%. Practically, retrieved rain rates are less affected by changes in higher values of μ compared to changes in lower values. Therefore, operationally, simply being able to distinguish regions of 'high' and 'low' μ with L could be sufficient to provide an improvement over existing $Z - Z_{DR}$ retrieval techniques.

Chapter 6

Summary and future work

6.1 Mixed-phase clouds

Mixed-phase clouds are one of the most poorly understood cloud types. Consequently, they tend to be poorly parameterised in numerical weather and climate models. It is possible to classify them as one of two types: those containing a layer of supercooled liquid water (SLW) at cloud top (Type I) and those containing SLW embedded within deep ice cloud (Type II). Neither of these cloud types are fully understood; in particular, there is a distinct lack of observations of Type II mixed-phase clouds. This thesis has attempted to address this deficiency, by presenting statistics of the polarimetric radar signatures of these cloud types, and developing a novel polarimetric radar retrieval technique to reveal the microphysics in these regions.

Fundamentally, this work exploits the property of pristine crystals to orient themselves with their major axis aligned horizontally as they fall due to aerodynamic effects, and the fact that pristine oriented crystals tend to be associated with the presence of SLW, and therefore act as a proxy for its presence (Hogan *et al.*, 2003a).

6.1.1 Frequency of occurrence of Type II mixed-phase clouds

In chapter 2, the statistics of 10 weeks of continuous 35 GHz radar observations at an elevation angle of 45° were presented. Clouds were characterised as either (a) irregular polycrystals or aggregates, (b) Type II or (c) Type I mixed-phase using measurements of DDV and Z_{DR}. It is shown that Z_{DR} alone is not sufficient to distinguish between these polycrystals and aggregates and Type II regions, as frequency distributions have a similar shape and range of Z_{DR}. Pristine oriented crystals forming amongst irregular ice crystals tend to fall more slowly and have a high "intrinsic Z_{DR}". Therefore, observations of DDV, which is sensitive to differences in shapes and fall speeds of particles within a sample volume can be used to identify Type II mixed-phase regions. Using thresholds of DDV and Z_{DR}, it was estimated that during the 10 weeks of observations, irregular polycrystals and aggregates were present 72% of the time, consistent with in-situ aircraft observations (Korolev *et al.* 2000, Stoelinga *et al.*, 2007). Type II mixed-phase clouds occurred 27% of the time and Type I mixed-phase clouds occurred 1% of the time. However, this apparent lack of occurrence of Type I clouds could be because the definition of frequency of occurrence is the fraction of all pixels; there are many more pixels from deep frontal clouds. The frequency of occurrence of each cloud type was also shown as a function of temperature. At warmer temperatures (e.g. -15 and -10°C), Type II mixed-phase clouds were a significant occurrence; 40% of all data was identified as a Type II region. These statistics complement the growing body of observations of mixed-phase clouds. They also motivate further investigation of Type II mixed-phase clouds given their prevalence, especially at warmer temperatures.

6.1.2 A new variable: L $= -\log_{10}(1 - \rho_{hv})$

The variable ρ_{hv} is sensitive to the variety of shapes within a radar pulse volume. However, its quantitative use is hampered by lack of rigorous confidence intervals accompanying ρ_{hv} estimates. In chapter 3, a new variable $L = -\log_{10}(1-\rho_{hv})$ is defined. Unlike frequency distributions of ρ_{hv} measurements which are highly negatively skewed, L is Gaussian distributed with a width predictable by the number of independent I and Q samples, which in turn can be estimated using the Doppler spectral width. This allows, for the first time, the construction of rigorous confidence intervals on each ρ_{hv} measurement. The predicted errors using this new method were verified using high quality measurements in drizzle from the Chilbolton Advanced Meteorological Radar. This variable is also of much greater practical use because confidence intervals do not require knowledge of the unknown "true" ρ_{hv} that one is trying to estimate and no bias is introduced by averaging many ρ_{hv} samples. Chapter 3 also describes a technique to account for the imperfect co-location of H and V sampling volumes on ρ_{hv} measurements, which is necessary to account for when comparing theoretical and observed values ρ_{hv}.

6.1.3 Retrieving the microphysics of Type II mixed-phase clouds

The prevalence of Type II mixed-phase clouds indicated in chapter 2 motivates further investigation of these cloud types. However, a practical problem of using Z_{DR} in these regions is that it is reflectivity-weighted; the presence of even relatively few, but larger irregular crystals or aggregates can dominate the radar backscatter and mask the signal from co-existing pristine crystals (Bader *et al.*, 1987). In chapter 4, a novel polarimetric retrieval technique is developed that utilises the newly defined variable L from chapter 3 and Z_{DR} to retrieve both the intrinsic Z_{DR} of pristine crystals (Z^P_{DRI}) and their relative contribution to radar reflectivity (C). Two case studies are presented. The retrieval profiles show that enhancements of Z_{DR} embedded within deep ice are typically produced by pristine oriented crystals with large Z_{DRI} values (3—7 dB), with varying contributions to the radar reflectivity. The retrieved C and Z^P_{DRI} profiles provide an insight into the microphysics of the pristine oriented crystals that would otherwise be masked by the irregular polycrystals or aggregates. The effective density of the pristine oriented crystals was estimated by comparing the retrieved Z^P_{DRI} with forward modelled Z_{DRI} using modified Gans theory (Westbrook, 2013); estimates range from 0.50 — 0.90 g cm^{-3}, and were consistent with laboratory studies of ice crystals grown at similar temperatures to those observed (Takahashi *et al.*, 1991; Fukuta and Takahashi, 1999).

Furthermore, in the first case study, DDV measurements could be used to estimate the fall speeds of pristine crystals and aggregates, when combined with the observed vertical velocity from the Copernicus 35 GHz Doppler radar. The results were consistent with plate-like crystals grown in the laboratory (e.g. Kajikawa 1972).

In the second case study, in-situ measurements were also collected by the FAAM aircraft at microphysically significant heights. Cloud imaging probes on-board the aircraft support the conceptual model used in the retrieval; the observation of plate-like crystals with extensions growing amongst polycrystals and aggregates are consistent with retrieved C and Z^P_{DRI}. Bi-modal Doppler spectra were also measured by the

Copernicus radar in this case study. C was estimated by separating contributions to radar reflectivity of each crystal type by the observed Doppler velocity. C estimated in this way was qualitatively similar to C estimates, but several dB lower than that using the new polarimetric retrieval.

Fundamentally, the newly developed retrieval technique demonstrated in chapter 4 allows deeper insight into the microphysical properties and characteristics of Type II mixed-phase clouds than was previously possible. Their high frequency of occurrence, especially at warmer temperatures motivates further study; better observations are the basis of an improved representation in numerical weather and climate models.

6.2 Rain drop size distributions

Measurements of the rain drop size distribution using disdrometer measurements tend to be biased due poor sampling or small and large drops. This thesis attempts to resolve this problem by using radar measurements to estimate μ, which is preferable to disdrometers due the relatively very large number of drops that are sampled. A technique to retrieve μ in rainfall using high-precision measurements of the newly defined variable L and Z_{DR} was presented for four case studies.

Estimates of μ in stratiform rain somewhat agree in magnitude with those from disdrometer studies for small Z_{DR}, but there appears to be a tendency to more monodisperse DSDs between $Z_{DR} = 0.8$ and 1.5 dB, unlike the trend towards an exponential distribution suggested by previous disdrometer statistics in the literature. There is a decrease in μ with increasing Z_{DR} in the convective case study, but the magnitudes of these μ were much larger than predicted by disdrometer measurements. This would cause overestimates of retrieved rain rate by approximately 1 dB if the $\mu - D_m$ relationship of Williams *et al.* (2014) is used, or 2 dB if an exponential distribution or the $\mu - \Lambda$ relationship of Cao *et al.* (2008) is used. It is shown that the inclusion of drop oscillations for the purpose of retrieving μ is essential.

These μ estimates are an improvement over previous attempts to measure μ with ρ_{hv} of Illingworth and Caylor (1991) and Thurai *et al.* (2008). Unlike Illingworth and Caylor (1991), the effect of both imperfect co-location of the H and V sample volumes and drop oscillations on measurements of ρ_{hv} is accounted for. Furthermore, the μ estimates presented in this thesis are not biased by averaging short time series estimates of ρ_{hv}. Each of these effects would cause μ to be underestimated. Thurai *et al.* (2008) did not account for the imperfect co-location of beams, even though drop shapes measured by a 2DVD were used to derive empirical $\rho_{hv}-\sigma_m$ relationships which did include oscillations.

The potential of using L to retrieve μ operationally is discussed. The use of rapid scan rates favoured by operational radar networks offers very few independent I and Q samples. However, it is suggested that by averaging to the order of 1 km^2, it should be possible to retrieve rain rates with an uncertainty of $\pm$ 12.5%. Practically, however, simply being able to distinguish regions of 'high' and 'low' μ with L could be sufficient to provide an improvement over existing $Z - Z_{DR}$ retrieval techniques.

6.3 Future work

6.3.1 Mixed-phase clouds

There are a number of interesting avenues of future work that arise from the results of this thesis. Further observations of mixed-phase clouds, and in particular Type II mixed-phase clouds, are still required to fully understand the microphysical processes occurring within them. It would be interesting to collect further data with the 35 GHz radar at an elevation angle of 45° over a longer period of time, preferably over the winter months when the melting layer is lower (there would be more pixels colder than 0°C) and there are typically more frontal systems passing over the UK. It would also be beneficial to measure the variable ρ_{hv}, which unfortunately was not successfully recorded during the 10 weeks of continuous measurements presented in chapter 2. ρ_{hv} could be used to develop statistics of Type II mixed-phase in the same way as DDV by diagnosing a mixture of ice particle shapes. Or, it could be used in the polarimetric retrieval technique demonstrated in chapter 4 to obtain long-term statistics of retrieved of C and Z_{DRI}^{P}. Collecting long-term coincident measurements of DDV, Z_{DR} and L

with Copernicus would also allow statistics of particle fall speeds to be collected, since a 94 GHz radar is also installed at Chilbolton which could provide vertical Doppler velocity information.

There is also potential to use the data collected during the 45° observational campaign together with Doppler lidars installed at Chilbolton. These instruments can easily detect liquid water layers (when the beam is not attenuated, such as for Type I mixed-phase clouds). It would be interesting to evaluate the polarimetric signatures at locations where SLW is detected by the lidar. Not only would this allow the investigation of the microphysics of mixed-phase clouds directly, it could allow Type II mixed-phase clouds to be inferred statistically given observed polarimetric signatures.

The retrievals of C and Z_{DRI}^{P} in chapter 4 are shown to be sensitive to the assumption of the shape of polycrystals and aggregates. In the results presented, this assumption was based on the Z_{DR} measurement just above the melting layer where it is known that large pseudo-spherical aggregates dominate Z_{DR}; it is difficult to measure directly above the embedded mixed-phase region. Aircraft data and Z_{DR} measurements (as well as observational evidence from Z_{DR} profiles in chapter 2) suggest that Z_{DRI}^{A} may in fact increase with increasing height. This would be consistent with overestimating of C with the polarimetric technique which seemed to be suggested by the comparison with Doppler spectra (although a quantitative comparison is not strictly possible since the profiles are not co-located in space). Since these retrievals depend on an accurate assumption of the shape of irregular ice crystals and aggregates, this warrants further investigation.

Further microphysical information provided by other polarimetric measurements such as K_{DP}, which is only sensitive to the number and shape of aligned particles could allow further microphysical information to be retrieved. For example, combined with retrieved Z_{DRI}^{P}, K_{DP} could be used to estimate ice water contents of the pristine crystals using a method similar to Ryzhkov and Zrnic (1998). Furthermore, gradients in retrieved radar reflectivities from each crystal type with height could allow estimation of the growth rates of pristine crystals and aggregates. More case studies with stronger polarimetric signatures would be useful to fully exploit this new retrieval technique to further investigate the microphysical properties and processes in deep stratiform mixed-phase clouds. It would also be interesting to explore the wealth of information that is collected with operational radars which are now reporting dual polarisation variables continuously. Polarimetric measurements from higher elevation PPI scans could be used to estimate the frequency of occurrence of mixed-phase clouds based on ρ_{hv} and Z_{DR}. Furthermore, this data could be used to apply the retrieval developed in chapter 4 to obtain the statistical behaviours of C and Z_{DRI}^{P} with temperature, or even in combination with K_{DP} to estimate IWC from pristine oriented crystals. There is also the potential to use operational DDV, Z_{DR} and L measurements to identify mixed-phase conditions for the purpose of identifying aircraft icing conditions.

6.3.2 Drop size distributions

The μ retrieval technique demonstrated in chapter 5 could facilitate improved retrievals of rain rate. However, it was shown that the forward modelled L and Z_{DR} are sensitive to the choice of drop oscillation model. A better understanding of these oscillations would be useful to fully establish the accuracy of this retrieval technique. More case studies are also desirable to investigate the statistical properties of μ retrieval using this technique.

It is in principle possible to use L operationally to improve retrievals of rain rate. One caveat of this method is the requirement of a strict SNR threshold, which would tend to restrict the range that rain rate could be retrieved typically to the first few tens of kms. One possible way to alleviate this problem would be to account for SNR in the $L - Z_{DR}$ forward model in the same manner as the retrieval presented in chapter 4.

More work needs to be done to examine the full potential of this technique, and assess whether retrieved rain rates can indeed be improved.

Appendix A

The effect of imperfectly co-located H and V samples on ρ_{hv}

Consider two measurements of the (complex) amplitudes at horizontal and vertical polarisation A_H and A_V. If the two polarisations do not have perfectly matched sample volumes, then each amplitude is the sum of (i) a component which is common to both polarisations C_H, C_V, (ii) a component which is different for each polarisation D_H, D_V:

$$A_H = C_H + D_H \tag{A.1}$$

(and similarly $A_V = C_V + D_V$). The co-polar correlation coefficient is:

$$\rho_{hv} = \frac{\sum A_H A_V^*}{\sqrt{\sum |A_H|^2 \sum |A_V|^2}} \tag{A.2}$$

where the sums $\sum$ are taken over many reshufflings of the raindrops. Substituting in the expressions for A_H and A_V leads to:

$$\rho_{hv} = \frac{\sum C_H C_V^* + \sum D_H C_V^* + \sum C_H D_V^* + \sum D_H D_V^*}{\sqrt{\sum |C_H + D_H|^2 \sum |C_V + D_V|^2}} \tag{A.3}$$

The first term in the numerator dominates as the number of pulses is increased. This is because D_H, D_V, are uncorrelated with C_V, C_H (because the reshuffling of particles in the different sample volumes is not connected or organised in any way), while C_H and C_V are highly correlated (because the true ρ_{hv} is close to 1). The final term is small because D_H, D_V, are not correlated (by the same argument), and this term is small in any case since $|D| \ll |C|$)

This leaves:

$$\rho_{hv} = \frac{\sum C_H C_V^*}{\sqrt{\sum |C_H + D_H|^2 \sum |C_V + D_V|^2}} \tag{A.4}$$

In the case of a perfect radar with perfect co-location of the H and V samples, then D_H, D_V are zero and we get a correlation coefficient which is the true ρ_{hv} which we are trying to obtain (i.e. setting $A = C$ in equation A.2).

In general, for an imperfect radar, we have $D_H, D_V > 0$ and from the results above we see that:

$$\rho_{hv} = \rho_{hv}^{\text{true}} \times f_{hv}^{max} \tag{A.5}$$

where

$$f_{hv}^{max} = \left(\frac{\sum |C_H|^2}{\sum |C_H + D_H|^2} \times \frac{\sum |C_V|^2}{\sum |C_V + D_V|^2} \right)^{1/2} \tag{A.6}$$

This result is directly analogous to the results of Bringi *et al.* (1983) on ρ_{hv} in the presence of noise. If we identify C as our "signal" and D as our "noise" this equation is identical to Equation A.1.

Crucially, the relationship between the true ρ_{hv} (ρ_{hv}^{true}) and the one which is actually observed is determined simply by how much power (on average over many pulses) comes from the particles which are different for the H and V sample volumes, relative to how much power comes from the particles which are common to the H and V sample volumes, and that this factor should be constant for different microphysical situations. Thus if we can measure ρ_{hv} in drizzle where we know $\rho_{hv}^{\text{true}} = 1$, then the measured ρ_{hv} is simply equal to f_{hv}^{max}. This scaling factor can then be applied to data from all other situations.

Appendix B

Computing Z_{DR} of raindrops and ice crystals

Differential reflectivity is the ratio of the backscatter from the H and V polarisations respectively:

$$Z_{DR} = \frac{\sigma_h}{\sigma_v} \tag{B.1}$$

where σ_h and σ_v are the mean backscatter cross-sections in the H and V polarisation respectively. Since it is known that pristine crystals and raindrops tend to fall with their major axes aligned horizontally, the problem of computing Z_{DR} for these particles for an elevation angle of 0° is relatively straightforward. This is because both the horizontally and vertically polarised incident fields are parallel to one of the axes of the particles. The backscatter cross-sections of a particle in the Rayleigh regime and in the far-field, can be related to the scattered electric field in an analogous manner to Seliga and Bringi (1976). The strength of the induced dipole ($\mathbf{p}$) in response to an applied electric field of magnitude, $\mathbf{E_0}$, is given by:

$$\mathbf{p} = 4\pi\epsilon_0 \mathbf{X}\mathbf{E}_0 \tag{B.2}$$

where $\mathbf{X}$ is the "polarisability" of the particle and ϵ_0 is the permittivity of free space. For hexagonal crystals which have two perpendicular axes of symmetry, $\mathbf{X}$ is diagonal, and can be written as a 3 x 3 tensor (Senior, 1976). The backscatter cross-section of a particle can therefore be given by (Westbrook, 2013):

$$\sigma = 4\pi k^4 |(\mathbf{X}\hat{\mathbf{E}}_0).\hat{\mathbf{E}}_0|^2 \tag{B.3}$$

where $\hat{\mathbf{E}}_0$ is a unit vector along the direction of polarisation. Once $\mathbf{X}$ is known for a particular shape, the backscatter and hence Z_{DR} can be easily computed. Analytical expressions are only possible for simple shapes such as an ellipsoid (Gans, 1912). For a Cartesian co-ordinate system, such that the principle axes of the ellipsoid are parallel to $\hat{\mathbf{x}}$, $\hat{\mathbf{y}}$ and $\hat{\mathbf{z}}$, the elements of $\mathbf{X}$ are:

$$X_{ii} = \frac{V}{4\pi} \times \frac{\epsilon - 1}{L_i(\epsilon - 1) + 1} \tag{B.4}$$

where V is the volume of the particle, L_i is a function of the aspect ratio and ϵ is their relative permittivity. For oblate spheroids, which have their $\hat{\mathbf{z}}$ orthogonal to the propagation direction of the incident electric field, these shape factors L_i are:

$$L_z = \frac{1 + e^2}{e^2}\Big(1 - \frac{1}{e}\tan^{-1} e\Big) \tag{B.5}$$

For prolate particles, these elements are:

$$L_z = \frac{1 - e^2}{e^2}\Big(- 1 + \frac{1}{2e}\ln\frac{1 + e}{1 - e}\Big) \tag{B.6}$$

where e is the eccentricity of the spheroid. For both oblate and prolate spheroids, the shape factors corresponding to the $\hat{\mathbf{x}}$ and $\hat{\mathbf{y}}$ axes are:

$$L_x = L_y = \frac{1 - L_z}{2} \tag{B.7}$$

Rain drops can be approximated as oblate spheroids, and so these shape factors are used to compute the Z_{DR} of raindrops in this thesis. However, Westbrook (2013) showed using the discrete dipole approximation that the assumption of pristine plates or columns as oblate or prolate spheroids (rather than hexagonal prisms) can lead to significant errors in estimates of Z_{DR}. Empirical modifications to the above shape factors were suggested:

$$L_z = \frac{1}{2}\Big(\frac{1 - 3/w}{1 + 3/w} + 1\Big) \tag{B.8}$$

$$L_x = L_y = \frac{1}{4}\Big(\frac{1-0.5w^{0.9}}{1+0.5w^{0.9}} + 1\Big) \tag{B.9}$$

where $w = 2a/L$ is the aspect ratio of the particle, which are much more accurate. For plate-like crystals falling with their $\hat{\mathbf{z}}$ axis pointing vertically and illuminated at zero degree elevation angle:

$$Z_{DR} = \frac{\sigma_h}{\sigma_v} = \frac{|X_{xx}|^2}{|X_{zz}|^2} \tag{B.10}$$

For columns, the situation is slightly more complicated as the $\hat{\mathbf{z}}$ of the crystal can be aligned in any azimuthal direction in the horizontal plane. For a vertically polarised wave, this is not a problem as at any azimuthal orientation, the incident field vector is still parallel to either axis $\hat{\mathbf{x}}$ or $\hat{\mathbf{y}}$. For hexagonal prisms $X_{xx} = X_{yy}$, therefore:

$$\sigma_v = 4\pi k^4 |X_{xx}|^2 \tag{B.11}$$

For a horizontally polarised wave, the backscatter must be integrated over all possible azimuthal orientations, therefore:

$$\sigma_h = 4\pi k^4 \Big(\frac{3}{8}|X_{zz}|^2 + \frac{3}{8}|X_{xx}|^2 + \frac{1}{4}|X_{xx}||X_{zz}|\Big) \tag{B.12}$$

and:

$$Z_{DR} = \frac{3|X_{zz}|^2}{8|X_{xx}|^2} + \frac{3}{8} + \frac{1|X_{zz}|}{4|X_{xx}|} \tag{B.13}$$

Computing Z_{DR} as a function of elevation angle

The Z_{DR} of ice particles illuminated at an arbitrary radar elevation angle (θ) can be computed in a similar manner. This time, because the incident field is not necessarily parallel to one of the principle axes of the particle, the components of induced dipole in each plane of the particle must be considered. Starting with plate crystals, the horizontal polarisation is always pointing in the $\hat{\mathbf{y}}$ direction (see figure B.1) for all elevation angles, so again:

$$\sigma_h = 4\pi k^4 |X_{xx}|^2, \tag{B.14}$$

and is not a function of elevation angle. However, with increasing elevation angle, the vertically polarised wave becomes increasingly in the same plane as the horizontally polarised wave. The backscatter for a vertically polarised wave is therefore:

$$\sigma_w = 4\pi k^4 |(\mathbf{X}\hat{\mathbf{E}}_w).\hat{\mathbf{E}}_w|^2 \tag{B.15}$$

where $\hat{E_w}$ is defined in figure B.1. At an elevation angle >0°, a dipole is induced in both the $\hat{\mathbf{x}}$ and $\hat{\mathbf{z}}$ directions. The polarisation is orthogonal to the $\hat{\mathbf{y}}$ axis and so no dipole is induced, therefore:

$$\hat{\mathbf{E}}_{\mathbf{w}} = \begin{pmatrix} \sin(\theta) \\ 0 \\ \cos(\theta) \end{pmatrix} \tag{B.16}$$

Substitution into equation B.15 yields:

$$\sigma_w = 4\pi k^4 X_{xx}^2 \sin^4(\theta) + 2X_{xx}X_{yy}\sin^2(\theta)\cos^2(\theta) + X_{xx}^2\cos^4(\theta) \tag{B.17}$$

Therefore, for plates:

$$Z_{DR} = \frac{X_{xx}^2}{(X_{xx}^2 \sin^4(\theta) + 2X_{xx}X_{yy}\sin^2(\theta)\cos^2(\theta) + X_{xx}^2\cos^4(\theta)} \tag{B.18}$$

Dividing both the numerator and denominator by X_{zz} yields:

$$Z_{DR}(\theta) = \frac{Z_{DR}(0)}{[\sqrt{Z_{DR}(0)}\sin^2(\theta) + \cos^2(\theta)]^2} \tag{B.19}$$

This equation is used to compute Z_{DRI}^P at horizontal incidence ($Z_{DRI}^P(0)$) in chapter 4. For columns oriented with their $\mathbf{z}$ axis pointing in the $\hat{\mathbf{x}}$ direction, σ_h is equivalent to σ_v for a plate crystal:

$$\sigma_h = 4\pi k^4\Big(\frac{3}{8}|X_{zz}|^2 + \frac{3}{8}|X_{xx}|^2 + \frac{1}{4}|X_{xx}||X_{zz}|\Big) \tag{B.20}$$

The components of the induced dipoles for a vertically polarised wave:

$$\mathbf{\hat{E}_w} = \begin{pmatrix} \cos(\theta) \\ \sin(\theta)\sin(\phi) \\ \sin(\theta)\cos(\phi) \end{pmatrix} \tag{B.21}$$

where ϕ is the azimuthal angle of the particle. Substitution into equation B.3 and averaging over all azimuthal angles yields:

$$\sigma_w = X_{xx}^2\Big(\cos^4(\theta) + \cos^2(\theta)\sin^2(\theta) + \frac{3}{8}\sin^4(\theta)\Big) + \frac{3}{8}X_{zz}^2\sin^4(\theta)\Big)$$

$$+X_{xx}X_{zz}\Big(\cos^2(\theta)\sin^2(\theta) + \frac{1}{4}\sin^4(\theta)\Big) \tag{B.22}$$

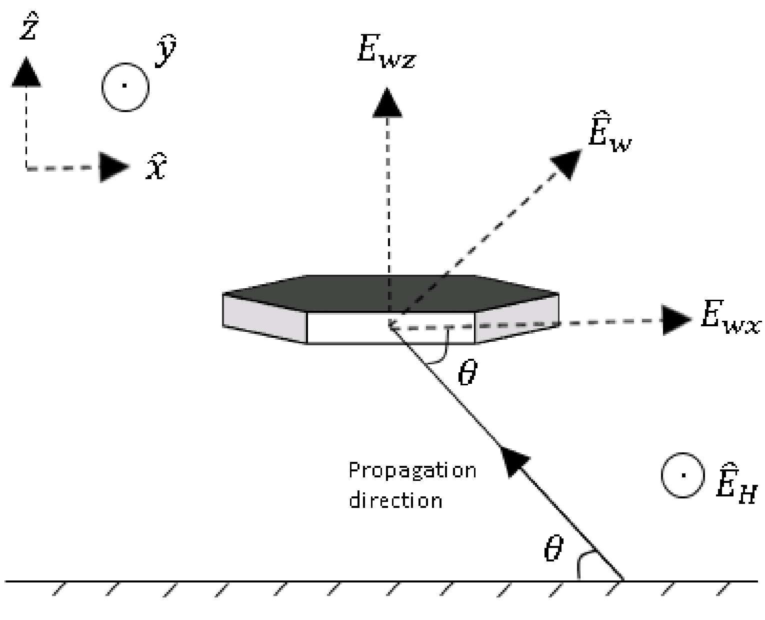

Figure B.1 Schematic of a plate crystal illuminated at an elevation angle θ.

and:

$$Z_{DR} = \frac{\sigma_h}{\sigma_w} \tag{B.23}$$

References

Bibliography

Andrić, J., Kumjian, M. R., Zrnić, D. S., Straka, J. M., and Melnikov, V. M. (2013). Polarimetric signatures above the melting layer in winter storms: An observational and modeling study. *Journal of Applied Meteorology and Climatology*, **52**(3), 682–700.

Bader, M. J., Clough, S. A., and Cox, G. P. (1987). Aircraft and dual polarization radar observations of hydrometeors in light stratiform precipitation. *Quart. J. Roy.Met. Soc.*, **113**(476), 491–515.

Bailey, M. P. and Hallett, J. (2009). A comprehensive habit diagram for atmospheric ice crystals: Confirmation from the laboratory, AIRS ii, and other field studies. *Journal of the Atmospheric Sciences*, **66**(9), 2888–2899.

Balakrishnan, N. and Zrnic, D. (1990). Use of polarization to characterize precipitation and discriminate large hail. *Journal of the atmospheric sciences*, **47**(13), 1525–1540.

Batten, L. J. (1973). Radar observations of the atmosphere.

Beard, K. V. and Kubesh, R. J. (1991). Laboratory measurements of small raindrop distortion. Part 2: Oscillation frequencies and modes. *Journal of the atmospheric sciences*, **48**(20), 2245–2264.

Beard, K. V., Bringi, V., and Thurai, M. (2010). A new understanding of raindrop shape. *Atmospheric Research*, **97**(4), 396–415.

Bechini, R., Baldini, L., Chandrasekar, V., Cremonini, R., and Gorgucci, E. (2011). Observations of KDP in the ice region of precipitating clouds at X-band and C-band radar frequencies. In *Preprints, 35th Conf. on Radar Meteorology, Pittsburgh, PA, Amer. Meteor. Soc. A*, volume 7.

Brandes, E. A. and Ikeda, K. (2004). Freezing-level estimation with polarimetric radar. *Journal of Applied Meteorology*, **43**(11), 1541–1553.

Brandes, E. A., Zhang, G., and Vivekanandan, J. (2002). Experiments in rainfall estimation with a polarimetric radar in a subtropical environment. *Journal of Applied Meteorology*, **41**(6), 674–685.

Bringi, V. N. and Chandrasekar, V. (2001). *Polarimetric Doppler Weather Radar, Principles and Applications*. Cambridge University Press, Cambridge, UK.

Bringi, V. N., Seliga, T. A., and Cherry, S. M. (1983). Statistical properties of the dual-polarization differential reflectivity (z_{DR}) radar signal. *IEEE Trans. Geosci. Rem Sens.*, **GE-21**(2), 215 –220.

Brown, P. R. and Francis, P. N. (1995). Improved measurements of the ice water content in cirrus using a total-water probe. *Journal of Atmospheric and Oceanic Technology*, **12**(2), 410–414.

Cao, Q. and Zhang, G. (2009). Errors in estimating raindrop size distribution parameters employing disdrometer and simulated raindrop spectra. *Journal of Applied Meteorology and Climatology*, **48**(2), 406–425.

Cao, Q., Zhang, G., Brandes, E., Schuur, T., Ryzhkov, A., and Ikeda, K. (2008). Analysis of video disdrometer and polarimetric radar data to characterize rain microphysics in oklahoma. *Journal of Applied Meteorology and Climatology*, **47**(8), 2238–2255.

Caylor, I. J. (1989). *Radar Observations of Maritime Clouds using Dual Linear Polarisation*. Ph.D. thesis, University of Manchester, Manchester, UK.

Caylor, J. and Illingworth, A. J. (1989). Identification of the bright band and hydrometeors using co-polar dual polarization radar. In *Preprints, 24th Conf. on Radar Meteorology, Florida, USA, Amer. Meteor. Soc*, pages 352–357.

Cho, H., Iribarne, J., and Richards, W. (1981). On the orientation of ice crystals in a cumulonimbus cloud. *Journal of the Atmospheric Sciences*, **38**(5), 1111–1114.

Comstock, J. M., d'Entremont, R., DeSlover, D., Mace, G. G., *et al.* (2007). An intercomparison of microphysical retrieval algorithms for upper-tropospheric ice clouds. *Bulletin of the American Meteorological Society*, **88**(2), 191.

Crosier, J., Bower, K., Choularton, T., Westbrook, C. D., Connolly, P., Cui, Z., Crawford, I., Capes, G., Coe, H., Dorsey, J., *et al.* (2011). Observations of ice multiplication in a weakly convective cell embedded in supercooled mid-level stratus. *Atmospheric Chemistry and Physics*, **11**(1), 257–273.

de Boer, G., Eloranta, E. W., and Shupe, M. D. (2009). Arctic mixed-phase stratiform cloud properties from multiple years of surface-based measurements at two high-latitude locations. *Journal of the Atmospheric Sciences*, **66**(9), 2874–2887.

De Boer, G., Morrison, H., Shupe, M., and Hildner, R. (2011). Evidence of liquid dependent ice nucleation in high-latitude stratiform clouds from surface remote sensors. *Geophysical Research Letters*, **38**(1).

Doviak, R. J. and Zrnic (2006). *Doppler Radar and Weather Observations*. Dover Publications, Inc., Mineola, New York, USA.

Dufournet, Y. (2010). *Ice crystal properties retrieval using radar spectral polarimetric measurements within ice/mixed-phase clouds*. TU Delft, Delft University of Technology.

Field, P. R., Hogan, R. J., Brown, P. R. A., Illingworth, A. J., Choularton, T., Kaye, P., Hirst, E., and Greenaway, R. (2004). Simultaneous radar & aircraft observations of mixed-phase cloud at the 100 m scale. *Quart. J. Roy. Met. Soc.*, **130**(600), 1877–1904.

Fisher, R. A. (1915). Frequency distribution of the values of the correlation coefficient in samples from an indefinitely large population. *Biometrika*, **10**(4), 507–521.

Fleishauer, R. P., Larson, V. E., and Vonder Haar, T. H. (2002). Observed microphysical structure of midlevel, mixed-phase clouds. *Journal of the atmospheric sciences*, **59**(11), 1779–1804.

Fridlind, A., Ackerman, A., McFarquhar, G., Zhang, G., Poellot, M., DeMott, P., Prenni, A., and Heymsfield, A. (2007). Ice properties of single-layer stratocumulus during the mixed-phase arctic cloud experiment: 2. model results. *Journal of Geophysical Research: Atmospheres*, **112**(D24).

Fukuta, N. and Takahashi, T. (1999). The growth of atmospheric ice crystals: A summary of findings in vertical supercooled cloud tunnel studies. *Journal of the atmospheric sciences*, **56**(12), 1963–1979.

Gans, R. (1912). Über die form ultramikroskopischer goldteilchen. *Annalen der Physik*, **342**(5), 881–900.

Gayet, J.-F., Brown, P. R., and Albers, F. (1993). A comparison of in-cloud measurements obtained with six pms 2D-C probes. *Journal of Atmospheric and Oceanic Technology*, **10**(2), 180–194.

Giangrande, S. E., Krause, J. M., and Ryzhkov, A. V. (2008). Automatic designation of the melting layer with a polarimetric prototype of the WSR-88D radar. *Journal of Applied Meteorology and Climatology*, **47**(5), 1354–1364.

Goddard, J., Eastment, J. D., and Thurai, M. (1994). The chilbolton advanced meteorological radar: A tool for multidisciplinary atmospheric research. *Electronics & communication engineering journal*, **6**(2), 77–86.

Gregory, D. and Morris, D. (1996). The sensitivity of climate simulations to the specification of mixed phase clouds. *Clim. dyn.*, **12**(9), 641–651.

Hall, M. P., Goddard, J. W., and Cherry, S. M. (1984). Identification of hydrometeors and other targets by dual-polarization radar. *Radio Science(ISSN 0048-6604)*, **19**, 132–140.

Hallett, J. and Mossop, S. C. (1974). Production of secondary ice particles during the riming process. *Nature*, **249**, 26–28.

Harimaya, T. (1975). The riming properties of snow crystals. *J. Meteor. Soc. Japan*, **53**, 384–392.

Harrington, J. Y., Reisin, T., Cotton, W. R., and Kreidenweis, S. M. (1999). Cloud resolving simulations of arctic stratus: Part ii: Transition-season clouds. *Atmospheric Research*, **51**(1), 45–75.

Heymsfield, A. and Knollenberg, R. (1972). Properties of cirrus generating cells. *Journal of the Atmospheric Sciences*, **29**(7), 1358–1366.

Heymsfield, A. J. and Iaquinta, J. (2000). Cirrus crystal terminal velocities. *Journal of the Atmospheric Sciences*, **57**(7), 916–938.

Hobbs, P. V. and Rangno, A. L. (1998). Microstructures of low and middle-level clouds over the beaufort sea. *Quarterly Journal of the Royal Meteorological Society*, **124**(550), 2035–2071.

Hobbs, P. V., Chang, S., and Locatelli, J. D. (1974). The dimensions and aggregation of ice crystals in natural clouds. *Journal of Geophysical Research*, **79**(15), 2199–2206.

Hogan, R., Illingworth, A., O'connor, E., and Baptista, J. (2003). Characteristics of mixed-phase clouds. ii: A climatology from ground-based lidar. *Quart. J. Roy. Meteor. Soc.*, **129**(592), 2117–2134.

Hogan, R., Francis, P., Flentje, H., Illingworth, A., Quante, M., and Pelon, J. (2003a). Characteristics of mixed-phase clouds. i: Lidar, radar & aircraft observations from clare'98. *Quart. J. Roy. Meteor. Soc.*, **129**(592), 2089–2116.

Hogan, R. J., Field, P. R., Illingworth, A. J., Cotton, R. J., and Choularton, T. W. (2002). Properties of embedded convection in warm-frontal mixed-phase cloud from aircraft and polarimetric radar. *Quart. J. Roy. Met. Soc.*, **128**(580), 451–476.

Hogan, R. J., Behera, M. D., O'Connor, E. J., and Illingworth, A. J. (2004). Estimate of the global distribution of stratiform supercooled liquid water clouds using the LITE lidar. *Geophysical research letters*, **31**(5).

Illingworth, A., Hogan, R., OConnor, E., Bouniol, D., Delanoë, J., Pelon, J., Protat, A., Brooks, M., Gaussiat, N., Wilson, D., *et al.* (2007). Cloudnet-continuous evaluation of cloud profiles in seven operational models using ground-based observations, B. Am. Meteorol. Soc., 88, 883–898, doi: 10.1175. Technical report, BAMS-88-6-883.

Illingworth, A. J. and Caylor, I. J. (1991). Co-polar correlation measurements of precipitation. In *Preprints, 25th Int. Conf. on Radar Meteorology, Paris, France, Amer. Meteor. Soc*, pages 650–653.

Jameson, A. and Kostinski, A. (1998). Fluctuation properties of precipitation. Part ii: Reconsideration of the meaning and measurement of raindrop size distributions. *Journal of the atmospheric sciences*, **55**(2), 283–294.

Jiang, H., Cotton, W. R., Pinto, J. O., Curry, J. A., and Weissbluth, M. J. (2000). Cloud resolving simulations of mixed-phase arctic stratus observed during base: Sensitivity to concentration of ice crystals and large-scale heat and moisture advection. *Journal of the atmospheric sciences*, **57**(13), 2105–2117.

Johnson, R. W., Kliche, D. V., and Smith, P. L. (2014). Maximum likelihood estimation of gamma parameters for coarsely binned and truncated raindrop size data. *Quarterly Journal of the Royal Meteorological Society*, **140**(681), 1245–1256.

Kajikawa, M. (1972). Measurement of falling velocity of individual snow crystals. *J. Meteor. Soc. Japan*, **50**, 577–583.

Kajikawa, M. (1982). Observation of the falling motion of early snow flakes. 1. relationship between the free-fall pattern and the number and shape of component snow crystals. *Journal of the Meteorological Society of Japan*, **60**(2), 797–803.

Kajikawa, M. (1992). Observations of the falling motion of plate-like snow crystals. i: The free-fall patterns and velocity variations of unrimed crystals. *Journal of the Meteorological Society of Japan*, **70**(1), 1–9.

Keat, W., Westbrook, C., and Illingworth, A. (2016). High-precision measurements of the co-polar correlation coefficient: Non-gaussian errors and retrieval of the dispersion parameter μ in rainfall. *Journal of Applied Meteorology and Climatology*, (2016).

Kennedy, P. C. and Rutledge, S. A. (2011). S-band dual-polarization radar observations of winter storms. *Journal of Applied Meteorology and Climatology*, **50**(4), 844–858.

Klein, S. A., McCoy, R. B., Morrison, H., Ackerman, A. S., Avramov, A., Boer, G. d., Chen, M., Cole, J. N., Del Genio, A. D., Falk, M., *et al.* (2009). Intercomparison of model simulations of mixed-phase clouds observed during the arm mixed-phase arctic cloud experiment. i: Single-layer cloud. *Quarterly Journal of the Royal Meteorological Society*, **135**(641), 979–1002.

Korolev, A. and Field, P. R. (2008). The effect of dynamics on mixed-phase clouds: Theoretical considerations. *Journal of the Atmospheric Sciences*, **65**(1), 66–86.

Korolev, A., Isaac, G., and Hallett, J. (2000). Ice particle habits in stratiform clouds. *Quarterly Journal of the Royal Meteorological Society*, **126**(569), 2873–2902.

Korolev, A., Isaac, G., Strapp, J., Cober, S., and Barker, H. (2007). In situ measurements of liquid water content profiles in midlatitude stratiform clouds. *Quarterly Journal of the Royal Meteorological Society*, **133**(628), 1693–1699.

Korolev, A., Emery, E., Strapp, J., Cober, S., Isaac, G., Wasey, M., and Marcotte, D. (2011). Small ice particles in tropospheric clouds: Fact or artifact? airborne icing instrumentation evaluation experiment. *Bulletin of the American Meteorological Society*, **92**(8), 967–973.

Korolev, A. V., Isaac, George, A., Cober, S. G., Strapp, J. W., and Hallett, J. (2003). Microphysical characterization of mixed-phase clouds. *Quart. J. Roy. Met. Soc.*, **129**(587), 39–65.

Lamb, D. and Verlinde, J. (2011). *Physics and chemistry of clouds*. Cambridge University Press.

Liu, L., Bringi, V. N., Chandrasekar, V., Mueller, E. A., and Mudukutore, A. (1994). Analysis of the co-polar correlation coefficient between horizontal and vertical polarizations. *Journal of Atmospheric and Oceanic Technology*, **11**(4), 950–963.

Locatelli, J. D. and Hobbs, P. V. (1974). Fall speeds and masses of solid precipitation particles. *Journal of Geophysical Research*, **79**(15), 2185–2197.

Magono, C., Chung, W., *et al.* (1966). Meteorological classification of natural snow crystals. *Journal of the Faculty of Science, Hokkaido University. Series 7, Geophysics*, **2**(4), 321–335.

Marsham, J., Dobbie, S., and Hogan, R. (2006). Evaluation of a large-eddy model simulation of a mixed-phase altocumulus cloud using microwave radiometer, lidar and doppler radar data. *Quarterly Journal of the Royal Meteorological Society*, **132**(618), 1693–1715.

McFarquhar, G. M. (2004). The effect of raindrop clustering on collision-induced breakup of raindrops. *Quarterly Journal of the Royal Meteorological Society*, **130**(601), 2169–2190.

Melnikov, V. and Straka, J. M. (2013). Axis ratios and flutter angles of cloud ice particles: Retrievals from radar data. *Journal of Atmospheric and Oceanic Technology*, **30**(8), 1691–1703.

Meyers, M. P., DeMott, P. J., and Cotton, W. R. (1992). New primary ice-nucleation parameterizations in an explicit cloud model. *Journal of Applied Meteorology*, **31**(7), 708–721.

Mitchell, D. L. (1996). Use of mass-and area-dimensional power laws for determining precipitation particle terminal velocities. *Journal of the atmospheric sciences*, **53**(12), 1710–1723.

Mitchell, J. F., Senior, C., and WJ, I. (1989). CO_2 and climate: a missing feedback? *Nature*, **341**(6238), 132–134.

Moisseev, D., Saltikoff, E., and Leskinen, M. (2009). Dual-polarization weather radar observations of snow growth processes. In *Preprints, 34th Conf. on Radar Meteorology, Williamsburg, VA, Amer. Meteor. Soc. B*, volume 13.

Moisseev, D. N., Lautaportti, S., Tyynela, J., and Lim, S. (2015). Dual-polarization radar signatures in snowstorms: Role of snowflake aggregation. *Journal of Geophysical Research: Atmospheres*, **120**(24), 12644–12655.

Morrison, A. E., Siems, S. T., and Manton, M. J. (2011). A three-year climatology of cloud-top phase over the southern ocean and north pacific. *Journal of Climate*, **24**(9), 2405–2418.

Morrison, H., Shupe, M., and Curry, J. (2003). Modeling clouds observed at sheba using a bulk microphysics parameterization implemented into a single-column model. *Journal of Geophysical Research: Atmospheres*, **108**(D8).

Morrison, H., McCoy, R. B., Klein, S. A., Xie, S., Luo, Y., Avramov, A., Chen, M., Cole, J. N., Falk, M., Foster, M. J., *et al.* (2009). Intercomparison of model simulations of mixed-phase clouds observed during the arm mixed-phase arctic cloud experiment. ii: Multilayer cloud. *Quarterly Journal of the Royal Meteorological Society*, **135**(641), 1003–1019.

Morrison, H., de Boer, G., Feingold, G., Harrington, J., Shupe, M. D., and Sulia, K. (2012). Resilience of persistent arctic mixed-phase clouds. *Nature Geoscience*, **5**(1), 11–17.

Mülmenstädt, J., Sourdeval, O., Delanoë, J., and Quaas, J. (2015). Frequency of occurrence of rain from liquid-, mixed-, and ice-phase clouds derived from a-train satellite retrievals. *Geophysical Research Letters*, **42**(15), 6502–6509.

Ono, A. (1969). The shape and riming properties of ice crystals in natural clouds. *Journal of the Atmospheric Sciences*, **26**(1), 138–147.

Papoulis, A. (1965). Probability, random variables, and stochastic processes.

Park, H. S., Ryzhkov, A. V., Zrnic, D., and Kim, K.-E. (2009). The hydrometeor classification algorithm for the polarimetric WSR-88D: Description and application to an MCS. *Weather and Forecasting*, **24**(3), 730–748.

Platt, C. (1978). Lidar backscatter from horizontal ice crystal plates. *Journal of Applied Meteorology*, **17**(4), 482–488.

Politovich, M. K. (1989). Aircraft icing caused by large supercooled droplets. *Journal of Applied Meteorology*, **28**(9), 856–868.

Pruppacher, H. R. and Klett, J. D. (1997). *Microphysics of clouds and precipitation*. Kluwer Acadenic Publishers, Boston, USA.

Rambukkange, M. P., Verlinde, J., Eloranta, E. W., Flynn, C. J., and Clothiaux, E. E. (2011). Using doppler spectra to separate hydrometeor populations and analyze ice precipitation in multilayered mixed-phase clouds. *Geoscience and Remote Sensing Letters, IEEE*, **8**(1), 108–112.

Rauber, R. M. and Tokay, A. (1991). An explanation for the existence of supercooled water at the top of cold clouds. *Journal of the atmospheric sciences*, **48**(8), 1005–1023.

Rogers, R. (1989). Raindrop collision rates. *Journal of the Atmospheric Sciences*, **46**(15), 2469–2472.

Ryzhkov, A. V. and Zrnic, D. S. (1998). Polarimetric rainfall estimation in the presence of anomalous propagation. *Journal of Atmospheric and Oceanic Technology*, **15**(6), 1320–1330.

Sachidananda, M. and Zrnic, D. (1989). Efficient processing of alternately polarized radar signals. *Journal of Atmospheric and Oceanic Technology*, **6**(1), 173–181.

Sassen, K. (1980). Remote sensing of planar ice crystal fall attitudes. *J. Meteor. Soc. Japan*, **58**(5), 422–429.

Schafer, R., Avery, S., May, P., Rajopadhyaya, D., and Williams, C. (2002). Estimation of rainfall drop size distributions from dual-frequency wind profiler spectra using deconvolution and a nonlinear least squares fitting technique. *Journal of Atmospheric and Oceanic Technology*, **19**(6), 864–874.

Schönhuber, M., Lammer, G., and Randeu, W. L. (2008). The 2D-video-distrometer. In *Precipitation: Advances in measurement, estimation and prediction*, pages 3–31. Springer.

Seliga, T. and Bringi, V. (1976). Potential use of radar differential reflectivity measurements at orthogonal polarizations for measuring precipitation. *Journal of Applied Meteorology*, **15**(1), 69–76.

Senior, C. and Mitchell, J. (1993). Carbon dioxide and climate. the impact of cloud parameterization. *Journal of Climate*, **6**(3), 393–418.

Senior, T. (1976). Low-frequency scattering by a dielectric body. *Radio Science*, **11**(5), 477–482.

Shupe, M. D. (2011). Clouds at arctic atmospheric observatories. Part ii: Thermodynamic phase characteristics. *Journal of Applied Meteorology and Climatology*, **50**(3), 645–661.

Shupe, M. D., Matrosov, S. Y., and Uttal, T. (2006). Arctic mixed-phase cloud properties derived from surface-based sensors at sheba. *Journal of the atmospheric sciences*, **63**(2), 697–711.

Shupe, M. D., Daniel, J. S., De Boer, G., Eloranta, E. W., Kollias, P., Long, C. N., Luke, E. P., Turner, D. D., and Verlinde, J. (2008a). A focus on mixed-phase clouds: The status of ground-based observational methods. *Bulletin of the American Meteorological Society*, **89**(10), 1549.

Shupe, M. D., Kollias, P., Persson, P. O. G., and McFarquhar, G. M. (2008b). Vertical motions in arctic mixed-phase stratiform clouds. *Journal of the Atmospheric Sciences*, **65**(4), 1304–1322.

Solomon, S., Qin, D., Manning, M., Chen, Z., Marquis, M., Averyt, K., Tignor, M., and Miller, H. (2007). Contribution of working group i to the fourth assessment report of the intergovernmental panel on climate change, 2007.

Stoelinga, M. T., Locatelli, J. D., and Woods, C. P. (2007). The occurrence of irregular ice particles in stratiform clouds. *Journal of the atmospheric sciences*, **64**(7), 2740–2750.

Sun, Z. and Shine, K. (1994). Studies of the radiative properties of ice and mixed-phase clouds. *Quart. J. Roy. Meteor. Soc.*, **120**(515), 111–137.

Szakáll, M., Diehl, K., Mitra, S. K., and Borrmann, S. (2008). A wind tunnel study on the oscillation of freely falling raindrops. In *Proc. Fifth European Conf. on Radar in Meteorology and Hydrology (ERAD 2008)*.

Szakáll, M., Mitra, S. K., Diehl, K., and Borrmann, S. (2010). Shapes and oscillations of falling raindropsa review. *Atmospheric Research*, **97**(4), 416–425.

Szakáll, M., Kessler, S., Diehl, K., Mitra, S. K., and Borrmann, S. (2014). A wind tunnel study of the effects of collision processes on the shape and oscillation for moderate-size raindrops. *Atmospheric Research*, **142**, 67–78.

Tabary, P., Le Henaff, A., Vulpiani, G., Parent-du Châtelet, J., and Gourley, J. (2006). Melting layer characterization and identification with a C-band dual-polarization radar: A long-term analysis. In *Proc. Fourth European Radar Conf*, pages 17–20.

Takahashi, T. (2014). Influence of liquid water content and temperature on the form and growth of branched planar snow crystals in a cloud. *Journal of the Atmospheric Sciences*, **71**(11), 4127–4142.

Takahashi, T., Endoh, T., Wakahama, G., and Fukuta, N. (1991). Vapor diffusional growth of free-falling snow crystals between -3 and- 23°C. *Journal of the Meteorological Society of Japan*, **69**(1), 15–30.

Tang, L., Zhang, J., Langston, C., Krause, J., Howard, K., and Lakshmanan, V. (2014). A physically based precipitation–nonprecipitation radar echo classifier using polarimetric and environmental data in a real-time national system. *Weather and Forecasting*, **29**(5), 1106–1119.

Thomas, L., Cartwright, J., and Wareing, D. (1990). Lidar observations of the horizontal orientation of ice crystals in cirrus clouds. *Tellus B*, **42**(2), 211–216.

Thurai, M. and Bringi, V. (2005). Drop axis ratios from a 2d video disdrometer. *Journal of Atmospheric & Oceanic Technology*, **22**(7).

Thurai, M., Hudak, D., and Bringi, V. (2008). On the possible use of co-polar correlation coefficient for improving the drop size distribution estimates at c band. *Journal of Atmospheric and Oceanic Technology*, **25**(10), 1873–1880.

Thurai, M., S. M. B. V. N. and Mitra, S. K. (2013). Collision-induced drop oscillations from wind-tunnel experiments. In *Proc. 36th Conference on Radar Meteorology*.

Tokay, A., Kruger, A., and Krajewski, W. F. (2001). Comparison of drop size distribution measurements by impact and optical disdrometers. *Journal of Applied Meteorology*, **40**(11), 2083–2097.

Torlaschi, E. and Gingras, Y. (2003). Standard deviation of the co-polar correlation coefficient for simultaneous transmission and reception of vertical and horizontal polarized weather radar signals. *Journal of Atmospheric and Oceanic Technology*, **20**(5), 760–766.

Ulbrich, C. W. (1983). Natural variations in the analytical form of the raindrop size distribution. *Journal of Climate and Applied Meteorology*, **22**(10), 1764–1775.

Unal, C. (2015). High resolution raindrop size distribution retrieval based on the doppler spectrum in the case of slant profiling radar. *Journal of Atmospheric and Oceanic Technology*, (2015).

Wang, P. K. and Ji, W. (2000). Collision efficiencies of ice crystals at low-intermediate reynolds numbers colliding with supercooled cloud droplets: A numerical study. *Journal of the atmospheric sciences*, **57**(8), 1001–1009.

Westbrook, C. (2008). The fall speeds of sub-100 μm ice crystals. *Quarterly Journal of the Royal Meteorological Society*, **134**(634), 1243–1251.

Westbrook, C. (2013). Notes and correspondence: Rayleigh scattering by hexagonal ice crystals and the interpretation of dual-polarisation radar measurements.

Westbrook, C. and Illingworth, A. (2011a). The formation of ice in a long-lived supercooled layer cloud.

Westbrook, C., Illingworth, A., O'Connor, E., and Hogan, R. (2010). Doppler lidar measurements of oriented planar ice crystals falling from supercooled and glaciated layer clouds. *Quarterly Journal of the Royal Meteorological Society*, **136**(646), 260–276.

Westbrook, C. D. and Heymsfield, A. J. (2011). Ice crystals growing from vapor in supercooled clouds between -2.5 and -22°C: Testing current parameterization methods using laboratory data. *Journal of the Atmospheric Sciences*, **68**(10), 2416–2429.

Westbrook, C. D. and Illingworth, A. (2011b). Evidence that ice forms primarily in supercooled liquid clouds at temperatures >-27°C. *Geophys. Res. Lett.*, **38**(14), L14808.

Williams, C. R. (2002). Simultaneous ambient air motion and raindrop size distributions retrieved from UHF vertical incident profiler observations. *Radio Science*, **37**(2).

Williams, C. R., Bringi, V., Carey, L. D., Chandrasekar, V., Gatlin, P. N., Haddad, Z. S., Meneghini, R., Joseph Munchak, S., Nesbitt, S. W., Petersen, W. A., *et al.* (2014). Describing the shape of raindrop size distributions using uncorrelated raindrop mass spectrum parameters. *Journal of Applied Meteorology and Climatology*, **53**(5), 1282–1296.

Willmarth, W. W., Hawk, N. E., and Harvey, R. L. (1964). Steady and unsteady motions and wakes of freely falling disks.

Wilson, D. R., Illingworth, A. J., and Blackman, T. M. (1997). Differential doppler velocity: A radar parameter for characterizing hydrometeor size distributions. *Journal of Applied Meteorology*, **36**(6), 649–663.

Wolde, M. and Vali, G. (2001). Polarimetric signatures from ice crystals observed at 95 ghz in winter clouds. Part ii: Frequencies of occurrence. *Journal of the atmospheric sciences*, **58**(8), 842–849.

Yau, M. K. and Rogers, R. (1996). *A short course in cloud physics*. Elsevier.

Young, K. C. (1993). *Microphysical processes in clouds*. Oxford University Press, Oxford, UK.

Zhang, D., Wang, Z., and Liu, D. (2010). A global view of midlevel liquid-layer topped stratiform cloud distribution and phase partition from CALIPSO and CloudSat measurements. *Journal of Geophysical Research: Atmospheres*, **115**(D4).